

Observable Signatures of EMRI Black Hole Binaries Embedded in Thin Accretion Disks

Bence Kocsis,¹ Nicolás Yunes,^{2,1} and Abraham Loeb¹

¹*Harvard-Smithsonian Center for Astrophysics, 60 Garden St., Cambridge, MA 02138, USA.*

²*Dept. of Physics and MIT Kavli Institute, Massachusetts Institute of Technology,
77 Massachusetts Avenue, Cambridge, MA 02139, USA.*

(Dated: January 19, 2013)

We examine the electromagnetic (EM) and gravitational wave (GW) signatures of stellar-mass compact objects (COs) spiraling into a supermassive black hole (extreme mass-ratio inspirals or EMRIs), embedded in a thin, radiation-pressure dominated, accretion disk. At large separations, the tidal effect of the secondary CO clears a gap. We show that the gap refills during the late GW-driven phase of the inspiral, leading to a sudden EM brightening of the source. The accretion disk leaves an imprint on the GW through its angular momentum exchange with the binary, the mass increase of the binary members due to accretion, and its gravity. We compute the disk-modified GWs both in an analytical Newtonian approximation and in a numerical effective-one-body approach. We find that disk-induced migration provides the dominant perturbation to the inspiral, with weaker effects from the mass accretion onto the CO and hydrodynamic drag. Depending on whether a gap is present, the perturbation of the GW phase is between 10 and 1000 radians per year, detectable with the future Laser Interferometer Space Antenna (LISA) at high significance. The Fourier transform of the disk-modified GW in the stationary phase approximation is sensitive to disk parameters with a frequency trend different from post-Newtonian vacuum corrections. Our results suggest that observations of EMRIs may place new sensitive constraints on the physics of accretion disks.

PACS numbers: 04.30.Tv, 98.62.Mw, 04.30.-w, 95.30.Sf

CONTENTS

I. Introduction	2	D. Implications of BHL Accretion	17
A. Relevance of Accretion Disks to EMRIs	2	1. EMRI formation scenarios	18
B. Previous Explorations	3	2. GW Observations	18
C. Executive Summary of Results	5	V. Hydrodynamic Drag	19
D. Organization and Conventions	7	A. Azimuthal wind	19
II. Review of EMRI GWs	7	B. Radial wind	20
A. Basics of EMRI Dynamics	7	C. Dynamical friction	20
B. Measures of LISA Sensitivity to GWs	8	D. GW Implications	20
1. Simple Mass and Time-Scale Measures	8	VI. Axisymmetric Gravitational Effects	21
2. Dephasing Measure	9	A. Accretion Disk Potential	21
3. Degeneracies and Template Placement	9	B. Change in the orbital frequency	22
III. Review of Accretion Disk Models	9	C. Change in the inspiral rate	22
A. Basics of Accretion-Disk Models	9	D. Apsidal precession	22
B. Gap opening	12	E. GW Implications	22
1. Gap decoupling	13	VII. Migration	22
2. Density enhancement outside the gap	14	A. General Properties	23
C. Twists, warps, and disk alignment	14	B. Type-I migration	23
IV. Mass Increase via Gas Accretion	14	C. Type-II migration	24
A. Primary Mass Increase	14	D. Quenching of migration	24
B. Secondary Mass Increase	15	E. GW Implications	25
C. Quenching of BHL Accretion	15	VIII. Comparison of Accretion Disk Effects	25
1. Quenching by wind and tidal effects	15	IX. Relativistic Waveforms and Detection	27
2. Quenching by thin disk geometry	16	A. Systems Investigated	27
3. Quenching by limited gas supply	16	B. Basics of the EOB Framework	28
4. Quenching by radiation pressure	16	C. Disk Modifications to EOB GWs	29
5. Quenching by gap formation	17	1. Effective Hamiltonian	29
6. Summary of quenching processes	17	2. Radiation-Reaction Force	30

X. Data Analysis Considerations	30
A. Dephasing Analysis	30
B. Overlap Analysis	31
C. Degeneracies	31
XI. Discussion	34
Acknowledgments	35
A. Phase Correction due to CO Accretion	35
1. Unsaturated BHL accretion	35
2. Gas supply limited BHL accretion	36
B. Phase Correction due to Wind and Migration	36
1. Wind – unsaturated BHL accretion	37
2. Wind – quenched BHL accretion	37
3. Type-I migration	37
4. Type-II migration	38
C. Phase Correction due to the Disk Gravity	38
1. Disk Potential	38
2. Axisymmetric disk gravity without a gap	39
References	39

I. INTRODUCTION

The full exploitation of gravitational wave (GW) signals will hinge on controlling all systematics associated with their astrophysical sources. One can classify such systematics into three major groups: instrumental, theoretical, and astrophysical. Instrumental systematics are associated with possible issues related to the detector. For example, the future Laser Interferometer Space Antenna (LISA) [1–4] might suffer from instrumental glitches [5]. Such glitches, and other potential instrumental issues, might lead to a foreground of noise artifacts that might have to be either removed, or dealt with via data analysis techniques.

Theoretical systematics are due to incomplete modeling of waveform templates [6]. The extraction of GWs from noisy data requires the construction of these optimized filters, which represent our best guess model for the GWs generated by the source. Since approximation schemes (either analytical or numerical) are employed to solve Einstein’s equations of General Relativity (GR) for the source, the templates used for data analysis are not exact solutions and can introduce errors in parameter estimation [6].

Astrophysical systematics arise from modifications to the waveforms caused by the environment. For example, when modeling GWs from black hole (BH) or neutron star (NS) binary coalescences, one usually assumes the binary is isolated from external perturbers and ambient electromagnetic (EM) or matter fields. However, the unresolved GW foreground of Galactic and extragalactic white dwarfs (WDs), and possibly extreme

mass ratio inspirals, introduces additional astrophysical noise for LISA sources (see Ref. [7] and references therein). Furthermore, an additional nearby supermassive BH (SMBH) in the vicinity of a merging binary can lead to detectable Doppler-shifts in the GW signal [8].

Astrophysical systematics are expected to be negligible for the final stages of the inspiral and merger of two SMBHs, because the SMBH’s inertia greatly exceeds that of the environment. However, this is not the case for extreme mass-ratio inspirals (EMRIs), where a small compact object (CO) spirals into a SMBH [9]. In this case, the GW inspiral rate and signal amplitude are decreased by a factor of the mass-ratio, making these systems more sensitive to astrophysical perturbations as well as theoretical uncertainties. EMRIs produce millions of GW cycles in the LISA frequency band with signal-to-noise ratios (SNRs) around 20 with a GW phasing accuracy better than 1 radian and logarithmic mass measurement accuracy of 10^{-3} – 10^{-5} for a typical source at 1 Gpc observed for a year [10].

In this paper we consider the most important effects that a radiatively-efficient, thin accretion disk might have on an EMRI that is embedded in it:

- (i) SMBH mass increase due to accretion;
- (ii) CO mass increase due to accretion;
- (iii) modification of the gravitational potential due to the disk’s self-gravity (e.g. changing the angular velocity of the orbit as a function of radius, and inducing additional apsidal and nodal precession);
- (iv) modification in the energy and angular momentum dissipation rate (e.g. hydrodynamic drag from winds, torques from spiral arms, and resonant interactions analogous to planetary migrations).

We examine the conditions necessary for the tidal gravity of the CO to open a gap in radiation-pressure supported accretion disks, and its implications on the EM and GW signals. In particular, we study whether LISA will have sufficient sensitivity to resolve the presence and structure of the accretion disk.

A. Relevance of Accretion Disks to EMRIs

EMRIs are expected to form in dense galactic nuclei of stars, WDs, NSs, and BHs in orbit around a central SMBH. These dense nuclei are sometimes called *galactic cusps* (see e.g. [9]), because of their sharply peaked density profile at zero radius. Some of these galactic nuclei are coincidentally *active*, meaning that gas is currently accreting onto the central SMBH and produces bright EM radiation. Accretion disk effects on EMRIs are most prominent in active galactic nuclei (AGN) where gas is actively feeding the central SMBH.

Plausible arguments have been put forth both against and in favor of the common existence of EMRIs in AGN

disks. EMRIs can only be detected at relatively low redshift ($z \lesssim 0.5$) [11], but only a small fraction of galaxies within $z < 2$ are active and host a massive gaseous disk. AGN activity may be triggered by the inflow of gas during major galaxy mergers [12]. However, the SMBHs in the centers of merging galaxies form a binary, which may deplete the central cusp of stars [13], thereby reducing the probability of EMRI events. On the other hand, AGN activity may be fueled by the tidal disruption of stars in dense central cusps, which have large EMRI rates [14]. Stars may be captured or may form in accretion disks by fragmentation and/or coagulation of density enhancements [15–17]. The remnants of these stars would be pushed inwards by the disk and could provide a reservoir of EMRI events in AGNs.

Astrophysical evidence already exists for tightly bound BH binaries with accretion disks. OJ287 is believed to be an SMBH-SMBH binary, with masses of $10^8 M_\odot$ and $\sim 10^{10} M_\odot$, respectively, orbiting in an inclined accretion disk of mass $\sim 10^2 M_\odot$ [18]. For this system, optical flashes are observed periodically and interpreted as crossings of the accretion disk by the smaller object. For EMRIs with stellar mass COs, similar EM flares will be much harder to detect.

Estimates on the expected EMRI rates are very uncertain, around a few tens to a few hundreds per year [11]. LISA is expected to be sensitive to EMRIs up to redshifts close to unity [7], although most events should be at redshift much smaller than unity. A few percent among these might be in AGN environments, where accretion disk effects are non-negligible. These sources, if observed, may become the most interesting EMRI sources for studying astrophysics with LISA.

We examine whether an EMRI, if present in the accretion disk, is capable of regulating the accretion of the SMBH. If the secondary is sufficiently massive, its tidal gravity would expel gas from the inner regions, greatly reducing the amount of gas that would fall into the SMBH, and thus decreasing the disk's EM luminosity. However, as the inspiral proceeds, and the relative importance of tidal field changes compared to the local radiation pressure in the disk, the disk might refill, reigniting bright AGN activity.

The presence of an accretion disk around EMRIs also leads to interesting possibilities for future GW detections. A detection of the imprint of an accretion disk on the GW signal could inform us about accretion disk physics. But by the same token, the presence of the disk complicates the modeling of the GW signal, as the rather uncertain accretion disk physics introduces additional theoretical errors and potentially makes tests of GR with EMRIs more difficult.

If GWs could inform us about accretion disk physics, they could then provide candidates for EM counterpart searches. Indeed, accretion disks are very sensitive to the accretion rate parameter. A LISA measurement of the accretion rate would imply a plausible range of AGN luminosity. Then, by looking at the LISA source location

box (approximately 1° angular, 10^{-3} distance measurement accuracy [10]), EM instruments could search for AGNs with the predicted luminosity and redshift [19]. Since bright AGNs are relatively sparsely distributed in the universe relative to the LISA error volume, a search could cut down the number of galaxy candidates to just one [20]. Alternatively, the EM counterpart could be identified in case it is strongly modulated in time by the EMRI.

The identification of an EM counterpart would allow the use of EMRIs as standard sirens: measuring the distance using the EM redshift and the GW luminosity, which would allow to independently test cosmological models [21–23]. Peculiar velocities and weak lensing are expected to be the main limitation for studying cosmology with LISA, implying that a large number of low redshift sources such as the EMRIs considered here, are necessary for tightening existing cosmological constraints [20].

B. Previous Explorations

Accretion disks are common astrophysical systems that have been studied in depth, but only recently has there been some effort to discuss their effect on GW sources. To our knowledge, the first study of accretion disk effects on GWs was by Giampieri [24]. He considered an equal-mass binary, where each component is gaining mass due to accretion, in turn leading to a modified radial inspiral rate. He then argued that a measurement of the so-called GW braking index, $k_{\text{GW}} = f_{\text{GW}} \dot{f}_{\text{GW}} / \dot{f}_{\text{GW}}^2$, where f_{GW} is the GW frequency, could lead to information on the rate of accretion. However, if limited by the Eddington rate¹, the accretion timescale is $\sim 10^8$ times larger than the observation time and the effects on GWs is insignificant (see Sec. IV A below).

Almost simultaneously with Giampieri, Chakrabarti [25, 26] and then Giampieri, Gerardi and Molteni [27] considered an EMRI embedded in an accretion disk, where the CO accretes in the Bondi-Hoyle-Lyttleton (BHL) approximation² [28–32]. Assuming the gas velocity is different from the CO's velocity due to pressure gradient effects, they found that the CO experiences a head-wind (accelerating the coalescence) or a tail-wind (delaying the coalescence), depending on whether the disk is rotating at sub-Keplerian or super-Keplerian velocities. For very high accretion rates, the flow is trans-sonic and super-Keplerian, and

¹ The Eddington limit is defined as the mass accretion rate at which the inward gravitational force is balanced by the radiation-pressure force produced by the in-falling matter in spherical symmetry; see Sec. IV A for details.

² BHL accretion results when the accreting object is completely embedded in a gaseous medium and accretes isotropically; see Sec. IV B for further details.

the tailwind could supersede the angular momentum loss via GW emission, leading to a stalled orbit or even an out-spiral.

Later on, Narayan [33] examined the effect of radiatively-inefficient accretion flows on EMRIs. In quiescent nuclei, the accretion rate is often much lower than the limiting Eddington value and the accretion flow is dominated by advection of the thermal energy. Accretion disks of this type are commonly referred to as being “radiatively inefficient,” since the thermal energy of the gas is advected inwards rather than radiated away as in thin accretion disks. Narayan estimated the importance of hydrodynamic drag by computing the ratio of the timescale on which the EMRI loses angular momentum due to hydrodynamic torques and GW emission. For all reasonable sets of ADAF disk parameters, he found that the GW phase is changed by order 10^{-2} radians, well below the measurement accuracy of LISA.

Shortly after, Šubr and Karas [34, 35] investigated the evolution of the eccentricity and inclination of a CO when crossing a thin radiatively-efficient Shakura-Sunyaev α -disk³ [36]. Assuming that the disk is not perturbed by the CO significantly, they found that the orbit circularizes and aligns with the plane of the disk in its outskirts. In a follow-up work [35], they extended their study to the inner parts of the Shakura-Sunyaev disks, where the radiation pressure significantly modifies the density profile, and examined hydrodynamic drag during disk crossing, and angular momentum exchange with spiral density waves analogous to Type I and II planetary migration. They have provided formulas for the relative timescale of the effects, and concluded that GW emission drives the evolution interior to $\sim 100 \text{ GM}/c^2$.

Another important study in this field was presented by Levin [17]. Motivated by simulations of Gammie [37], Levin constructed models of thin self-gravitating, radiatively-efficient disks, including optically thick (i.e. photons scatter several times before escaping the disk) and thin regimes. He re-derived order-of-magnitude estimates of the non-relativistic hydrodynamic drag and planetary migration timescales, similar to that of Karas and Šubr [35], and also included the effect of azimuthal winds. Based on these estimates, Levin argued that, although GW emission drives the evolution inside $\sim 100 \text{ GM}/c^2$, such disk effects may be important for LISA EMRIs.

More recently, Barausse and Rezzolla [38] examined the effects of relativistic hydrodynamic drag on EMRIs embedded in a thick torus. They found that the hydrodynamic drag drives the EMRI toward alignment overcoming the GW radiation reaction, which by itself would drive the orbital plane toward anti-alignment with the MBHs spin [39]. However, stationary thick massive tori with constant specific angular momentum are unstable

to global non-axisymmetric modes that grow on a dynamical timescale [40–42], making their conclusions on EMRIs rather uncertain.

The EM emission of accretion disks around sub-parsec scale BH binaries have been considered by many authors. However, previous explorations focused on comparable mass binaries. In this case, the gravitational effects would clear a gap around the binary, significantly reducing accretion. As long as the binary separation is large enough that the gas can follow the GW inspiral rate of the binary, tidal stresses would act to increase the EM luminosity of the disk [43]. Eventually, however, the gas is left behind at radii exceeding $100 \text{ GM}/c^2$ for equal mass systems and the gap freezes relative to the rapid GW-induced inspiral. Consequently, bright EM emission would be expected only several years after the merger, when the gas has had time to diffuse inwards and accrete onto the remnant SMBH [44]. However, periodic inflow across the gap may generate EM variability prior to merger [45–48] or the secondary can shepherd any gas remaining interior to its orbit into the SMBH after gap freez-out [49]. The conditions for gap opening have not been examined in radiation-pressure dominated accretion disks, which is most relevant at separations smaller than $\sim 1000 \text{ GM}/c^2$. Here, we investigate whether this can lead to gap refilling prior to merger, which could have important consequences for EM signatures of EMRIs.

None of the previous studies examined in detail whether LISA has the sufficient accuracy to resolve the imprint of accretion disk effects on EMRI GWs and whether any of the accretion disk parameters may be recovered; this is the main topic of this paper and a companion paper [50] (hereafter Paper I). In Paper I, we examined the detectability of the angular momentum exchange of EMRIs with an ambient accretion disk using a large class of torque models parameterized by two free parameters. In particular, we pointed out that planetary migration models are examples that generate a very significant GW phase shift for LISA.

In this paper, we begin by reviewing the astrophysical models of the most important accretion-disk effects on EMRIs in AGNs, many of which were not included in Paper I. We focus on standard radiatively-efficient thin disks, where the viscosity is proportional to the total pressure (Shakura-Sunyaev α -disks [36]) or proportional to gas pressure only (which we refer to as β -disks) [51]. These disks constitute the standard model of luminous AGN accretion disks (see Refs. [31, 52] and Sec. III below). For both of these models, we include a more detailed analysis of the effects considered previously (SMBH mass accretion, CO mass accretion, hydrodynamic drag, torques from spiral density waves and resonant interactions), investigating the detailed circumstances under which such effects are possible or suppressed, and derive the effects of axisymmetric disk self-gravity on GWs, which was not considered before. We provide a detailed study of the consequences on the GW observable, using a few GW data analysis tools.

³ See Sec. III for further details on Shakura-Sunyaev α -disk models.

The analysis presented here is by no means exhaustive. For simplicity, we restrict attention to EMRIs on non-inclined, quasi-circular orbits. This restriction does not allow us to model binaries in which eccentricity is excited in the presence of an accretion disk [46, 47, 53–55]. Other effects that we do not discuss here include the following: GWs generated by accretion flows through the excitation of BH quasinormal modes [56–61]; GW energy flux dissipation by an ambient viscous disk, driving transverse and longitudinal density waves [62] that could heat the disk significantly and result in an observable infrared flare [63]; EM radiation generated by GWs in a strongly magnetized plasma, boosting the frequency of photons [64, 65], driving magnetosonic waves [66], focusing of EM radiation [67], generating photons in a static magnetic field [68, 69] and photons back-converting to GWs in a magnetized plasma [70–72]. We also do not consider the direct scattering of GWs by the gravity of the gas, nor the GW radiation of spiral arms in the disk. Clearly, these effects are interesting and should be studied in more detail, but they go beyond the scope of this paper.

C. Executive Summary of Results

This sub-section of the introduction is an executive summary of our main results, intended for non-specialists or for readers who might not be interested in all the related technical details of the paper, considering its length.

We derive the necessary conditions for the tidal effect of the CO to open a gap in radiation-pressure dominated α and β -disks. We find that EMRIs can open gaps at large radii in both α and β -disks. Depending on the EMRI masses and accretion disk parameters, the gap typically closes during the inspiral due to strong radiation-pressure gradients. Gap refilling occurs at orbital separations outside (inside) the LISA frequency band at orbital radii (in geometric units, see Sec. I D) $r \gtrsim 300$ ($24 M_\bullet$) for α (β) disks, under typical EMRI parameters [SMBH and CO masses of $(M_\bullet, m_\star) = (10^5, 10) M_\odot$]. Complete gap refilling occurs within 9 months in β -disks for these EMRI masses, well before the inspiral terminates in coalescence. This implies that bright AGN activity is coincident with LISA EMRIs in both cases.

We calculate the perturbations of the GW waveforms for quasi-circular, non-inclined EMRI orbits, due to the effects of mass accretion onto the SMBH and the CO, the hydrodynamic drag caused by an azimuthal and radial wind, and the axisymmetric and non-axisymmetric gravitational effects of the disk. Some of these effects lead to a strong imprint on the GW phase, while others do not.

We find that the gravitational torque from spiral density waves in the accretion disk (also known as *migration* torque in planetary dynamics) provides the most significant deviation from vacuum EMRI dynamics. Migration leads to the strongest GW imprints when the CO clears

a gap, leading to gas accumulation near the outer edge of the gap, like in a hydroelectric dam. The CO's mass accretion also leaves a significant imprint on the GW signal, if described by spherical BHL accretion [17]. However, we find that the CO accretion rate is significantly reduced by many processes, predominantly by limited gas supply and radiation pressure. Accounting for these limitations, the GW signature due to the CO's mass accretion is typically much smaller than that of migration. If tidal torques from the CO open a gap, the mass accretion onto the CO may be greatly reduced. All other effects are typically less significant.

We calculate the effect of all of the above mentioned processes on the GW observables, namely the waveform amplitude and phase, both with a leading-order Newtonian waveform model as well as with a relativistic effective-one-body (EOB) model [73–75]. Figure 1 summarizes the imprint of such processes on the Newtonian phase for the dominant GW mode as a function of the final orbital radius for a one-year observation. Different curve colors correspond to the phase difference between vacuum GW phases and those that include various disk effects, while solid and dotted lines correspond to α and β -disks respectively. We provide simple asymptotic analytical formulas describing the phase shift perturbation for arbitrary accretion disk, EMRI, and observation time parameters in Eqs. (115–116) and Table II in Sec. VIII. Figure 1 shows that the GW phase is modified significantly for EMRIs relevant to LISA (those with masses $(M_\bullet, m_\star) = (10^5, 10)$ and final orbital radii $r_f \lesssim 50 M_\bullet$) at 1 Gpc and an observing time of one year. The upper and lower thick magenta lines represent a rough measure of LISA sensitivity to the phase shift for a source at 1 Gpc and 10 Mpc, respectively.

The various curves in Figure 1 exhibit interesting features at different radii, which correspond to different astrophysical mechanisms that come into play. Most notably, the big decrease for the blue migration curves at $r \lesssim 24 M_\bullet$ correspond to a transition from Type-II to Type-I migration as the gap refills for β -disks. Coincidentally, roughly interior to that radius, BHL accretion and hydrodynamic drag from azimuthal winds are activated. The wiggles and the cutoff in the BHL accretion induced phase shift (black curves) correspond to a variety of effects. For α -disks (solid black curve), the gas density and sound speed determine the BHL accretion rate at small separations. At larger radii, the Bondi accretion radius becomes larger than the disk thickness, reducing the accretion rate. Even farther out, differential rotation of the disk reduces the BHL rate and the decrease in the average background radial gas velocity makes the amount of gas supply an important limitation. In the innermost region of the disk, photon diffusion is slow and the radiation is trapped within the BHL flow leading to super-Eddington accretion rates. However, at $r \gtrsim 35 M_\bullet$ this is no longer true for an α -disk and the flow becomes Eddington limited, greatly reducing BHL accretion effects.

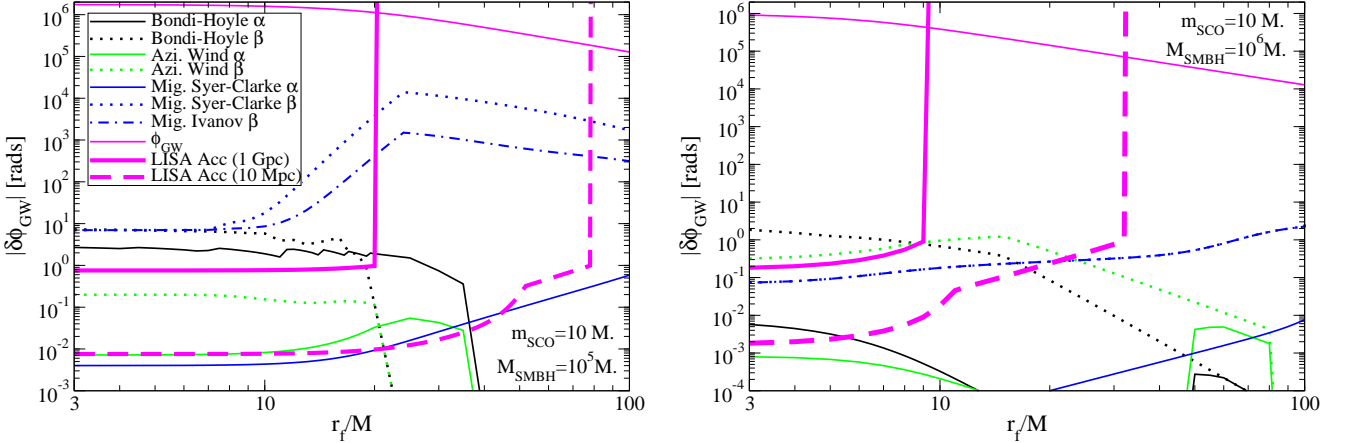


FIG. 1. The GW phase shift as a function of final radius in units of M_\bullet induced by different accretion disk effects relative to vacuum waveforms (see Sec. ID for the conventions used here). Solid (dotted) curves correspond to α (β) disks, with different colors indicating different disk effects: black corresponds to Bondi-Hoyle-Lyttleton (BHL) accretion, green to azimuthal wind and blue to migration. The thin, solid magenta line is the total accumulated GW phase in vacuum. The thick, solid (dashed) magenta line corresponds to a measure of the accuracy to which LISA can measure the GW phase for a source at 1 Gpc (10 Mpc). Observe that certain disk effects, like migration, can leave huge imprints on the GW observable, inside the LISA accuracy bucket.

Relativistic waveform models yield similar results to those presented in Fig. 1. After aligning the waveforms in time and phase (equivalent to a maximization of the SNR over the corresponding extrinsic parameters in white noise), we find changes in the GW phase after a typical one-year inspiral of up to $\mathcal{O}(10^4)$ radians when modeling migration in β -disks. Migration effects for α -disks are much smaller, since these disks are less dense. As the gap is typically expected to close for EMRIs in the most sensitive LISA frequency band ($r \lesssim 25M_\bullet$), Type-I migration is the most relevant process. Supply-limited, BHL accretion and wind effect lead to a dephasing of $\mathcal{O}(1)$ rads. Other effects are less significant: $\mathcal{O}(10^{-3})$ radians for SMBH mass accretion, and $\mathcal{O}(10^{-4})$ radians for axisymmetric self-gravity effects.

We then proceed with a more careful data analysis study on the distinguishability of accretion disk effects by computing a data analysis measure for two representative systems at 1 Gpc with component masses $(10, 10^5) M_\odot$ and $(10, 10^6) M_\odot$, respectively. We calculate the SNR in the waveform *difference* between signals accounting for accretion disk perturbations and those that do not, marginalizing over an overall time and phase shift. We find that, for these systems, $\rho(\delta h) > 10$ after just 4 months of evolution for β -disk migration, while it takes one full year of integration to reach the same SNR for BHL accretion and wind effects. All other accretion disk effects are less significant.

Finally, we examine possible degeneracies between accretion disk effects and vacuum EMRI parameters. We analytically derive the Fourier transform of the waveforms in the stationary phase approximation. We find that the disk-induced perturbation to the frequency-

domain GW phase depends on the GW frequency to a high negative power relative to the Newtonian term, multiplied by a function of the initial binary masses, the α -disk parameter and the SMBH accretion rate \dot{m}_\bullet . In contrast, the phase of the Fourier transform of vacuum waveforms is a positive power of frequency relative to the Newtonian term, when including post-Newtonian (PN) corrections. The difference in the frequency scaling arises because the accretion disk effects grow with orbital separation (lower frequency), as opposed to PN corrections which grow with decreasing separation (higher frequency). This suggests that accretion disk effects are not strongly correlated with general relativistic vacuum terms in the frequency-domain GW phase. Whether this statement holds in a realistic data analysis implementation requires a much more detailed analysis of the likelihood surface that is beyond the scope of this paper.

Our results suggest that if a GW signal is detected from an EMRI in an accretion disk, then matched filtering with accretion disk templates could allow for the measurement of certain disk parameters to an interesting fractional accuracy (early estimates suggest 10% accuracy for certain parameters [76]). The precise magnitude of the latter requires the detailed mapping of the likelihood surface with relativistic EMRI signals, full Fourier transforms, and improved disk modeling (including relativistic effects and magnetic fields), which is beyond the scope of this paper.

We caution, however, that the models considered here might not provide a fully realistic description of the angular momentum exchange between the binary and the accretion disk, leading to systematic theoretical uncertainties in interpreting GW measurements. Since EM

observations of the disk luminosity are also sensitive to \dot{m}_\bullet , the combination of contemporaneous EM and GW observations might hold the key for constraining the accretion disk physics most reliably.

D. Organization and Conventions

This paper is aimed at both the General Relativity and Astrophysics communities. We present a significant amount of background material to make the paper self-contained for both communities. Sec. II reviews the basics of EMRIs as relevant to GW physics and a rough measure of the accuracy to which the waveforms need to be computed for LISA parameter estimation. Sec. III presents the basic elements of the thin accretion disk models that are considered in this paper, and derives the necessary conditions for tidal effects to open a gap in the disk around the secondary. Sec. IV studies the effect of binary mass increase due to gas accretion on the GW signal. Sec. V focuses on the effect of hydrodynamic drag on the GW signal, induced by the gas velocity relative to the CO (i.e. wind). Sec. VI discusses the effects of the axisymmetric gravity of the disk. Sec. VII concentrates on gravitational angular momentum exchange with the disk (i.e. migration) and its effects on the GW signal. Sec. VIII compares and contrasts the effect of the different accretion disk effects on the GW phase. Sec. IX describes the theoretical framework through which we compute effective-one-body waveforms in the presence of an accretion disk. Sec. X performs a simple data analysis study to infer the detectability of accretion disk effects. Finally, Sec. XI concludes and suggests future work.

Throughout the paper, we employ the following conventions. We use geometric units with $G = c = 1$ unless otherwise noted. This implies that masses are in units of length or time, where the mapping is simply $M_\odot = 1.476 \text{ km} = 4.92 \mu\text{s}$. The EMRI is assumed to be composed of a SMBH with mass M_\bullet and a CO with mass m_\star . The SMBH is assumed to be spinning with spin angular momentum $S_\bullet = a_\bullet M_\bullet$, aligned with the orbital one. We do not model here the spin of the CO. We measure quantities relative to their typical magnitudes and denote $A_b = A/(10^b M_\odot)$. For example, $M_{\bullet 5} = M_\bullet/(10^5 M_\odot)$ and $m_{\star 1} = m_\star/(10 M_\odot)$. The radial orbital separation is always scaled in terms of the SMBH's mass, such that $\bar{r} \equiv r/M_\bullet$. The natural scale for the start and end of observation in the most sensitive part of the LISA band is $20M_\bullet$ and $10M_\bullet$, so we use $\bar{r}_{20} = r/(20M_\bullet)$ and \bar{r}_{10} accordingly. We use r' to denote distance from the CO to a field point.

II. REVIEW OF EMRI GWS

We start by reviewing some basic facts about EMRI dynamics, focusing only on leading-order effects. Sec. IX

provides a more detailed analysis that includes higher-order relativistic effects.

A. Basics of EMRI Dynamics

Since the CO orbits very close to the SMBH, GR effects cause the largest perturbations of Newtonian orbits. In this section we consider eccentric EMRI dynamics, although in most of what follows we restrict our attention to quasi-circular EMRIs. In the absence of spin, the binary's energy is

$$\frac{E}{m_\star} = \frac{1}{2} M_\bullet^2 \Omega^2 \bar{r}^2 - \frac{1}{\bar{r}} = -\frac{1}{2\bar{r}}, \quad (1)$$

the Keplerian orbital frequency is

$$\Omega = M_\bullet^{-1} \bar{r}^{-3/2}, \quad (2)$$

where $\bar{r} \equiv r/M_\bullet$ is the semi-major axis of the orbit in units of M_\bullet . Apsidal or pericenter precession for an orbit with eccentricity e is

$$\Omega_{\text{GR,ap}} = 3M_\bullet^{-1}(1-e^2)^{-1}\bar{r}^{-5/2}, \quad (3)$$

while Lense-Thirring precession of the node of an inclined orbit around a spinning SMBH is

$$\Omega_{\text{LT}} = 2a_\bullet M_\bullet^{-1} \bar{r}^{-3}. \quad (4)$$

The CO inspiral produces GWs that remove binding energy and specific angular momentum from the system at the rate

$$\dot{E}_{\text{GW}} = -\frac{32}{5} \frac{m_\star^2}{M_\bullet^2} \frac{g_1(e)}{\bar{r}^5} = -6.4 \times 10^{-13} \frac{m_{\star 1}^2}{M_{\bullet 5}^2} \frac{g_1(e)}{\bar{r}_{10}^5}, \quad (5)$$

$$\dot{\ell}_{\text{GW}} = -\frac{32}{5} \frac{m_\star}{M_\bullet} \frac{g_2(e)}{\bar{r}^{7/2}} = -2 \times 10^{-7} \frac{m_{\star 1}}{M_{\bullet 5}} \frac{g_2(e)}{\bar{r}_{10}^{7/2}}, \quad (6)$$

to leading order in $m_\star \ll M_\bullet$, where $\bar{r}_{10} = \bar{r}/10$ and where

$$g_1(e) = \frac{1 + \frac{73}{24}e^2 + \frac{37}{96}e^4}{(1-e^2)^{7/2}}, \quad g_2(e) = \frac{1 + \frac{7}{8}e^2}{(1-e^2)^2}. \quad (7)$$

We have here introduced the notation $A_b = A/(10^b M_\odot)$ for any quantity A , such that $M_{\bullet 5} = M_\bullet/(10^5 M_\odot)$ and $m_{\star 1} = m_\star/(10 M_\odot)$.

Such loss of energy and angular momentum leads to the decrease of the semi-major axis and eccentricity at a rate

$$\dot{r}_{\text{GW}} = -\frac{64}{5} \frac{m_\star}{M_\bullet} g_1(e) \bar{r}^{-3} = -1.3 \times 10^{-6} \frac{m_{\star 1}}{M_{\bullet 5}} g_1(e) \bar{r}_{10}^{-3} \quad (8)$$

$$|\dot{e}_{\text{GW}}| = \frac{304}{15} \frac{m_\star}{M_\bullet^2} g_3(e) \bar{r}^{-4} = 2 \times 10^{-12} M_\odot^{-1} \frac{m_{\star 1}}{M_{\bullet 5}^2} g_3(e) \bar{r}_{10}^{-4}$$

where we have defined

$$g_3(e) = \frac{e(1 + \frac{121}{304}e^2)}{(1-e^2)^{5/2}}. \quad (9)$$

Equivalently, we can parameterize the orbit in terms of the change in the orbital frequency

$$\dot{\Omega}_{\text{GW}} = \frac{96}{5} \frac{m_{\star}}{M_{\bullet}^3} g_1(e) \bar{r}^{-11/2} \quad (10)$$

For quasi-circular orbits, several formula simplify. For example, one can easily see that $\dot{E}_{\text{GW}} = \Omega \dot{L}_{\text{GW}}$. Similarly, the inward inspiral velocity $v_{\star r}$ is simply given by Eq. (8) with $g_1(e) \rightarrow 1$. The orbital evolution of the semi-major axis, Eq. (8), can be integrated [77, 78] for quasi-circular orbits,

$$\bar{r}_0 = \bar{r}_f \left(1 + \frac{\tau}{\bar{r}_f^4} \right)^{1/4}, \quad \text{where } \tau \equiv \frac{256}{5} \frac{m_{\star}}{M_{\bullet}^2} T. \quad (11)$$

and where \bar{r}_0 and \bar{r}_f are the initial and final separations in units of M_{\bullet} for an observation time T . Let us define the critical radius and observation time where \bar{r}_f starts to deviate significantly from \bar{r}_0 as

$$\bar{r}_{f,\text{crit}} \equiv \tau^{1/4} = 24 m_{\star 1}^{1/4} M_{\bullet 5}^{-1/2} T_{\text{yr}}^{1/4}, \quad (12)$$

$$T_{\text{crit}} \equiv \frac{5}{256} \frac{M_{\bullet}^2}{m_{\star}} \bar{r}_f^4 = 0.031 \text{ yr} \frac{M_{\bullet 5}^2}{m_{\star 1}} \bar{r}_{f,10}^4. \quad (13)$$

The measured GW phase to leading order is twice the orbital phase for a quasi-circular orbit $\phi_{\text{GW}} = 2\phi_{\text{orb}}$. The total accumulated phase for a quasi-circular inspiral is then

$$\begin{aligned} \phi_{\text{GW}} &= 2 \int_{t_f - T_{\text{obs}}}^{t_f} \Omega(t) dt = 2 \int_{\bar{r}_0}^{\bar{r}_f} \Omega(\bar{r}) \frac{d\bar{r}}{\dot{\bar{r}}} \\ &= \frac{1}{16} \frac{M_{\bullet}}{m_{\star}} \bar{r}_f^{5/2} \left[\left(1 + \frac{\tau}{\bar{r}_f^4} \right)^{5/8} - 1 \right] \end{aligned} \quad (14)$$

where τ is the dimensionless observation time defined in Eq. (11), and \bar{r}_f is the final radius at the end of the observation. Depending on whether the observation time is short or long compared to the inspiral timescale $\tau/\bar{r}_f^4 \ll 1$ or $\tau/\bar{r}_f^4 \gg 1$, Eq. (14) becomes

$$\phi_{\text{GW}}^{\text{short}} \approx 4 \times 10^6 \text{ rads} \frac{T_{\text{yr}}}{M_{\bullet 5} \bar{r}_{f,10}^{3/2}} \left(1 - 6 \frac{m_{\star 1}}{M_{\bullet 5}^2} \frac{T_{\text{yr}}}{\bar{r}_{f,10}^4} \right) \quad (15)$$

$$\phi_{\text{GW}}^{\text{long}} \approx 2 \times 10^6 \text{ rads} \frac{T_{\text{yr}}^{5/8}}{M_{\bullet 5}^{1/4} m_{\star 1}^{3/8}} \left(1 - 0.1 \frac{M_{\bullet 5}^{5/4}}{m_{\star 1}^{5/8}} \frac{\bar{r}_{f,10}^{5/2}}{T_{\text{yr}}^{5/8}} \right) \quad (16)$$

for short observations or widely separated binaries ($T \ll T_{\text{crit}}$ and $\bar{r}_f \gg \bar{r}_{f,\text{crit}}$), and long observations or close-in orbits ($T \gg T_{\text{crit}}$ and $\bar{r}_f \ll \bar{r}_{f,\text{crit}}$), respectively.⁴

Equations (15–16) show that initially the GW phase accumulates quickly as $c_1 T + c_2 T^2$, but then saturates to a rate $c_3 T^{5/8}$, where c_i are time-independent constants. Setting $m_{\star} = 10 M_{\odot}$ and $M_{\bullet} = 10^5 M_{\odot}$, we find that $\phi_{\text{GW}} \sim \mathcal{O}(10^6)$ rads in a one year observation.

B. Measures of LISA Sensitivity to GWs

GW detectors are most sensitive to the phase of the GW signal. Since EMRIs can accumulate millions of GW cycles in the detector's sensitivity band, they make for excellent probes of the astrophysical environment.

1. Simple Mass and Time-Scale Measures

A rough measure of the accuracy to which LISA can extract parameters can be derived by looking at the mass measurement accuracy. This quantity is of order [10]

$$\frac{\delta M_{\bullet}}{M_{\bullet}} \sim \frac{\delta m_{\star}}{m_{\star}} \sim \frac{10^{-3}}{\rho}, \quad (17)$$

where ρ is the SNR (see below). The SNR can be roughly as large as a few tens for a $10 M_{\odot}$ CO spiraling into a $10^6 M_{\odot}$ within $\bar{r} \lesssim 10M$ at a distance of 1 Gpc. Thus, the relative mass estimation precision is at best around $10^{-4} - 10^{-5}$ [10]. Of course, for less distant sources, the SNR can be larger, allowing a better determination of the masses. This mass accuracy, compared to the accretion mass or local disk mass, provides a rough measure of whether the disk may generate important perturbations for LISA.

Another rough measure to decide whether certain effects are important for LISA is the following. If a perturbation has an associated timescale \mathcal{T} on which it changes the inspiral phase by a factor of order unity, then the magnitude of the phase correction corresponding to this process is roughly

$$\delta\phi_{\text{GW}} \sim \frac{T_{\text{obs}}}{\mathcal{T}} \phi_{\text{GW}}^{\text{tot}} \quad (18)$$

where $\phi_{\text{GW}}^{\text{tot}}$ is the total, accumulated GW phase in the observation. We assume here that this $\delta\phi$ is not a simple, constant phase shift, but a modification in the phase evolution, such that at the end of the observation, the template dephases from the signal by an amount $\delta\phi_{\text{GW}}$. LISA can detect phase differences of order a few radians (see below). Thus an effect is important if $\mathcal{T} \lesssim 4.4 \times 10^5$ yrs for a single year observation, see Eq. (14). In practice, $\mathcal{T} \equiv x/\dot{x}$ may be used where $x(t)$ represents any of the following physical quantities: the mass of the SMBH or CO, the induced angular momentum or energy dissipation rate relative to the GW-driven dissipation rates, the inspiral rate relative to the GW inspiral rate, or the frequency shift relative to the Keplerian frequency.

⁴ We note that $\phi_{\text{GW}}^{\text{long}}$ is the standard PN expression for the phase evolution as a function of time [79], when the phase evolution culminates in merger. Individual EMRIs, however, may outlive LISA observations, which is why we choose to use Eq. (14) along with the asymptotes Eq. (15–16).

2. Dephasing Measure

A more accurate criterion to decide whether a certain GW modification is detectable for LISA is:

$$\delta\phi_{\text{GW}} \geq \begin{cases} 10/\rho & \text{if } \rho \geq 10, \\ 0 & \text{if } \rho \leq 10, \end{cases} \quad (19)$$

where ρ^2 is the square of the signal-to-noise ratio (SNR), defined as

$$\rho^2(h) = 4 \int \frac{df}{S_n(f)} |\tilde{h}|^2. \quad (20)$$

The quantity \tilde{h} is the Fourier transform of the measured GW strain amplitude and $S_n(f)$ is the spectral noise density curve of the detector. Accounting for white-dwarf confusion noise and not averaging over sky-angles, the noise curve is

$$S_n(f) = \min \left\{ S^{\text{NSA}} e^{4.5T_{\text{yr}}^{-1}N'}, S^{\text{NSA}} + S^{\text{gal}} \right\} + S^{\text{ex-gal}}, \quad (21)$$

where $(S^{\text{NSA}}, S^{\text{gal}}, S^{\text{ex-gal}}, N')$ are functions of frequency, that can be found, for example, in [7]. We account for sky position and binary orientation averaged response functions and noise curves, by multiplying Eq. (21) by a prefactor of 20/3.

Equation (19) is motivated by the following arguments. Any accretion disk effect is measurable only if the EMRI is detected in the first place. We have here conservatively chosen $\rho \geq 10$ as the threshold for detection. Once the EMRI is detected, the accuracy to which a phase difference can be measured is roughly $10/\rho$, where ρ is the total SNR.

Let us now relate this phase shift measure to the SNR of the waveform difference between signals that include and those that neglect disk effects: $\delta\tilde{h} \equiv \tilde{h}_1 - \tilde{h}_2$. If these waveforms differ only in phase by an amount $\delta\phi_{\text{GW}}$, then

$$\delta\tilde{h} = \tilde{h}_1 (1 - e^{i\delta\phi_{\text{GW}}}). \quad (22)$$

The SNR of the difference is then

$$\begin{aligned} \rho^2(\delta h) &= 4 \int \frac{df}{S_n(f)} |\delta\tilde{h}|^2, \\ &= 8 \int \frac{df}{S_n(f)} |\tilde{h}_1|^2 [1 - \cos(\delta\phi_{\text{GW}})], \\ &\sim 4 \int \frac{df}{S_n(f)} |\tilde{h}_1|^2 \delta\phi_{\text{GW}}^2, \end{aligned} \quad (23)$$

where in the last line we have assumed that $\delta\phi_{\text{GW}} \ll 1$ rad.

The perturbation of the waveform is significant if $\rho(\delta h) \gtrsim 10$, which is similar to the accuracy requirements constructed in [80–82]. If the instantaneous SNR, $|\tilde{h}_1|^2 S_n^{-1}(f)$ does not vary greatly while the phase difference accumulates, then $\rho(\delta h) \sim (\delta\phi_{\text{GW}})\rho(h_1)$ for $\delta\phi_{\text{GW}} \ll 1$ rad, which leads to the simple phase shift criterion, Eq. (19), above.

3. Degeneracies and Template Placement

One can generalize the above measures by allowing for both amplitude and phase modifications. The SNR of the waveform difference then becomes

$$\rho^2(\delta h) \equiv \min_{\lambda_2} \left[4 \int \frac{df}{S_n(f)} \left| \tilde{h}_1(f) - \tilde{h}_2(f; \lambda_2) \right|^2 \right], \quad (24)$$

where \tilde{h}_1 and \tilde{h}_2 are the Fourier transforms of two waveforms (the “signal” and “template”), normalized such that $\rho(h_1) = \rho(h_2) = 1$. The template may depend on free parameters λ_2 that may be different from the true astrophysical values, where the minimum difference corresponds to the best fit. Expanding Eq. (24), we find $\rho^2(\delta h) = 2MM$, where $MM = 1 - \mathcal{O}$ is the mismatch and

$$\mathcal{O}(h_1, h_2) \equiv \max_{\lambda_2} \left[4\Re \int \frac{df}{S_n(f)} \tilde{h}_1(f) \tilde{h}_2^*(f; \lambda_2) \right]. \quad (25)$$

is the overlap.

For a simple estimate, we minimize $\rho^2(\delta h)$ over certain non-physical *extrinsic parameters* only, i.e. an overall phase and time shift, as opposed to *intrinsic parameters*, such as the binary’s masses or spins, or other extrinsic parameters, such as the distance to the source, the polarization angles or the sky position. When the SNR of the difference is computed in this way, estimates of measurability are optimistic as they do not account for possible degeneracies between all parameters. For example, a signal $h_1(f, \vec{\lambda}_1)$ with true parameters λ_1 may be mimicked by a waveform model $h_2(f, \vec{\lambda}_2)$ with different intrinsic parameters $\vec{\lambda}_2 \neq \vec{\lambda}_1$, even if the extrinsic parameters are the same. In Sec. XC we show that the incorrect determination of EMRI parameters in a fiducial model (e.g. with no accretion disk) cannot mimic the waveform of a different model (e.g. including the effects of an accretion disk), because of the particular spectral features introduced by accretion disks in the Fourier transform of the response function.

III. REVIEW OF ACCRETION DISK MODELS

We proceed with an overview of the accretion disk models under consideration. As this paper aims to bridge between the accretion disk astrophysics community and GW physics community, we have chosen to provide a complete description of background material.

A. Basics of Accretion-Disk Models

Despite a long history of observational, theoretical, and numerical investigations, accretion disks remain one of the most exciting unsolved problems in astrophysics. The complexity is related to the modeling of magnetohydrodynamic (MHD) flows, turbulence, radiative transport,

and plasma physics. Here we provide a brief overview of the formulas used to model accretion disks; for more details see textbooks by Shapiro & Teukolsky [31] and Frank et. al. [52].

We restrict our attention to geometrically thin, radiatively efficient, stationary accretion disks, responsible for the observed bright emission around AGNs. In this case, as gas orbits around the central object, it radiates thermal energy away much faster than the timescale over which the gas particles drift inward, and the disk maintains a thin configuration. Radiatively efficient disks are the most massive among accretion disks, as the mass accretion rate is largest and the inward drift velocity is smallest. For lower radiative efficiencies around quiescent SMBHs, accretion is described by other models, such as advection-domination, which we ignore here.

Radiatively-efficient, stationary accretion disks can be described by the Shakura-Sunyaev α -disk model [31, 36]. The $t_{r\phi}$ component of the viscous stress tensor corresponds to an effective viscosity⁵ $t_{ij} = \rho v \nabla_i v_j$ and it is responsible for the slow inflow of gas. In the α -disk model, the viscous stress is assumed to be proportional to the total pressure p_{tot} in the disk at each radius: $t_{r\phi} = -(3/2)\alpha p_{\text{tot}}$. The total pressure includes both thermal gas pressure and radiation pressure, and the dimensionless constant of proportionality α is a free model parameter. These disks are viscously, thermally, and convectively unstable to linear perturbations [83–86]. In the alternative model [51], hereafter denoted β -disks, viscous stress is proportional to the gas pressure only, $t_{r\phi} = -(3/2)\alpha p_{\text{gas}}$, and such models are stable.⁶

The nature of viscosity, however, is not sufficiently well-understood to predict which of these prescriptions is closer to reality. Recent MHD numerical simulations of accretion disks indicate that stresses correlate with total pressure as in the α -disk model [87] and are thermally stable [88], though they might be viscously unstable [89]. In cases where the diffusion scale is larger than the wavelength of the magneto-rotational instability, other simulations are consistent with the β -disk model [90, 91]. The instability in α -disks implies spectral variations which are not observed in many systems, while the β -disk model provides a better match to spectral constraints [92]. In this paper, we remain agnostic about the disk model and carry out calculations for both of them.

Shakura-Sunyaev α and β -disks for a BH of fixed M_\bullet mass are described by two free parameters: the accretion rate \dot{M}_\bullet and the α parameter in the viscosity prescription. AGN observations show that the accretion rate relative to the Eddington rate⁷, $\dot{m}_\bullet \equiv \dot{M}_\bullet / \dot{M}_{\bullet,\text{Edd}}$, is typ-

ically around 0.1–1 with a statistical increase towards higher luminosities [93, 94]. Theoretical limits based on simulations of MHD turbulence around BHs are inconclusive, but are consistent with α in the range 0.001–1 [95]. Its estimated value in protoplanetary accretion disks is lower, $\alpha \lesssim 10^{-3}$ [96]. Observations of outbursts in binaries with an accreting WD, NS, or stellar BH imply $\alpha = 0.2$ –0.4 [97, 98]. The value of α in AGN accretion disks is uncertain, but might be expected to be similar (for a review, see Ref. [98]). In the following, we assume

$$\dot{m}_{\bullet,1} \equiv \frac{\dot{m}_\bullet}{0.1} = 1, \quad \epsilon_1 \equiv \frac{\epsilon}{0.1} = 1, \quad \alpha_1 \equiv \frac{\alpha}{0.1} = 1, \quad (26)$$

but retain $\dot{m}_{\bullet,1}$ and α_1 to be able to describe different values. Here ϵ is the radiation efficiency (see Eq. (51) below).⁸

The surface density, $\Sigma(\bar{r})$, and the scale height of the disk from the mid-plane, $H(\bar{r})$, can be calculated as [16],

$$\Sigma(\bar{r}) = \frac{2^{4/5} \sigma_{\text{SB}}^{1/5}}{3\pi^{3/5} f_T^2 \kappa^{1/5}} \left(\frac{\mu_0 m_p}{k_B \alpha} \right)^{4/5} \dot{M}_\bullet^{3/5} \Omega^{2/5} \beta^{4(1-b)/5}, \quad (27)$$

$$H(\bar{r}) = \frac{f_T \kappa \dot{M}_\bullet}{2\pi c(1-\beta)}. \quad (28)$$

where $b = 0$ for α -disks and 1 for β -disks, and the radial dependence is implicit in the orbital velocity $\Omega = M_\bullet^{-1} \bar{r}^{-3/2}$ and β . Here, $\beta(\bar{r}) \equiv p_{\text{gas}}/p_{\text{tot}}$, where $p_{\text{tot}} = p_{\text{gas}} + p_{\text{rad}}$, p_{gas} is the thermal gas pressure, p_{rad} is the radiation pressure, and β satisfies

$$\frac{\beta^{(1/2)+(1/10)(b-1)}}{1-\beta} = \frac{2^{3/5} \pi^{4/5} c}{\sigma_{\text{SB}}^{1/10} \alpha^{1/10} \kappa^{9/10}} \left(\frac{k_B}{\mu_0 m_p} \right)^{2/5} \times \dot{M}_\bullet^{-4/5} \Omega^{-7/10}, \quad (29)$$

with $\mu_0 = 2/(3X_H + 1) = 0.615$ the mean molecular weight, k_B the Boltzmann constant, σ_{SB} the Stefan-Boltzmann constant, and $f_T = 3/4$ a constant related to the assumption of optical depth (see [99]). The quantity $\kappa = \mu_e \sigma_T / m_p$ is the electron scattering opacity in the medium, with μ_e the number density of electrons relative to the total density, m_p the proton mass, and σ_T the Thompson scattering cross-section. In practice $\mu_e = (1 + X_H)/2 = 0.875$ and $\kappa = 0.348 \text{ cm}^2 \text{ g}^{-1}$ for a fully ionized gas of hydrogen and helium, where the mass fraction of hydrogen is $X_H = 0.75$. Equation (29) can be solved numerically for $\beta(\bar{r})$ at each radius and substituted in Eqs. (27–28) to obtain $\Sigma(\bar{r})$ and $H(\bar{r})$. The kinematic viscosity coefficient in the disk is

$$\nu = \alpha \beta^b H c_s = \frac{\dot{M}_\bullet}{3\pi \Sigma} \quad (30)$$

⁵ Throughout this section $\rho \equiv \rho(r)$ denotes gas density (i.e. not the SNR of GWs), ν is the kinematic viscosity coefficient in units of cm^2/s , and v is the gas velocity.

⁶ Another popular model that is stable assumes $t_{r\phi} = -(3/2)\alpha \sqrt{p_{\text{gas}} p_{\text{tot}}}$.

⁷ We define the Eddington rate $\dot{M}_{\bullet,\text{Edd}}$ more precisely in Eq. (54) below.

⁸ Note that in all of our formulas $\dot{m}_{\bullet,1}$ and ϵ_1 always appear in the combination $\dot{m}_{\bullet,1}/\epsilon_1$. To simplify notation we suppress the ϵ_1 scaling.

[100].

Equations (27–29) give a self-consistent non-relativistic description of a geometrically thin, radiatively efficient, stationary accretion disk, provided the following conditions are satisfied: the disk is optically thick to electron scattering, opacity is dominated by electron scattering, the disk is hot enough to be fully ionized, the self-gravity of the gas is negligible relative to the gravity of the accreting object, and the modifications near the inner boundary condition are neglected (see below). These conditions are all satisfied within $6 \ll \bar{r} < 10^3$ for $M_\bullet < 10^7 M_\odot$, $\dot{m} > 0.1$, $\alpha > 0.1$ [99]. Equation (29) shows that well within

$$\bar{r}_{\text{rad}} = 600 \dot{m}_{\bullet 1}^{16/21} \alpha_1^{2/21} M_{\bullet 5}^{2/21}, \quad (31)$$

$\beta \ll 1$ holds, so that radiation pressure dominates over thermal gas pressure. In this case, Eq. (29) can be inverted analytically

$$\beta(\bar{r}) \approx 4.3 \times 10^{-4} \alpha_1^{-1/5} \dot{m}_{\bullet 1}^{-8/5} M_{\bullet 5}^{-1/5} \bar{r}_{10}^{21/10} \quad \text{for } \beta\text{-disks} \quad (32)$$

and Eqs. (27–28) simplify to

$$\begin{aligned} \Sigma(\bar{r}) &\approx \begin{cases} 538.5 \text{ g cm}^{-2} \alpha_1^{-1} \dot{m}_{\bullet 1}^{-1} \bar{r}_{10}^{-3/2} & \text{for } \alpha\text{-disks,} \\ 1.262 \times 10^6 \text{ g cm}^{-2} \alpha_1^{-4/5} \dot{m}_{\bullet 1}^{3/5} M_{\bullet 5}^{1/5} \bar{r}_{10}^{-3/5} & \text{for } \beta\text{-disks,} \end{cases} \\ &= \begin{cases} 5.907 \times 10^{-21} M_\odot^{-1} \alpha_1^{-1} \dot{m}_{\bullet 1}^{-1} \bar{r}_{10}^{-3/2} & \text{for } \alpha\text{-disks,} \\ 1.384 \times 10^{-17} M_\odot^{-1} \alpha_1^{-4/5} \dot{m}_{\bullet 1}^{3/5} M_{\bullet 5}^{1/5} \bar{r}_{10}^{-3/5} & \text{for } \beta\text{-disks,} \end{cases} \end{aligned} \quad (33)$$

$$H(\bar{r}) \approx 1.5 \dot{m}_{\bullet 1} M_\bullet = 1.5 \times 10^5 M_\odot \dot{m}_{\bullet 1} M_{\bullet 5}. \quad (34)$$

The disk scale height is the same for the two models in the radiation pressure dominated regime, approximately constant in radius. Note that the thin disk assumption $2H \ll r$ breaks down within $\bar{r} \lesssim 3\dot{m}_{\bullet 1}$. Since radiatively efficient thick disks have no widely accepted analytical models to date, we extrapolate Eqs. (27–28) to this regime, as well.

Equation (33) shows that β -disks are much more massive within $\bar{r} \ll 1000$. This is to be expected, as the effective viscosity is much smaller for β -disks relative to α -disks by a factor of order β . Since the orbital velocity of gas is different for different radii, viscosity leads to energy dissipation, and a slow radial inflow. A smaller viscosity implies a smaller radial inflow velocity, which for a fixed accretion rate corresponds to a larger mass.

The local disk mass near the binary in a logarithmic radius bin is defined as

$$\begin{aligned} m_d(\bar{r}) &= 4\pi r^2 \Sigma \\ &= \begin{cases} 7.4 \times 10^{-8} M_\odot \alpha_1^{-1} \dot{m}_{\bullet 1}^{-1} M_{\bullet 5}^2 \bar{r}_{10}^{7/2} & \text{for } \alpha\text{-disks,} \\ 1.7 \times 10^{-4} M_\odot \alpha_1^{-4/5} \dot{m}_{\bullet 1}^{3/5} M_{\bullet 5}^{11/5} \bar{r}_{10}^{7/5} & \text{for } \beta\text{-disks.} \end{cases} \end{aligned} \quad (35)$$

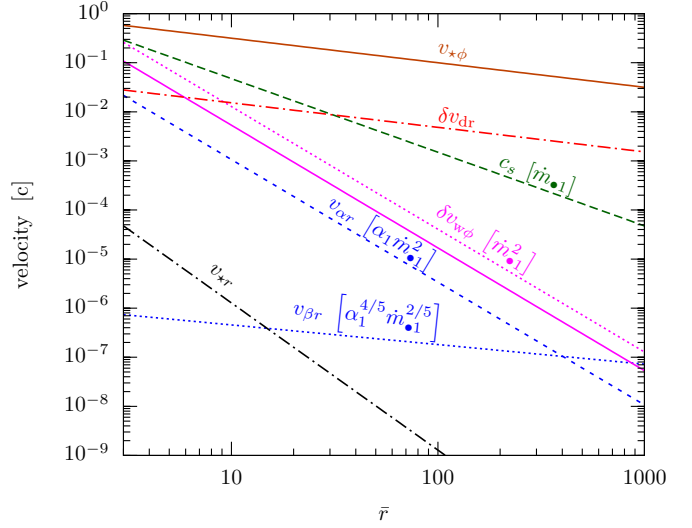


FIG. 2. The velocity scales in the problem as a function of radius. From top to bottom (with corresponding equations): Keplerian orbital velocity (2), differential rotation at the Hill's radius for β - and α -disks (37), isothermal sound speed (38), azimuthal wind (79), radial inflow velocity for α - and β -disks (37), and the GW radiation reaction inspiral velocity (8). The scalings with accretion disk parameters ($\alpha_1, \dot{m}_{\bullet 1}$) are as labelled. Fiducial parameters used: $\alpha_1 = \dot{m}_{\bullet 1} = M_{\bullet 5} = m_{\star 1} = 1$.

The gas density in the disk, the mean radial inflow velocity, and the isothermal sound speed are

$$\rho(\bar{r}) \equiv \frac{\Sigma}{2H} \quad (36)$$

$$\approx \begin{cases} 2.0 \times 10^{-26} M_\odot^{-2} \alpha_1^{-1} \dot{m}_{\bullet 1}^{-2} M_{\bullet}^{-1} \bar{r}_{10}^{-3/2} & \text{for } \alpha\text{-disks} \\ 4.6 \times 10^{-23} M_\odot^{-2} \alpha_1^{-4/5} \dot{m}_{\bullet 1}^{-2/5} M_{\bullet}^{-4/5} \bar{r}_{10}^{-3/5} & \text{for } \beta\text{-disks} \end{cases}$$

$$v_r^{\text{gas}}(\bar{r}) = \frac{3\nu}{2r} = -\frac{\dot{M}_\bullet}{2\pi r \Sigma} = -\frac{\dot{M}_\bullet r}{m_d} \quad (37)$$

$$\approx \begin{cases} -3.8 \times 10^{-4} \alpha_1 \dot{m}_{\bullet 1}^2 \bar{r}_{10}^{-5/2} & \text{for } \alpha\text{-disks} \\ -6.9 \times 10^{-7} \alpha_1^{4/5} \dot{m}_{\bullet 1}^{2/5} M_{\bullet 5}^{-1/5} \bar{r}_{10}^{-2/5} & \text{for } \beta\text{-disks} \end{cases}$$

$$c_s(\bar{r}) \equiv \sqrt{\frac{p_{\text{tot}}}{\rho}} = H\Omega \approx 0.047 \dot{m}_{\bullet 1} \bar{r}_{10}^{-3/2}. \quad (38)$$

where \dot{M}_\bullet is the SMBH accretion rate, defined more precisely in Sec. IV A.

Figure 2 compares the typical velocity scales in the problem for quasi-circular EMRIs. Typically, $|v_{r,\star}| \ll |v_{r,\beta}| \ll |v_{r,\alpha}| \ll c_s$ for $\bar{r} \gtrsim 10$, where $v_{r,\alpha}$ and $v_{r,\beta}$ corresponds to v_r^{gas} for α and β -disks. The figure also depicts other relevant velocity scales which we shall derive in Secs. IV and V below. Similarly, to get a feel of the typical disk mass scales, Figure 3 compares the MBH and EMRI mass, and the local disk masses for α and β -disks, as well as the CO accretion rate per year derived in Sec. IV B below. The local β -disk mass and

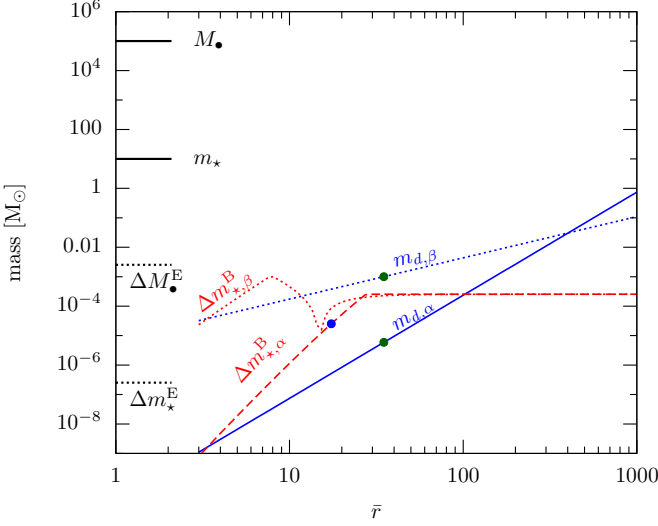


FIG. 3. The mass scales in the problem. Plotted are the MBH mass, M_\bullet , the EMRI mass, m_\star , the local disk mass, m_d , the accreted mass at Eddington rate after 1 yr (efficiency $\epsilon = 0.1$), $\Delta M_\bullet^E, \Delta m_\star^E$ (Sec. IV A), and the accreted mass at BHL rate onto the CO for the α and β -disks per year, $\Delta m_{\star\alpha,\beta}^B$ (Sec. IV B). A gap opens outside the radius marked by green dots (Sec. III B).

Δm_\star are close to the LISA detection uncertainty of the EMRI mass, δm_\star [Eq. (17)] suggesting that the disk gravity and accretion may lead to detectable effects for LISA observations.

Note that the above mentioned simple formulas describing accretion disks are non-relativistic and neglect modifications related to the inner boundary condition of the accretion disk. If assuming zero torque at the inner boundary of the disk, r_0 , this introduces additional factors of $1 - (r_0/r)^{1/2}$ for isothermal disks [31], making the surface density profile no longer a simple power of r . General relativistic corrections introduce additional similar factors near the innermost stable circular orbit (ISCO), light-ring, and horizon [101, 102]. Among these, the ISCO radius is the outermost one, at $1 \leq \bar{r}_\star \leq 9$ in the equatorial plane for spinning BHs. If the shear stress generated by the CO heats the disk, then this may further affect the scale height and the density profile. Non-axisymmetric inflow across the CO orbit, and the inward migration of the CO leads to a more complicated time-dependent density profile [47, 49, 103–106]. We neglect these additional factors for simple order-of-magnitude estimates and extrapolate the disk down to $\bar{r} = 3$ in many of our Figures (which is close to the ISCO for a spinning BH with $a/M \sim 0.9$).

B. Gap opening

Up to this point, we neglected the effects of the CO. If the CO is sufficiently massive so that its gravitational torque moves gas away faster than viscosity can replenish

it, then an annular gap opens in the disk around the CO. The gap width can be obtained from the balance between these two competing effects and it is given by⁹

$$\bar{r}'_\Delta = \left(\frac{f_g}{3\pi} \frac{r_*^2 \Omega}{\nu} q^2 \right)^{1/3} \bar{r}_*, \quad (39)$$

where $\bar{r}_* = r_*/M_\bullet$ is the dimensionless orbital radius of the CO, $q = m_\star/M_\bullet$ is the mass-ratio, and f_g is a geometrical factor for which $3\pi/f_g \approx 40 - 50$ according to numerical simulations [107–109]. Typically, the gap width is much larger than the horizon radius of the CO.

Gap opening requires that the equilibrium width \bar{r}'_Δ be larger than (i) the torque cutoff scale around the CO, and (ii) the scale on which the tidal field of the CO dominates over the SMBH [107, 108, 110, 111]. The CO's tidal torque is shifted out of resonance by the mid-plane radial pressure gradient and saturates interior to the torque cutoff scale, r'_{cutoff} . This is roughly equal to the disk scale height [see Eq. (34)], $r'_{\text{cutoff}} \sim H$ [112]. The tidal field of the CO dominates inside the Hill radius or Roche lobe, r'_H ,

$$r'_H = (q/3)^{1/3} \bar{r}_* = 0.32 m_{\star 1}^{1/3} M_{\bullet 5}^{-1/3} \bar{r}_{\star 10}. \quad (40)$$

Gas entering within r'_H gets either accreted by the CO or it may flow around the CO toward the SMBH.

Thus, gap opening requires¹⁰

$$H \lesssim r'_\Delta \text{ and } r'_H \lesssim r'_\Delta. \quad (41)$$

Combining Eqs. (39–41), we get that a gap opens if the mass-ratio satisfies

$$\begin{aligned} q &> \max \left\{ \sqrt{\frac{3\pi}{f_g} \frac{\nu}{r^2 \Omega}} \left(\frac{H}{r_*} \right)^{3/2}, \frac{3\pi}{f_g} \frac{\nu}{r_*^2 \Omega^2} \right\} \\ &= \max \left\{ \sqrt{\frac{3\pi}{f_g} \alpha \beta^b} \left(\frac{H}{r_*} \right)^{5/2}, \frac{3\pi}{f_g} \alpha \beta^b \left(\frac{H}{r_*} \right)^2 \right\}, \end{aligned} \quad (42)$$

where in the last line we have utilized Eq. (30) for ν , and the terms in the brackets correspond respectively to $H \leq r'_\Delta$, and $r'_H \leq r'_\Delta$. Eq. (44) is general for both α and β -disks. For α -disks $b = 0$, but for β -disks $b = 1$ and the RHS depends implicitly on q and r through β . Substituting H from Eq. (34), and β from Eq. (32) and solving for q gives the mass-ratios that lead to gap

⁹ Here, and throughout the paper, primed distances correspond to radial distances measured from the CO, i.e. $r' = |r - r_*|$.

¹⁰ In the planetary context, the gap opening condition is sometimes written as $H \lesssim r'_H \lesssim r'_\Delta$ where $H \lesssim r'_H$ guarantees that pressure effects are less important than the gravity of the CO and nonlinearities become significant. However, the validity and interpretation of this condition is disputed [113], and we shall not require it here over the two criteria in Eq. (41).

opening

$$q_{\text{gap},\alpha} > \max \left\{ 0.018 \alpha_1^{1/2} \frac{\dot{m}_{\bullet 1}^{5/2}}{\bar{r}_{\star 10}^{5/2}}, 0.092 \alpha_1 \frac{\dot{m}_{\bullet 1}^2}{\bar{r}_{\star 10}^2} \right\}, \quad (43)$$

$$\begin{aligned} q_{\text{gap},\beta} &> \max \left\{ 3.6 \times 10^{-4} \alpha_1^{2/5} \dot{m}_{\bullet 1}^{17/10} M_{\bullet 5}^{-1/10} \bar{r}_{\star 10}^{-29/20}, \right. \\ &\quad \left. 3.9 \times 10^{-5} \alpha_1^{4/5} \dot{m}_{\bullet 1}^{2/5} M_{\bullet 5}^{-1/5} \bar{r}_{\star 10}^{1/10} \right\}, \end{aligned} \quad (44)$$

for α and β -disks, respectively, and we assumed $f_g = 0.23$.

Equations (43–44) can be used to find the CO orbital radius \bar{r}_\star at which a gap opens. For α -disks both terms decrease quickly with radius, thus the gap may eventually close if the CO orbital radius \bar{r}_\star is sufficiently small. However, for β -disks, the second term depends very mildly on radius. Hence, this term for β -disks is best viewed as a radius independent necessary condition for the CO mass for gap formation. The CO radius where a gap opens, satisfies

$$\bar{r}_{\star \text{gap},\alpha} \geq \max \left\{ \frac{79 \alpha_1^{1/5} \dot{m}_{\bullet 1} M_{\bullet 5}^{2/5} m_{\star 1}^{-2/5}}{300 \alpha_1^{1/2} \dot{m}_{\bullet 1} M_{\bullet 5}^{1/2} m_{\star 1}^{-1/2}} \right\}, \quad (45)$$

$$\bar{r}_{\star \text{gap},\beta} \geq 24 \alpha_1^{8/29} \dot{m}_{\bullet 1}^{34/29} M_{\bullet 5}^{18/29} m_{\star 1}^{-20/29} \quad \text{and} \quad (46)$$

$$m_{\star \text{gap},\beta} \gtrsim 3.9 M_\odot \alpha_1^{4/5} \dot{m}_{\bullet 1}^{2/5} M_{\bullet 5}^{4/5}. \quad (47)$$

Therefore, EMRIs in radiation-pressure dominated α -disks in the LISA frequency band ($\bar{r}_\star \lesssim 50$) typically do not open gaps unless $\alpha \lesssim 10^{-3}$. However, a gap typically opens around the CO in a radiation-pressure dominated β -disk, provided the CO mass exceeds a value given by Eq. (47) and it is captured by the accretion disk at a large radius $\bar{r}_\star > 100$. As the CO travels inwards, however, it eventually crosses the radius [given by Eq. (46)] where the gap starts to refill for β -disks too.

If the CO gets first captured in the accretion disk around the SMBH at some large radius $\bar{r}_\star \gg 100$, a gap is expected to be cleared quickly, and the gas interior to the orbit slowly drains down the SMBH on the viscous timescale. Depending on disk parameters and less understood non-axisymmetric inflows [103], the inner disk may be completely or partially cleared by the time the CO reaches the LISA frequency band at separation $\bar{r}_\star \lesssim 50$. If there is still residual gas interior to r_\star , the EMRI may eventually catch up with the inner disk, shepherding it into the SMBH and causing an EM brightening of the AGN [49]. We estimate the radius at which this first happens in Eq. (48) below. Eventually, close to the merger, the gap would refill interior to the radii given by Eqs. (45–46), reigniting the AGN activity.

The fact that in AGN disks, gaps open around EMRIs for large r_\star but then eventually close for smaller separations may seem surprising, because it has the opposite behavior in protoplanetary disks. The reason for the difference is the large radiation pressure in AGN disks, which makes H to be a constant, so that H/r_\star decreases

outwards in Eq. (42). In contrast, H/r_\star is nearly constant, slowly increasing outwards for gas pressure dominated or self-gravitating disks [99, 100]. The other unusual feature in Eq. (42) is the β^b factor, where we recall $\beta = p_{\text{gas}}/(p_{\text{gas}} + p_{\text{rad}})$. This factor approaches 1 and becomes unimportant in the gas pressure dominated regime for β -disks where $b = 1$, while $b = 0$ makes it identically 1 for α -disks. However, this factor makes a big difference in the radiation-pressure dominated regime for β -disks, where $\beta \ll 1$, see Eq. (32).¹¹

We note that the above conditions for gap opening, based on Eq. (41) are probably necessary but perhaps insufficient in realistic disks. While these conditions have been well tested for protoplanetary disks using simulations [108, 109], we are not aware of any studies discussing their applicability in 3D radiation-pressure dominated, turbulent MHD flows for the typical EMRI and accretion disk parameters in AGNs. MHD simulations of turbulent protostellar disks show that in some cases an annular gap may form with an “anti-gap” interior to that region where the gas density is increased compared to the unperturbed case [114].

1. Gap decoupling

As explained above, a gap is expected to form for β -disks in the LISA band for a wide range of parameters. The outer edge of the gap at $\lambda \bar{r}$ can initially follow the secondary as long as the GW inspiral rate is smaller than the viscous gas inflow rate. As the binary separation shrinks, the GW inspiral velocity eventually overtakes the viscous inflow rate, $v_{\star r}(\bar{r}_\star) \geq v_{\text{gas},r}(\lambda \bar{r}_\star)$ and the gas outside the gap cannot keep up with the CO: the outer disk decouples [44]. Coincidentally, the CO can catch up with the disk interior to the gap, if present, causing an EM flare [49]. The evolution of the gap and binary decouple at $\bar{r}_\star \leq \bar{r}_d$, which using Eqs. (8) and (37), is given by

$$\bar{r}_d = \begin{cases} 1.4 \times 10^{-5} \alpha_1^{-2} \dot{m}_{\bullet 1}^{-4} M_{\bullet 5}^{-2} m_{\star 1}^2 \lambda^5 & \text{for } \alpha\text{-disks,} \\ 15 m_{\star 1}^{5/13} \alpha_1^{-4/13} \dot{m}_{\bullet 1}^{-2/13} M_{\bullet 5}^{-4/13} m_{\star 1}^{5/13} \lambda^{2/13} & \text{for } \beta\text{-disks,} \end{cases} \quad (48)$$

where in the following we adopt $\lambda = 1.7$ [111].

The criterion given by Eq. (48) is not satisfied anywhere where a gap has been opened for our nominal set of parameters in either α or β -disks, see Eqs. (45–46). However, the gap can decouple in β -disks for $m_\star \gtrsim 15 M_\odot$ or $\alpha \lesssim 0.05$ [see Fig. 4 below].

¹¹ The β^b factors were incorrectly missing from the gap opening criteria in Ref. [99] for β -disks.

2. Density enhancement outside the gap

As inflowing gas is repelled by the secondary at r_* , gas accumulates outside the gap, and the surface density is modified relative to its original value without the perturber $\Sigma(\bar{r})$ [Eq. (33)] as

$$\Sigma_{\text{gap}}(\bar{r}) = \Sigma(\bar{r}) \times \begin{cases} 1 & \text{if } \bar{r} > \bar{r}_n \\ [m_*/m_d(r_*)]^k & \text{if } \bar{r}_n > \bar{r} > \bar{r}_g \\ 0 & \text{if } \bar{r} < \bar{r}_g \end{cases} \quad (49)$$

where $\bar{r}_g = \lambda \bar{r}_*$ is the outer boundary of the gap¹², and $k = 3/8$ for β -disks¹³ [115], while r_n is the radius at which the density enhancement disappears. In practice r_n is time dependent; it moves outward with velocity of order $|v_{\text{gas},r}|$ [115]. By the time the CO enters the LISA band $r_n \gg 100$.

In Sec. IV through VII we discuss various effects the disk has on EMRIs, and show that the opening of a gap has a serious impact. Depending on whether a gap is opened or not, the CO is subject to Type-II or Type-I migration, respectively. Moreover, if a gap is opened, then the mass density near the secondary is significantly reduced, accretion and hydrodynamic drag effects are quenched. In that case, only the gravitational effects play a role (i.e. axisymmetric disk gravity and Type-II migration).

C. Twists, warps, and disk alignment

In general, MBHs are expected to have a non-negligible spin and dominate the angular momentum of the EMRI and the disk within $\bar{r} \lesssim 10^3$. In the absence of an accretion disk, radiation-reaction tends to circularize the EMRI. Due to GW emission, the orbital angular momentum evolves slowly toward anti-alignment with the MBH spin, although the total perturbation of the orbital inclination is very small [39, 116]. If the CO is on a misaligned orbit, collisions with the disk will cause it to align or counteralign with the disk [14, 34, 38]. In the absence of a CO, if the disk is initially misaligned with the MBH spin axis, Lense-Thirring precession will cause the disk to warp and twist, and viscous dissipation and radiative cooling leads to an aligned or anti-aligned configuration with the MBHs spin (Bardeen–Petterson effect, [117–119]). Similarly, a CO can cause warps and twists in the disk if on an inclined orbit leading to alignment (or

anti-alignment) of the disk plane with the EMRI [104]. Finally, the accretion disk may be warped by the star cluster surrounding the MBH in the outskirts of the disk [120], by an intermediate mass BH [121], or by its own self gravity [122]. Henceforth, we neglect such complications, and consider the MBH, EMRI and disk angular momenta to be aligned or anti-aligned in the relative radial range of LISA observations for simplicity.

IV. MASS INCREASE VIA GAS ACCRETION

Next, we concentrate on the mass increase effect due to accretion. Our goal is to make order of magnitude estimates and compare them to the detectability measures described in Sec. II B.

A. Primary Mass Increase

The accretion disk feeds matter to the SMBH, but such process is bounded by the Eddington limit. This limit corresponds to the balance between radiation pressure and the gravitational force in spherical symmetry¹⁴. The corresponding luminosity due to accretion is

$$L^{\text{Edd}} = \frac{4\pi Gc}{\kappa} M_\bullet, \quad (50)$$

where M_\bullet is the SMBH's mass, which is here the accreting object, and κ is the opacity (see discussion below Eq. (29)).

If a fraction ϵ of the rest mass energy is converted into radiation, then the corresponding accretion rate is

$$\frac{\dot{M}_\bullet^{\text{Edd}}}{M_\bullet} = \frac{L^{\text{Edd}}}{\epsilon M_\bullet c^2} = 2.536 \times 10^{-8} \epsilon_1^{-1} \text{ yr}^{-1}, \quad (51)$$

where $\epsilon_{0.1} = \epsilon/0.1$ is the normalized efficiency. Notice that the right-hand side of this equation is mass-independent. If the SMBH is accreting at a constant rate $\dot{m}_\bullet = \dot{M}_\bullet / \dot{M}_\bullet^{\text{Edd}}$, then

$$M_\bullet(t) \approx M_{\bullet,0} + \dot{M}_\bullet^{\text{Edd}} t = M_{\bullet,0} \left(1 + \frac{\dot{m}_\bullet}{\epsilon_1} \frac{L^{\text{Edd}}}{c^2} t \right), \quad (52)$$

where $M_{\bullet,0}$ is the initial SMBH mass. In the analysis of Sec. III we dropped most factors of ϵ_1^{-1} , but as is clear from here, every factor of \dot{m}_\bullet is accompanied by a factor of ϵ_1^{-1} .

Is such a change in the mass observable via EMRI GWs? Equation (51) tells us that, during a 1 yr observation, the SMBH's mass changes by $\Delta M_\bullet / M_\bullet = 2.2 \times 10^{-9} \dot{m}_\bullet / \epsilon_1$, which is clearly below the LISA mass measurement accuracy of Eq. (17). Another way to see this

¹² We assume that the inflow across the gap interior to the CO is significantly reduced by the CO. This is a conservative estimate since, non-axisymmetric inflow is expected to occur across the inner edge of the annulus at a reduced rate [103].

¹³ In the radiation-pressure dominated regime, k has not been determined for α -disks. We conservatively adopt $k = 0$ in this case.

¹⁴ This limit may sometimes be violated as shown in Sec. IV B below.

is to compute the phase shift (Eq. (18)) for Eddington-limited accretion, which yields $\delta\phi_{\text{GW}}^{\text{Edd}} \sim \phi_{\text{GW}}^{\text{tot}} T_{\text{obs}} / \mathcal{T}_{\text{Edd}} \approx 10^{-3} \dot{m}_{\bullet 1} M_{\bullet 5}^{-1/4} m_{\star 1}^{3/8} T_{\text{yr}}^{13/8}$, much smaller than the phase measurement accuracy. We conclude then that the change in the SMBH's mass via Eddington-limited accretion has a negligible effect on the GW signal, irrespective of the type of disk modeled. The accretion has to be very super-Eddington or the radiation efficiency very small ($\dot{m}_{\bullet 1}/\epsilon_1 \rightarrow 10^3$) for it to have any impact on the GW signal for typical EMRIs at 1 Gpc.

B. Secondary Mass Increase

The CO itself increases in mass too, as it feeds from the ambient gas in the accretion disk. We consider the case when the CO orbital inclination is aligned with the disk. The thickness of the accretion disk [Eq. (34)] is much larger than the horizon diameter by a factor of $H/m_{\star} \sim 1.5 \dot{m}_{\bullet 1} M_{\bullet} / m_{\star} \sim 10^4$, and thus, it completely surrounds the CO.

In such circumstances, accretion can be analyzed within the framework of Bondi-Hoyle-Lyttleton (BHL) [29–31]. The characteristic radius of accretion can be calculated as the radius at which the thermal energy of particles is less than the gravitational potential energy¹⁵

$$r'_{\text{B}} = \frac{2m_{\star}}{v_{\text{rel}}^2 + c_s^2} \approx \frac{2m_{\star}}{M_{\bullet}} \frac{r^3}{H^2} = 8.9 \times 10^3 M_{\odot} m_{\star 1} \dot{m}_{\bullet 1}^{-2} \bar{r}_{10}^3. \quad (53)$$

The second and third equality correspond to corotating quasi-circular COs, neglecting v_{rel} and using Eqs. (38) and (34).

Assuming isotropic accretion and an adiabatic equation of state, the Euler and continuity equations can be integrated to give

$$\begin{aligned} \frac{\dot{m}_{\star}^{\text{B}}}{m_{\star}} &= 4\pi\rho \frac{m_{\star}}{(v_{\text{rel}}^2 + c_s^2)^{3/2}} \quad (54) \\ &\approx \begin{cases} 1.5 \times 10^{-7} \text{ yr}^{-1} \alpha_1^{-1} \dot{m}_{\bullet 1}^{-5} M_{\bullet 5}^{-1} m_{\star 1} \bar{r}_{10}^6 \\ \text{for } \alpha\text{-disks, corotating, circular CO,} \\ 3.5 \times 10^{-4} \text{ yr}^{-1} \alpha_1^{-4/5} \dot{m}_{\bullet 1}^{-17/5} M_{\bullet 5}^{-4/5} m_{\star 1} \bar{r}_{10}^{39/10} \\ \text{for } \beta\text{-disks, corotating, circular CO.} \end{cases} \end{aligned}$$

where ρ is the ambient density, c_s is the sound speed, and v_{rel} is the relative velocity of the gas with respect to the medium, Eqs. (8) and (36–38). The numerical values shown in the second line are only representative, they assume $v_{\text{rel}} = |\mathbf{v}_{\text{gas}} - \mathbf{v}_{\star}| \ll c_s$. This is approximately satisfied near the SMBH, but in the numerical calculations we substitute the estimated value of v_{rel} (see

Eq. (58) below). Figure 3 shows the corresponding mass accretion rate per year for α and β -disks, including the quenching processes discussed next.

C. Quenching of BHL Accretion

Accretion can be “quenched” or suppressed by several different astrophysical processes. In this subsection, we summarize all such quenching effects that severely modify the accretion rates quoted in Eq. (54).

1. Quenching by wind and tidal effects

When v_{rel} is not neglected, the estimates of Eq. (54) are reduced. The relative velocity between the CO and the gas contains contributions from the relative bulk motion of the gas, differential rotation of the disk, and turbulence.

The effect of differential rotation can be estimated as follows. Since the gas velocity is different at the edge of the accretion range relative to the bulk velocity at r at orbital radii $r \pm \delta r'$, then

$$\delta v_{\text{dr}} = |\delta r'^i \nabla_i v_{\text{gas}}^j| \approx \left| \partial_r v_{\phi} + \Gamma_{\phi r}^{\phi} v_{\phi} \right| r_{\text{H}} = \frac{3}{2} \bar{r}_{\text{H}} \bar{r}^{-3/2}, \quad (55)$$

where in the second equality we have set $(\delta r'^r, \delta r'^\phi) = (r'_{\text{H}}, 0)$, and in the third used $v_{\phi} = \sqrt{M_{\bullet}/r}$ and $\Gamma_{\phi r}^{\phi} = -1/r$ for the Christoffel symbol in flat space. Substituting in for the Hill radius [Eq. (40)], this becomes

$$\delta v_{\text{dr}} = \frac{3}{2} \frac{r'_{\text{H}}}{H} c_s = 0.015 \left(\frac{m_{\star 1}}{M_{\bullet 5}} \right)^{1/3} \bar{r}_{10}^{1/2}. \quad (56)$$

We estimate the radial wind using $\delta v_r = |v_{\text{gas},r} - v_{\star,r}|$, where $v_{\text{gas},r}$ and $v_{\star,r}$ can be found in Eqs. (8) and (37). The relative velocity induced by an azimuthal wind δv_{ϕ} is

$$\delta v_{\phi} = \frac{3 - \gamma}{2} \frac{H}{r} c_s = \begin{cases} 0.0053 \dot{m}_{\bullet 1}^2 \bar{r}_{10}^{-5/2} & \text{for } \alpha\text{-disks} \\ 0.013 \dot{m}_{\bullet 1}^2 \bar{r}_{10}^{-5/2} & \text{for } \beta\text{-disks} \end{cases}, \quad (57)$$

which we derive in Sec. V below.

With all of this in mind, the relative velocity is then

$$v_{\text{rel}}^2 = (\delta v_{\phi} + \delta v_{\text{dr}})^2 + \delta v_r^2. \quad (58)$$

Figure 2 shows that δv_{dr} dominates the relative gas velocity relative to the bulk azimuthal and radial wind velocities. Indeed, $\delta v_{\text{dr}} > c_s$ when the CO's mass is larger than $m_{\star} \gtrsim 300 M_{\bullet 5} \dot{m}_{\bullet 1}^3 \bar{r}_{10}^{-3}$ or if $\bar{r} > \bar{r}_{\text{dr}} \equiv 31 \dot{m}_{\bullet 1} M_{\bullet 5}^{1/3} m_{\star 1}^{-1/3}$. In that case, one might expect large deviations in Eq. (54). As we show in Sec. IV C 3, however, this quenching mechanism is typically superseded by limited gas supply. Nevertheless, we include v_{rel} in our calculations below.

¹⁵ We use r' to distinguish orbital distances measured from the CO.

We denote the CO orbital radius by r unless it leads to confusion, otherwise r_{\star} . Over-bar denotes units of M_{\bullet} .

The accretion is very anisotropic due to differential rotation and turbulence in the accretion disk. The accretion rate in such an advection dominated accretion flow may be significantly less than the BHL rate [123, 124]. We consider our simple estimates to be accurate only to the order of magnitude.

2. Quenching by thin disk geometry

Spherical BHL accretion is valid in the region where the Bondi radius is less than (i) the scale height of the disk H [Eq. (34)], and (ii) the Hill's radius or Roche lobe where tidal effects from the SMBH are negligible [Eq. (40)]. These constraints are satisfied interior to

$$\bar{r}_{\text{thin}} = 19 \dot{m}_{\bullet 1} M_{\bullet 5}^{1/3} m_{\star 1}^{-1/3}, \quad (59)$$

$$\bar{r}_{\text{tidal}} = 26 \dot{m}_{\bullet 1} M_{\bullet 5}^{1/3} m_{\star 1}^{-1/3}. \quad (60)$$

Thus, the thin disk requirement is always more restrictive for radiation-pressure dominated disks.

Beyond orbital radius \bar{r}_{thin} [Eq. (59)], the accretion cross section is reduced from $4\pi r_B'^2$ to $4\pi r_B' H$, because of cylindrical symmetry. Consequently, the accretion rate is modified as

$$\dot{m}_{\star}^{\prime B} \approx \min \left[1, \frac{H}{r_B'} \right] \dot{m}_{\star}^B. \quad (61)$$

3. Quenching by limited gas supply

The BHL accretion rate might also be limited by the amount of gas supply near the CO. First, note that the radial inspiral velocity $v_{\star r}$ is typically much slower than the radial inflow velocity of the gas $v_{\alpha r}$ and $v_{\beta r}$ for α and β -disks (Fig. 2). This implies that there is a constant gas flux across the CO orbit from the outer regions. However, if the Bondi rate in Eq. (54) was greater than the radial gas flux toward M_{\bullet} , then the accretion onto m_{\star} would be limited by the rate at which gas flows in from the outer regions. The mass flux across the CO's orbit is

$$\dot{M}_{\text{flux},\star} = 2\pi r \Sigma |v_{\text{gas},r} - v_{\star r}| = \dot{M}_{\bullet} \left| 1 - \frac{v_{\star r}}{v_{\text{gas},r}} \right| \quad (62)$$

where $v_{\star r}$ and $v_{\text{gas},r}$ are given by Eqs. (8) and (37). Thus, the accretion rate onto the CO becomes

$$\dot{m}_{\star}'' = \min \left[\dot{M}_{\text{flux},\star}, \dot{m}_{\star}^{\prime B} \right]. \quad (63)$$

At large separations, $|v_{\star r}| \ll |v_{\text{gas},r}|$, the CO accretes inflowing gas from the outside and the accretion rate \dot{m}_{\star} becomes independent of radius (as long as a gap is not opened, see Sec. III B). At very small separations, given by Eq. (48), $|v_{\star r}| > |v_{\text{gas},r}|$, the CO sweeps up the disk interior to its orbit, and the accretion rate becomes sensitive to the assumptions on the available gas supply interior to the orbit.

Is Eq. (63) an important constraint for EMRI systems observable by LISA? If the mass-ratio is extreme $\eta \lesssim 10^{-4}$, then $|v_{\star r}| \ll |v_{\text{gas},r}|$ (Fig. 2), so Eq. (63) imposes a constraint if and only if $\dot{m}_{\star}^B \leq \dot{M}_{\bullet}$ is violated for the radial separations covered by the CO during the observation. This is the case outside $\bar{r} \geq \bar{r}_q$, where

$$\bar{r}_q = \begin{cases} 24 \alpha_1^{1/6} \dot{m}_{\bullet 1} M_{\bullet 5}^{1/3} m_{\star 1}^{-1/3} & \text{for } \alpha\text{-disks,} \\ 5.1 \alpha_1^{8/39} \dot{m}_{\bullet 1}^{44/39} M_{\bullet 5}^{6/13} m_{\star 1}^{-20/39} & \text{for } \beta\text{-disks.} \end{cases} \quad (64)$$

Figure 2 shows that the accretion rate of the CO saturates at \dot{M}_{\bullet} at large \bar{r} . BHL accretion is supply limited for at least part of the observation for the particular EMRI systems we consider in Sec. IX A below.

4. Quenching by radiation pressure

Since the BHL accretion rate is typically super-Eddington for a mass m_{\star} , does radiation pressure quench such large rates? One has to be careful about this point since the derivation of the BHL accretion rate restricts to adiabatic flows, neglecting the effects of radiation pressure, heat transport, and cooling. Super-Eddington mass accretion onto the CO is possible if the radiation is transported inward with the inflow faster than how it can diffuse out [125–127]. We compare the diffusion time with the infall time below.

The infall time of the fluid element from the Bondi radius to a distance r' from the CO is approximately

$$t_{\text{in}} \approx r_B' \frac{1 - \tilde{r}'}{\sqrt{v_{\text{rel}}^2 + c_s^2}}, \quad (65)$$

where $\tilde{r}' = r'/r_B'$ is the dimensionless radial distance from the CO, and the denominator is the RMS gas velocity.

The diffusion time from a distance r' from the CO to r_B' is

$$t_{\text{diff}}(r') = \frac{1}{2} \int_{r'}^{r_B'} \kappa \rho_{\star}(\xi) \xi d\xi, \quad (66)$$

where we recall that κ is the gas opacity (see discussion after Eq. (29)). To avoid confusion, we label the local gas density in the close vicinity of the CO as $\rho_{\star}(r')$, which at the Bondi radius is equal to the mean disk density near the location of the CO, $\rho_{\star}(r_B') \equiv \rho(r_{\star})$ in Eq. (36). For BHL accretion, the density increases toward the CO as $\rho_{\star}(r') = \rho_{\star}(r_B') \tilde{r}'^{-3/2}$ [29–31]. Thus, Eq. (66) simplifies to

$$\begin{aligned} t_{\text{diff}} &= \kappa \rho(r_{\star}) r_B'^2 \left(1 - \tilde{r}'^{1/2} \right) \\ &= \frac{\kappa}{\pi} \frac{\dot{m}_{\star}^B}{\sqrt{v_{\text{rel}}^2 + c_s^2}} \left(1 - \tilde{r}'^{1/2} \right), \end{aligned} \quad (67)$$

where in the second line we have used Eq. (54) to relate t_{diff} to the BHL accretion rate. Comparing Eqs. (65)

and (67), we find that the diffusion time is larger than the infall time, precisely if $\dot{m}_\star^B \geq \dot{m}_\star^{\text{crit}}$ where

$$\begin{aligned} \frac{\dot{m}_\star^{\text{crit}}}{m_\star} &\equiv \frac{\pi}{\kappa} \frac{r'_B}{m_\star} \left(1 + \tilde{r}'^{1/2}\right) = \frac{2\pi}{\kappa} \frac{1 + \tilde{r}'^{1/2}}{v_{\text{rel}}^2 + c_s^2} \quad (68) \\ &\approx 5.6 \times 10^{-7} \text{ yr}^{-1} \dot{m}_{\bullet 1}^{-2} \tilde{r}_{10}^3 \left(1 + \tilde{r}'^{1/2}\right). \end{aligned}$$

The second line corresponds to $v_{\text{rel}} \ll c_s$, but in the numerical calculations we substitute v_{rel} from Eq. (58).

Interestingly, radiation pressure does not have any impact if the BHL accretion rate exceeds the limit, $\dot{m}_\star^{\text{crit}}$. For the nominal parameter values for a β -disk, Eqs. (54) and (68) show that $\dot{m}_\star^B \geq \dot{m}_\star^{\text{crit}}$ is satisfied for all $0 \leq \tilde{r}' \leq 1$. Therefore, we are reassured that radiation is trapped and advected inward in this case. However, α -disks are much less dense, and this condition is violated interior to $20\alpha_1^{1/3}\dot{m}_{\bullet 1}M_{\bullet 5}^{1/3}m_{\star 1}^{-1/3}$.

More generally, BHL accretion may be quenched by the various other effects discussed above, modifying r'_B and decreasing the gas density, and thereby the diffusion and infall times. In this case, radiation pressure may further suppress the accretion rate onto the CO if $\dot{m}_\star \leq \dot{m}_\star^{\text{crit}}$. This criterion can be fulfilled by both α and β -disks. The accretion rate then becomes

$$\dot{m}_\star''' = \begin{cases} \dot{m}_\star'' \text{ if } \dot{m}_\star'' \geq \dot{m}_\star^{\text{crit}}, \\ \dot{m}_\star^{\text{Edd}} \text{ otherwise.} \end{cases} \quad (69)$$

where \dot{m}_\star'' is given by Eq. (61) and we model the radiation-pressure quenched accretion as Eddington limited, replacing M_\bullet with m_\star in Eq. (51). We here choose $\tilde{r}' = 1$, as this gives the most conservative (smallest) estimate for \dot{m}_\star''' .

5. Quenching by gap formation

If the tidal torques of the CO are sufficiently strong to dominate over the viscous inflow, an annular gap forms around the CO, where the gas density is significantly reduced (see Sec. III B). Gap formation requires m_\star and r_\star to be sufficiently large, [Eqs. (45–47)]. These conditions can be satisfied for β -disks during the final year of the inspiral, but not for typical α -disks. If a gap forms, the accretion onto the CO ceases.

For large CO masses $m_\star \gtrsim 15 M_\odot$ or $\alpha \lesssim 0.05$, the inspiral rate becomes faster than the viscous inflow rate of gas outside the annular gap if $r_{\text{gap}} < r_\star < r_d$ (see Eq. 48). In this case, the CO may “catch up” with the gas interior to the orbit [49]. The inner disk may be filled by non-axisymmetric or three dimensional overflow [103]. In fact, in turbulent MHD disks, the region interior to the annular gap may have an over-density (“anti-gap”) relative to the case without an EMRI [114]. In this case, \dot{m}_\star may be restarted interior to r_d , and may exceed the BHL rate of the original unperturbed surface density of the disk [Eq (54)]. However, it is also possible that the inner disk drains away before r_d is reached, implying no

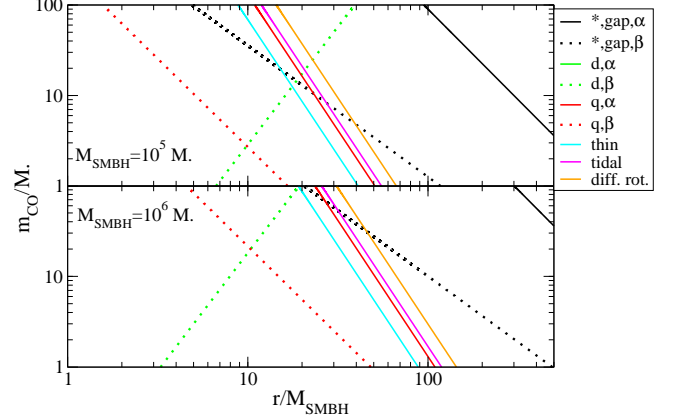


FIG. 4. Critical CO mass as a function of CO orbital radius for various mechanisms to quench BHL accretion onto the CO. The accretion rate is reduced for larger m_\star or larger r_\star . Top and bottom panels correspond to $M_\bullet = 10^5$ and $10^6 M_\odot$, respectively. Gap-decoupling occurs interior to the green curves.

accretion. We conservatively assume no accretion onto the CO if a gap is present,

$$\dot{m}_\star = \begin{cases} \dot{m}_\star''' \text{ if } r \leq r_{\text{gap}}, \\ 0 \text{ otherwise.} \end{cases} \quad (70)$$

6. Summary of quenching processes

The mass increase of the CO is very sensitive to the complicated details of accretion disk astrophysics. Most of these processes act to decrease the accretion rate from \dot{m}_\star^B . We summarize the EMRI parameters where various quenching mechanisms are in play in Figure 4. This figure depicts the minimum CO mass m_\star and orbital radii where particular processes become significant to quench the BHL accretion rate onto the CO for $\alpha_1 = \dot{m}_{\bullet 1} = 1$ for different $M_\bullet = 10^5 M_\odot$ (top panel) and $10^6 M_\odot$ (bottom panel). For these parameters, accretion is first completely quenched by gap formation for β -disks, but gaps do not form for α -disks for EMRIs in the LISA range. Then the gap refills, and accretion is limited by the amount of inflowing gas, radiation pressure, differential rotation, and the thin disk geometry. Closer to the SMBH, these processes become less and less significant and the accretion rate increases to the BHL rate \dot{m}_\star^B . This decreases inward with the decrease of gas density and the increase in the sound speed. The corresponding CO mass increase is shown in Figure 2 above.

D. Implications of BHL Accretion

Let us now describe the implications of BHL accretion on EMRI formation and the GW phase. The former is relevant to understand whether EMRIs can remain ex-

treme mass-ratio systems as they inspiral in the accretion disk toward the LISA band, or if they grow in mass to form an intermediate mass BH. Then, we estimate the corresponding perturbation to the GW phase and discuss its detectability with LISA.

Equations (54), (61), (63), (69), and (70) show that the CO mass growth rate is sensitive to the location of the CO, i.e. \dot{m}_\star is not a constant. The mass at radius \bar{r} can be estimated as

$$m_\star = m_{\star,0} + \int_{t_0}^t \dot{m}_\star dt = m_{\star,0} + \int_{\bar{r}_0}^{\bar{r}} \frac{\dot{m}_\star}{\dot{r}} d\bar{r}, \quad (71)$$

where $m_{\star,0}$ is the initial CO mass, and \dot{m}_\star is the accretion rate and \dot{r} is the inspiral rate (8).

1. EMRI formation scenarios

Does the CO mass grow significantly in the disk prior to the LISA observation? If the CO migrated through the disk from very large radii, $m_\star \gg 10M_\bullet$ could be expected by the time the CO reaches detectable separations for LISA observations [16, 17]. At large orbital radii the accretion rate is supply limited. Assuming that a gap does not form and the CO consumes the inflowing gas completely and that $|\dot{r}_\star| \ll |v_{\text{gas},r}|$

$$\Delta m_\star \leq \dot{M}_\bullet t_{\text{merger}} \leq 1.2 M_\odot \frac{\dot{m}_{\bullet 1} M_{\bullet 5}^3}{m_{\star 1}} \bar{r}_{200}^4, \quad (72)$$

where $\bar{r}_{200} = \bar{r}_0/200$ and we have substituted the inspiral time to coalescence t_{merger} given by Eq. (13).¹⁶ The merger time is typically less than the GW driven inspiral time due to angular momentum exchange with the disk discussed in Sec. VII [17, 35], so that Eq. (72) is only an upper limit on Δm_\star . Note that in this case, the mass increase is larger than the instantaneous amount of disk mass within a few Hill's radii [Eq. (40)], called the isolation mass, due to the viscous inflow of gas from the outer regions across the orbit. This situation is most relevant for α -disks where a gap does not form easily [see Eq. (45)].

Once the CO mass has grown sufficiently, the tidal torque of the CO eventually opens a radial gap in the disk, halting further growth. This leads to a limit called

the starvation mass¹⁷ [129], which from Eq. (43–44) is

$$\begin{aligned} \Delta m_{\star\alpha} &\leq \max \left\{ 1800 M_\odot \alpha_1^{1/2} \dot{m}_{\bullet 1}^{5/2} M_{\bullet 5} \bar{r}_{10}^{-5/2}, \right. \\ &\quad \left. 9200 M_\odot \alpha_1 \dot{m}_{\bullet 1} M_{\bullet 5} \bar{r}_{10}^{-2} \right\}, \end{aligned} \quad (73)$$

$$\begin{aligned} \Delta m_{\star\beta} &\leq \max \left\{ 36 M_\odot \alpha_1^{2/5} \dot{m}_{\bullet 1}^{17/10} M_{\bullet 5}^{9/10} \bar{r}_{10}^{-29/20}, \right. \\ &\quad \left. 3.9 M_\odot \alpha_1^{4/5} \dot{m}_{\bullet 1}^{2/5} M_{\bullet 5}^{4/5} \bar{r}_{10}^{-1/10} \right\}. \end{aligned} \quad (74)$$

Note that both Eq. (72) and (73) must be satisfied for α -disks, and Eq. (74) for β -disks. In both cases, the CO mass remains small $m_\star \ll 100 M_\odot$ for $M_\bullet = 10^5 M_\odot$. It grows to at most $\sim 76 M_\odot$ until reaching $\bar{r} = 25$ for $M_\bullet \sim 10^6 M_\odot$ in a β -disk, but can grow beyond $100 M_\odot$ for $M_\bullet \gtrsim 10^6 M_\odot$ in an α -disk, if captured in the disk outside $\bar{r} \gtrsim 50$. If so, an initial EMRI would morph into an intermediate mass-ratio inspiral before entering the LISA band. Growth beyond a mass given by Eq. (74) is halted by gap formation [17].

We conclude that EMRIs can remain extreme in mass-ratio on their journey to the LISA band ($\bar{r} \lesssim 50$) for a non-negligible set of disk parameters. Conversely, the mass measurement with LISA could have interesting implications on the structure of the accretion disk. Suppose LISA measures m_\star to be large, consistent with either Eq. (73) or (74). This information alone would suggest that the CO has grown by accretion in an α or β -disk, and suggest the possible presence of a disk, even without a direct GW phase shift measurement. In the opposite case, if LISA measures m_\star to be larger than what is expected from the growth arguments given by Eq. (73–74), then this could point to the common existence of intermediate mass BHs, which is debated at the time of the writing of this manuscript.

2. GW Observations

BHL accretion changes the GW inspiral rate of the EMRI due to the increase in the radiating mass quadrupole. This leads to a GW phase shift relative to a constant m_\star . Is BHL accretion measurable for EMRIs with LISA observations?

For a crude first estimate let us consider the corresponding limits on the mass and timescales of Sec. II B 1. Figure 3 shows the BHL mass accretion rate as a function of radius (red lines). For these masses ($10 M_\odot, 10^5 M_\odot$),

¹⁶ In the opposite extreme $|\dot{r}_\star| \gg v_{\text{gas},r}$, the CO growth is limited by the interior disk mass, which is typically less than $10M_\bullet^2 M_\odot$ within $\bar{r} \sim 10^3$, see Fig. 3.

¹⁷ If a gap opens and the CO is transported inward by Type-II migration together with the flow (see Sec. VII below), then Δm_\star is limited by the local disk mass in a few Hill's radii, i.e. the isolation mass [128]. However, typical CO masses exceed the local disk mass within $\bar{r} \lesssim 10^3$ (see Fig. 3), and the inward migration rate is slower than the gas inflow rate. In this case, gas can build up near the edge of the gap and cause the object to grow to the starvation mass.

$\Delta m_*/m_* \sim 10^{-5}$ to 10^{-4} for α and β -disks. This is comparable to the mass measurement precision of LISA for a source at ~ 1 Gpc, suggesting that the perturbation caused by the CO mass growth may be marginally significant. The timescale argument with $\mathcal{T}_B \sim m_*/\dot{m}_*$ is not directly applicable as \dot{m}_* varies significantly during a one-year LISA measurement.

A more accurate analytical estimate is computed in Appendix A, where we integrate the total perturbation to the GW phase assuming that $\dot{m}_* = Ar^B$, where A and B are constants. The phase shift will be presented in Sec. VIII, Eqs. (115–116) and Table II; it shows that the phase shift accumulates with time initially as $\delta\phi \approx a_1 T^3 + a_2 T^4$, for short observations relative to the inspiral rate, and eventually asymptotes to $a_3 T^{c_5}$, where (a_1, a_2, a_3, c_5) are constant coefficients that depend on the EMRI and the accretion disk parameters.

We find that the quenching by gas supply has a major effect on the GW phase shift. Without quenching, the effect would be of order $\delta\phi_{\text{GW}}^B \sim 7$ and 3000 rads for α and β -disks respectively, and even larger for larger m_* , assuming $T_{\text{obs}} = 1$ yr and $M_{\bullet,5} = m_{\star,1} = \dot{m}_{\bullet} = 1$. However, at most separations, the BHL rate is significantly suppressed by gas supply for β -disks, but the reduced dephasing is still about 13 rad per a year, and larger for larger M_{\bullet} . The phase shift is proportional to the following combination of accretion disk parameters: $\alpha_1^{-1} \dot{m}_{\bullet,1}^{-5}$ and $\alpha_1^{-4/5} \dot{m}_{\bullet,1}^{-17/5}$ for the unquenched BHL rate for α and β -disks, and $\dot{m}_{\bullet,1}$ for the supply limited rate. These combinations may be marginally measurable by LISA observations, given sufficiently strong signals.

V. HYDRODYNAMIC DRAG

Next, we consider the drag induced by a difference between the gas and CO velocities, sometimes called *wind*. This relative velocity is a consequence of a pressure gradient in the disk and results in a force that pushes the CO both azimuthally and radially [25, 26]. As in Sec. IV, the goal is to make order of magnitude estimates on the corresponding GW phase shift and compare them to the detectability measures of Sec. II B.

A. Azimuthal wind

If the orbital velocity of the gas is different from the CO's orbital velocity, the latter will experience an azimuthal headwind or backwind (relative to its unperturbed azimuthal motion). To estimate the orbital velocity of the gas, let us write the radial equation of motion assuming that $M_{\bullet} \gg m_*$, the orbital velocity is much larger than the radial velocity, and that the flow is subsonic:

$$-\frac{v_{\phi}^2}{r} + v_r \nabla_r v_r = -\frac{M_{\bullet}}{r^2} - \nabla_r \Phi_{\star} - \nabla_r \Phi_{\text{disk}} - \frac{\nabla_r p_{\text{tot}}}{\rho}, \quad (75)$$

where v_{ϕ} and v_r are the azimuthal and radial velocities of the gas, p_{tot} is the total pressure of the gas in a comoving frame, and ρ is the gas density. For standard thin disks, $p_{\text{tot}} = \rho c_s^2 = \rho H^2 \Omega^2$, where the scale height H is independent of radius in the radiation-pressure dominated regime [see e.g. Eqs. (34) and (38)]. The orbital average gravitational potential of the CO, Φ_{disk} , acting on the fluid element at radius r is

$$\Phi_{\star} = -\frac{2}{\pi} \frac{m_{\star}}{r + r_{\star}} K\left(\frac{2\sqrt{rr_{\star}}}{r + r_{\star}}\right), \quad (76)$$

where $K(k) = \int_0^{\pi/2} (1 - k^2 \sin^2 \theta)^{-1/2} d\theta$ is the complete elliptic integral of the first kind. The gravitational potential of the disk, Φ_{disk} , will be given in Sec. VI [see e.g. Eq. (95)].

Let us parameterize the radial density profile via $\rho(r) \propto r^{\gamma}$, where the exponent $\gamma = 3/2$ and $\gamma = -3/5$ for α and β -disks respectively [Eq. (33)]. Note that $v_r \nabla_r v_r$ is negligible in Eq. (75) since $v_r \ll c_s$ and $v_r \propto 1/(r\Sigma)$, see Eq. (37), and Fig. 2. Equation (75) then becomes

$$-\frac{v_{\phi}^2}{r} = -\frac{M_{\bullet}}{r^2} - \nabla_r \Phi_{\star} - \nabla_r \Phi_{\text{disk}} + (3 - \gamma) \frac{H^2 \Omega^2}{r}, \quad (77)$$

which one can solve to obtain

$$v_{\phi}^2 = \frac{M_{\bullet}}{r} \left[1 + (\gamma - 3) \frac{H^2}{r^2} + \frac{r}{M_{\bullet}} \nabla_r (\Phi_{\star} + \Phi_{\text{disk}}) \right]. \quad (78)$$

In the following we neglect the effects of the potential due to the secondary, an approximation valid if the gas accretes onto the CO from outside the Hill's sphere, i.e. the $r'_{\text{B}} < r'_{\text{H}}$, see Eqs. (60), as well as the disk gravity.

We then find that a corotating CO always experiences an azimuthal headwind with velocity (i.e. orbital velocity of gas with respect to the CO),

$$\begin{aligned} \delta v_{\phi} &\equiv \Omega_{\text{vac}} r - v_{\phi} \\ &\approx \frac{3 - \gamma}{2} \frac{H^2}{r^2} \sqrt{\frac{M_{\bullet}}{r}} = \frac{3 - \gamma}{2} (1.5 \dot{m}_{\bullet,1})^2 \bar{r}^{-5/2}, \end{aligned} \quad (79)$$

where we have used Eqs. (34) and (78). This equation agrees with Tanaka et. al. [130] or the approximate equation of Levin [17]. This estimate, however, does not hold for transsonic flows, as in this case the CO experiences a backwind, as found by Chakrabarti [26]. Since such flow requires very high accretion rates where the thin disk approximation may not hold, we ignore this possibility here.

An azimuthal headwind leads to additional dissipation of the CO's specific angular momentum, $\dot{\ell}_{\text{wind}} = r \dot{P}/m_{\star}$, where \dot{P} is the rate of change of the linear momentum, so that

$$\dot{\ell}_{\text{wind}} = -\frac{r \dot{m}_{\star} \delta v_{\phi}}{m_{\star}} = -\frac{3 - \gamma}{2} \frac{\dot{m}_{\star} M_{\bullet}}{m_{\star}} (1.5 \dot{m}_{\bullet,1})^2 \bar{r}^{-3/2}, \quad (80)$$

where we have used Eq. (79). Clearly, this is typically a small perturbation relative even to the loss of angular

momentum through GW emission. For unsaturated BHL accretion $\dot{m}_\star = \dot{m}_\star^B$, substituting Eq. (54) yields

$$\frac{\dot{\ell}_{\text{wind}}^B}{\dot{\ell}_{\text{GW}}} \approx \begin{cases} 6.1 \times 10^{-10} \alpha_1^{-1} \dot{m}_\star^{-3} M_{\bullet 5} \bar{r}_{10}^8 & \text{for } \alpha\text{-disks,} \\ 3.4 \times 10^{-6} \alpha_1^{-4/5} \dot{m}_\star^{-7/5} M_{\bullet 5}^{6/5} \bar{r}_{10}^{59/10} & \text{for } \beta\text{-disks.} \end{cases} \quad (81)$$

For supply limited BHL accretion $\dot{m}_\star = \dot{M}_\bullet$, Eq. (62), yields

$$\frac{\dot{\ell}_{\text{wind}}^{\text{sup.Bondi}}}{\dot{\ell}_{\text{GW}}} \approx \left(\begin{array}{l} 1.0 \times 10^{-7} \\ 2.5 \times 10^{-7} \end{array} \right) \times \dot{m}_\star^3 \frac{M_{\bullet 5}^3}{m_{\star 1}^2} \bar{r}_{10}^2, \quad (82)$$

where the top and bottom rows correspond to α and β -disks respectively. The change in the angular momentum dissipation rate leads to a modified inspiral rate that we discuss in Sec. V D.

B. Radial wind

In addition to the azimuthal headwind, the CO also experiences a wind in the radial direction. The corresponding force is

$$\dot{P}_{\text{wind}} = \dot{m}_\star |v_{r\star} - v_{\text{gas},r}| \quad (83)$$

$$\approx \frac{\dot{M}_\bullet m_\star^2}{H c_s^3 r} = 2.5 \times 10^{-22} \dot{m}_\star^{-3} M_{\bullet 5}^{-1} m_{\star 1}^2 \bar{r}_{10}^{7/2}, \quad (84)$$

where we have assumed $|v_{r\star}| \ll |v_{\text{gas},r}|$, see Fig. 2. The radial equation of motion is thus

$$m_\star \Omega^2 r = \frac{m_\star M_\bullet}{r^2} + \dot{P}_{\text{wind}}. \quad (85)$$

The first term on the RHS is the gravitational force, which satisfies $m_\star M_\bullet / r^2 = m_\star \Omega_{\text{vac}}^2 r$, by the definition of Ω_{vac} . Therefore, unlike the azimuthal wind, the radial wind does not dissipate angular momentum, but it modifies the orbital velocity Ω_{vac} relative to Keplerian:

$$\frac{\Omega^2 - \Omega_{\text{vac}}^2}{\Omega_{\text{vac}}^2} = \frac{\dot{P}_{\text{wind}}}{m_\star \Omega_{\text{vac}}^2 r} = 2.5 \times 10^{-16} \frac{m_{\star 1} \bar{r}_{10}^{11/2}}{\dot{m}_\star^3}. \quad (86)$$

The impact of this modification on the GW phase will be discussed in Sec. V D.

C. Dynamical friction

Dynamical friction is generated by the gravitational interaction of a perturber traveling at some relative velocity in an ambient medium [131]. The gravity of the perturber deflects the particles of the medium and generates a density wake trailing the perturber. In turn, the gravitational pull of the density wake acts like friction, decreasing the speed of the perturber. This process is analogous to Landau-damping in plasma physics and is also important in galactic dynamics for objects moving through a population of stars [132, 133].

The standard treatment of dynamical friction in a gaseous medium usually assumes that the medium has a spatially uniform initial velocity distribution relative to the perturber. If the perturber moves on a linear trajectory with a subsonic relative velocity in a gaseous medium, then the density wake in front and behind the perturber approximately cancel, leading to a small drag force [134]. However, dynamical friction is more significant for a supersonic perturber. Dynamical friction has also been investigated for perturbers moving on quasi-circular orbits in an initially static (i.e. non-rotating) medium [135]. In this case the density wake has a spiral structure and the drag force is enhanced. A fully relativistic treatment was presented in Refs. [38, 136].

Equations (37), (38), and (79) and Figure 2 show that the relative wind velocity at corotating orbits is typically non-relativistic and subsonic in standard α and β -disks. The arguments mentioned above then imply that the standard dynamical friction effect is greatly suppressed.¹⁸

The relative gas velocity at different radii outside $r_\star \pm \frac{2}{3}H$, however, is supersonic [see Eq. (55)] and thus, dynamical friction with respect to the gas in this region may be significant. In this case, the velocity of the medium is mostly due to differential rotation of the accretion disk and not the wind generated by the pressure gradient effects of Sec. V A. Differential rotation causes the density waves to wind up and standard dynamical friction formulas are not applicable. This regime has been well studied in planetary dynamics, which leads to the phenomenon called planetary migration. In this paper, we explicitly distinguish between such migration, described separately in Sec. VII below, and standard dynamical friction, which as argued above has a negligible effect on LISA EMRIs.

D. GW Implications

Are such changes in the orbital dynamics measurable with EMRI GWs? Let us first consider the effect of an azimuthal wind, for which the inspiral rate is increased with the timescale $\mathcal{T}_{\text{a.wind}} \equiv \ell / \dot{\ell}_{\text{wind}}$:

$$\mathcal{T}_{\text{aw}}^\alpha \approx -4.0 \times 10^8 \text{ yr} \alpha_1 \dot{m}_\star^3 M_{\bullet 5}^{-1} \bar{r}_{10}^4, \quad (87)$$

for α -disks and

$$\mathcal{T}_{\text{aw}}^\beta \approx -7.1 \times 10^4 \text{ yr} \alpha_1^{4/5} \dot{m}_\star^{7/5} M_{\bullet 5}^{4/5} m_{\star 1}^{-1} \bar{r}_{10}^{19/10}, \quad (88)$$

for β -disks. We have here used the fact that the specific angular momentum is $\ell = r^2 \Omega$ where Ω is given in Eq. (2).

These timescales can now be used to estimate the GW dephasing. The effect of the headwind is to change the

¹⁸ Regular dynamical friction may be significant for standard α and β -disks for retrograde orbits [55].

orbital angular velocity of the EMRI system, i.e. it induces a $\delta\Omega_{\text{wind}}$. This change in frequency can be approximated as $\delta\Omega_{\text{wind}} \sim (\dot{\ell}_{\text{wind}}/\ell)\Omega\delta t$, so the phase shift is proportional to $\mathcal{T}_{\text{aw}} = \dot{\ell}_{\text{wind}}/\ell$. Such a change in orbital frequency induces a change in orbital phase, which we can approximate as $\delta\phi_{\text{aw}} \sim \delta\Omega_{\text{wind}}\delta t \sim (\delta t/\mathcal{T}_{\text{aw}})\phi_{\text{GW}}^{\text{tot}}$. For α -disks we find $\delta\phi_{\text{aw}}^{\alpha} \approx 0.03$ rads, while for β -disks we find $\delta\phi_{\text{aw}}^{\beta} \approx 33$ rads, using a typical set of EMRI and disk parameters and initial separation of $\bar{r}_0 = 20$.

A more accurate measure of the GW phase shift can be obtained by integrating the perturbation to the inspiral rate due to the hydrodynamic drag. The results of a similar calculation was presented in Paper I [50] for a general model, of which the azimuthal wind is a special case. We provide the details of the derivation in Appendix B below. The asymptotic analytical solution is presented in Eqs. (115)-(116), where the coefficient and exponents are given in Table II. For the default parameters, we get that the perturbation to the GW phase is $\delta\phi_{\text{aw}}^{\alpha} \sim 0.03$ rad for α -disks, $\delta\phi_{\text{aw}}^{\beta} \sim 47$ rad for β -disks, assuming BHL accretion is not saturated for the final year of inspiral. Including the limitation by the gas supply does limit the process leading to $\delta\phi_{\text{aw}}^{\alpha} \sim 0.15$ rad for α -disks and $\delta\phi_{\text{aw}}^{\beta} \sim 0.35$ rads for β -disks. The result of the full calculation including all other saturation effects is shown in Figures 1 and 5 for different EMRI masses and final inspiral radii for a one year observation. We conclude then that the azimuthal wind affects the EMRI signal only marginally for typical parameters.

Let us now consider the effect of a radial wind on the GW phase. Since the GW phase is proportional to twice the orbital phase for quasi-circular orbits, the total GW phase shift induced by the radial wind is roughly

$$\delta\phi_{\text{GW}}^{\text{rad. wind}} = 2(\Omega - \Omega_{\text{vac}})T_{\text{obs}} \approx \frac{\dot{M}_{\bullet}m_{\star}}{\Omega_{\text{vac}}Hc_s^3r^2}T_{\text{obs}} \quad (89)$$

$$= 5.0 \times 10^{-10} \text{ rads } M_{\bullet}^{-1}m_{\star}^{-1}\dot{m}_{\bullet}^{-3}\bar{r}_{10}^4. \quad (90)$$

This radial wind is thus completely negligible for the LISA measurement unless $\bar{r} \gtrsim 1000$.¹⁹

VI. AXISYMMETRIC GRAVITATIONAL EFFECTS

The axisymmetric component of the disk gravity induces several effects in the orbital evolution of an EMRI: it modifies the angular velocity of the orbit and the inspiral rate and induces additional apsidal precession for eccentric orbits. We examine these effects here in turn, making order of magnitude estimates of the corresponding GW phase shifts.

¹⁹ Note that $\dot{m}_{\bullet} \ll 1$ is unrealistic for radiatively efficient, thin disk models, but even so, BHL accretion would be quenched by the limited gas supply, as explained in Sec. IV C 3.

A. Accretion Disk Potential

The gravitational potential of a thin disk may be much stronger than the isotropic component of the enclosed mass, $M_{\text{disk}}(\bar{r})/r$. This is to be expected since a thin ring exerts a much stronger force than a spherical shell of the same mass, which can point both in or out for exterior and interior test particles, respectively. Here we estimate the Newtonian gravitational potential of a stationary planar disk.

The total potential of the disk is a superposition of the contributions of infinitesimal concentric rings of mass $dm = 2\pi r dr \Sigma$. Using dimensionless radius variables,

$$\Phi_{\text{disk}}(\bar{r}) = -M_{\bullet} \int_{\bar{r}_{\min}}^{\bar{r}_{\max}} \Sigma(\bar{r}_0) \frac{4\bar{r}_0}{\bar{r} + \bar{r}_0} K\left(\frac{2\sqrt{\bar{r}\bar{r}_0}}{\bar{r} + \bar{r}_0}\right) d\bar{r}_0. \quad (91)$$

where the surface density $\Sigma(\bar{r})$ is to be substituted from Eq. (27) or (33). We here used the fact that a circular ring of mass dm and radius r_0 generates a potential at r as given in Eq. (76). Here \bar{r}_{\min} and \bar{r}_{\max} are the inner and outer radii defining the radial extent of the disk, we assume $\bar{r}_{\min} \sim 0$ and $\bar{r}_{\max} \sim \bar{r}_{\text{rad}}$ in practice [Eq. (31)].

For inclined orbits, with the CO angular momentum vector \mathbf{L}_{\star} at inclination ι relative to the total angular momentum vector of the CO and the disk, the potential generated by the disk can be expressed more conveniently with the Legendre polynomials $P_{\ell}(x)$

$$\Phi_{\text{disk}}(\bar{r}) = -\sum_{\ell=0}^{\infty} 2\pi [P_{2\ell}(0)]^2 P_{2\ell}(\cos \iota) \times M_{\bullet} \int_{\bar{r}_{\min}}^{\bar{r}_{\max}} \Sigma(\bar{r}_0) \bar{r}_0 \frac{\bar{r}_{<}^{2\ell}}{\bar{r}_{>}^{2\ell+1}} d\bar{r}_0, \quad (92)$$

where $\bar{r}_{<} = \min(\bar{r}, \bar{r}_0)$ and $\bar{r}_{>} = \max(\bar{r}, \bar{r}_0)$ [137]. The integrals in Eq. (92) can be simply evaluated analytically for the particular form of $\Sigma(\bar{r})$ given by Eq. (33). In Appendix C 1, we carry out this exercise and show that in the limit $\bar{r}_{\min} \ll \bar{r} \ll \bar{r}_{\max}$,

$$\Phi_{\alpha\text{-disk}}(\bar{r}) \approx -\pi \Sigma_{\alpha 0} \sqrt{\bar{r}_{\max}} \bar{r}^2, \quad (93)$$

$$\Phi_{\beta\text{-disk}}(\bar{r}) \approx 2\pi c_0 \Sigma_{\beta 0} \bar{r}^{2/5}, \quad (94)$$

where $c_0 = 1.38$, and Eq. (33) was used to define the dimensionless density scales $\Sigma_{\alpha 0}$ and $\Sigma_{\beta 0}$ as $M_{\bullet}\Sigma(\bar{r}) = \Sigma_{\alpha 0}\bar{r}^{3/2}$ and $\Sigma_{\beta 0}\bar{r}^{-3/5}$, for α and β -disks, respectively. Substituting $\bar{r}_{\max} = \bar{r}_{\text{rad}}$ from Eq. (31), we get

$$\frac{\Phi_{\text{disk}}(\bar{r})}{\Phi(\bar{r})} \approx \begin{cases} -1.4 \times 10^{-12} \alpha_1^{-20/21} \dot{m}_{\bullet}^{-13/21} M_{\bullet}^{22/21} \bar{r}_{10}^3 & \text{for } \alpha\text{-disks,} \\ 1.2 \times 10^{-9} \alpha_1^{-4/5} \dot{m}_{\bullet}^{3/5} M_{\bullet}^{6/5} \bar{r}_{10}^{-7/5} & \text{for } \beta\text{-disks,} \end{cases} \quad (95)$$

where we have used $\Phi(\bar{r}) = \bar{r}^{-1}$ for the SMBH potential.

Equation (95) shows that the disk potential decreases outwards and inwards for α and β -disks. Thus interestingly, the disk exerts an outward force on the CO for

α -disks. In Appendix C 1, we show that this is due to a strong quadrupolar field generated by the outskirts of a radiation-pressure dominated α -disk.

B. Change in the orbital frequency

The orbital angular frequency $\Omega(\bar{r})$ is modified due to the axisymmetric gravitational field of the disk from its value without the disk Ω_{vac} given by Eq. (2). Equating the centripetal acceleration to the gradient of the gravitational potential we find

$$r\Omega^2 = \frac{M_\bullet}{r^2} + \frac{d\Phi_{\text{disk}}}{dr} = r\Omega_{\text{vac}}^2 + \frac{d\Phi_{\text{disk}}}{dr}. \quad (96)$$

Therefore the orbital frequency is

$$\Omega \approx \Omega_{\text{vac}} \left(1 + \frac{\bar{r}^2}{2} \frac{d\Phi_{\text{disk}}}{d\bar{r}} \right). \quad (97)$$

C. Change in the inspiral rate

The binding energy in the Newtonian approximation is

$$E = \frac{1}{2}\Omega^2 r^2 \eta M - \frac{\eta M^2}{r} + m_* \Phi_{\text{disk}}, \quad (98)$$

where M is the total mass and $\eta = M_\bullet m_*/M^2$ is the symmetric mass-ratio. For EMRIs, $\eta M \approx m_*$ and $M \approx M_\bullet$. Assuming no other source of energy loss, other than the GW emission, and quasi-circular orbits,

$$\frac{dE}{dt} = -\frac{32}{5} \eta^2 M^2 r^4 \Omega^6. \quad (99)$$

We can use Eq. (97) to express the radial and time derivatives of the energy explicitly as a function of radius alone:

$$\frac{dE}{d\bar{r}} = \frac{\eta M}{2\bar{r}^2} \left(1 + 3\bar{r}^2 \frac{d\Phi_{\text{disk}}}{d\bar{r}} + \bar{r}^3 \frac{d^2\Phi_{\text{disk}}}{d\bar{r}^2} \right), \quad (100)$$

$$\frac{dE}{dt} = -\frac{32}{5} \eta^2 \bar{r}^{-5} \left(1 + 3\bar{r}^2 \frac{d\Phi_{\text{disk}}}{d\bar{r}} \right). \quad (101)$$

Therefore the radial velocity is modified as

$$\frac{d\bar{r}}{dt} = \left(\frac{dE}{d\bar{r}} \right)^{-1} \frac{dE}{dt} = \dot{\bar{r}}_{\text{vac}} \left(1 - \bar{r}^3 \frac{d^2\Phi_{\text{disk}}}{d\bar{r}^2} \right), \quad (102)$$

where $\dot{\bar{r}}_{\text{vac}}$ is the GW inspiral rate neglecting the effects of the disk [Eq. (8)]. Notice that the first derivative of the disk potential does not enter the radial velocity.

D. Apsidal precession

While clearly unimportant for quasi-circular EMRIs, we briefly show that the axisymmetric disk gravity causes

a negligible amount of apsidal precession in the eccentric case too.

The radial oscillation frequency for a nearly circular orbit in a perturbed potential is

$$\kappa^2(r) = \frac{M_\bullet}{r^3} + \frac{d^2\Phi_{\text{disk}}}{dr^2} + \frac{3}{r} \frac{d\Phi_{\text{disk}}}{dr}, \quad (103)$$

(see, e.g. [133]). If $\kappa \neq \Omega$, the ellipse precesses in its plane at a rate $\Omega - \kappa$. The dimensionless apsidal precession rate relative to the Keplerian frequency from Eqs. (97) and (103) is thus

$$\frac{\Omega_{\text{ap}}}{\Omega_{\text{vac}}} \equiv \frac{\Omega - \kappa}{\Omega_{\text{vac}}} = -\frac{\bar{r}^3}{2} \left(\frac{d^2\Phi_{\text{disk}}}{d\bar{r}^2} + \frac{2}{\bar{r}} \frac{d\Phi_{\text{disk}}}{d\bar{r}} \right). \quad (104)$$

We relate $\Omega_{\text{ap}}/\Omega_{\text{vac}}$ to the induced phase shift below; this quantity is proportional to $\Phi_{\text{disk}}/\Phi \ll 1$.

E. GW Implications

The disk potential changes the GW frequency and the inspiral rate at fixed orbital radii. The dimensionless change in the frequency $\delta\Omega = (\Omega - \Omega_{\text{vac}})/\Omega_{\text{vac}}$, inspiral rate $\delta\dot{r} = (\dot{r} - \dot{r}_{\text{vac}})/\dot{r}_{\text{vac}}$, and the dimensionless apsidal precession rate $\Omega_{\text{ap}}/\Omega_{\text{vac}}$ are all proportional to derivatives of $\Phi_{\text{disk}}(\bar{r})/\Phi(\bar{r})$, up to a factor of order unity [see Eqs. (97,102,104)]. Equation (95) shows that this ratio is typically very small, at the level of $\Phi_{\text{disk}}/\Phi \sim (2 \times 10^{-6}, 10^{-5})$ for (α, β) -disks with very small α and large M_\bullet and \bar{r} , $(\alpha, M_\bullet, \bar{r}) \sim (10^{-3}, 10^6 M_\odot, 100)$, and even smaller for more typical values. This leads to a small change in the GW phase of Eq. (14). In Appendix C, we carry out a detailed calculation that shows that for both α and β -disks, self-gravity effects induce a dephasing of approximately $10^{-4} - 10^{-7}$ rads for our nominal set of parameters in a one year observation, which is clearly below LISA's observational threshold.

These estimates are modified if the gravitational torques from the CO quenches gas inflow onto the SMBH, and clears a gap (Sec. III B). In this case, the gas density is greatly reduced interior to the CO, but extra gas accumulates outside its orbit, changing the potential. In Appendix C we show that this effect increases the dephasing by roughly an order of magnitude for β -disks, but such an increase is still well below the threshold of detectability. Axisymmetric gravitational effects may be more important for eccentric orbits with large semi-major axis $\bar{r} \sim 1000$.

VII. MIGRATION

Let us now examine the role of non-axisymmetric gravitational effects induced by the disk, which lead to a phenomenon known as “migration” in planetary dynamics. As before, the goal is to make order of magnitude estimates of the migration effect on the GW phase and compare them with the detectability measures of Sec. II B.

A. General Properties

Consider the non-axisymmetric gravitational effects of the disk, leading to angular momentum dissipation, analogous to planetary migration (see [113, 128] for reviews). The orbiting CO exerts a nonzero average gravitational torque on the gaseous disk, creating a spiral density wave. The total angular momentum budget is dissipated through viscosity and the outward angular momentum transport of the spiral density wave. The gravitational torque of the spiral density wave exchanges angular momentum resonantly with the CO causing it to migrate [110]. This effect is analogous to dynamical friction (see Sec. V C), but accounts for the inhomogeneous velocity field of the gaseous medium.

In planetary dynamics, this phenomenon in different regimes is called Type-I, Type-II, and Type-III migration. The distinction is whether a gap is opened (Type-II) or not (Type-I) and whether strong corotation torques related to horseshoe orbits are taken into account (Type-III). In the following we neglect Type-III migration because it is most relevant only if the disk mass near corotating orbits is comparable or larger than the secondary mass. Figure 3 shows that this is not the case for EMRIs in the LISA frequency band.

In a pioneer paper, Goldreich and Tremaine presented the first study on Type I migration, using 2 dimensional (2D) linear perturbation theory [110]. Their results were later improved by Tanaka et. al. to account for corotation resonances and 3D effects in isothermal disks [130], which are also consistent with 3D hydrodynamic simulations of laminar disks [138]. Further generalizations exist for locally adiabatic 2D disks [139]. However, recent MHD shearing box simulations of turbulent protoplanetary disks with a low mass planet show that the torques exhibit stochastic fluctuations for Type I migration, where even the sign of the torque changes rapidly [140, 141]. Stochastic migration is not expected if the satellite is more massive relative to the disk. The migration is also very sensitive to the value of opacity and radiation processes [142]. Recently, Hirata generalized the original study of Goldreich and Tremaine for laminar 2D relativistic disks and found the angular momentum transport to be larger by a factor ~ 4 close to the central BH [143, 144]. Finally, higher order PN corrections may resonantly excite persistent spiral density waves close to the SMBH even without an m_* , which could modify the torque estimates for EMRIs [145].

To our knowledge, Type-I migration is unexplored for the expected environments for LISA EMRI sources: for radiation-pressure-dominated, optically-thick, geometrically-thin, relativistic, magnetized and turbulent disks, where the mass of the perturbing body m_* exceeds the disk's mass. For a simple estimate below, we explore the GW phase shift in an EMRI system due to Type I migration, using the isothermal non-relativistic laminar formulas of Tanaka et. al [130], where we include the effects of radiation pressure by using the correspond-

ing expressions for the sound speed and the scale height.

If the CO is sufficiently massive and/or far out, a central region is cleared out and a circular gap develops (see Sec. III B). Once a gap opens, the angular momentum exchange becomes much more regular than Type-I and it is determined by the angular momentum transport through the more distant part of the disk [138, 140, 141]. This type of angular momentum exchange is referred to as Type II migration. If the local mass of the disk is greater than the mass of the perturbing object, then the object migrates inward on a viscous timescale with the velocity of the accreting gas. However, for LISA EMRI sources, the local disk mass is smaller than the CO's (see Fig. 3). In this case, the migration slows down, and becomes “secondary dominated Type-II migration” [128].

Simple steady-state estimates, based on angular momentum balance, were presented by Syer and Clarke [115]. These estimates account for the increase of the gas density relative to an isolated disk, assuming that the angular momentum exchange is dominated by that near the inner-edge of the disk. Later, Ivanov et. al. [104] relaxed the steady-state assumption and estimated the quasi-stationary, time-dependent evolution of the disk and satellite using a zero stress boundary condition at the location of the binary.

Both of these studies focused on thin, one-zone, gas pressure dominated, Shakura-Sunyaev disks, where the density is an increasing function of stress. This assumption is satisfied for β -disks but not for radiation-pressure dominated α -disks. In the later case, we are not aware of literature that is applicable to Type II migration. Recent studies have shown that migration with an annular gap is affected by global edge-modes for massive disks, and can cause stochastic migration of planets either inward or outward (similar to the Type I case with MHD) [146], and the migration rate is also sensitive to vortex forming instabilities [147]. However, these phenomena have not yet been explored in AGN accretion disks for EMRIs. For an order of magnitude analysis of Type II migration, we use both Syer and Clarke and the asymptotic Ivanov et. al. equations to estimate the corresponding GW phase shifts for EMRIs in β -disks. We make a conservative estimate for radiation-pressure dominated α -disks, based on angular momentum balance between m_* and the local disk, neglecting the accumulation of gas outside the gap.

B. Type-I migration

For an isothermal 3D disk, Type I migration removes or increases angular momentum at a rate

$$\dot{\ell}_{\text{mig,I}} = \pm c_1 \frac{m_* \Sigma r^6 \Omega^4}{M_\bullet^2 c_s^2} = \pm c_1 \frac{m_*}{M_\bullet} \Sigma \frac{r^3}{H^2}, \quad (105)$$

where $c_1 = (1.4 - 0.5\gamma)$ and $\gamma = 3/2$ or $-3/5$ for α and β -disks, respectively, and the \pm signs highlight the stochastic nature of migration in a turbulent disk [130].

The magnitude of c_1 is different for locally adiabatic 2D disks by a factor ~ 2 , but the scaling with other parameters remains the same [139]. Relative to the GW rate of angular momentum loss,

$$\frac{\dot{\ell}_{\text{mig,I}}}{\dot{\ell}_{\text{GW}}} = \begin{cases} \pm 7.2 \times 10^{-11} \alpha_1^{-1} \dot{m}_{\bullet 1}^{-3} M_{\bullet 5} \bar{r}_{10}^8 & \text{for } \alpha\text{-disks,} \\ \pm 5.1 \times 10^{-7} \alpha_1^{-4/5} \dot{m}_{\bullet 1}^{-7/5} M_{\bullet 5}^{6/5} \bar{r}_{10}^{59/10} & \text{for } \beta\text{-disks.} \end{cases} \quad (106)$$

Notice that the Type I migration dominates over even the GW loss of angular momentum at sufficiently large radii, beyond $\bar{r} \approx 150$ for α -disks and $\bar{r} \approx 112$ for β -disks.

C. Type-II migration

If the CO is sufficiently massive and/or far out that a gap opens (see Sec. III B) the CO is subject to Type II migration. The angular momentum exchange depends on the local disk mass near the binary, m_d given by Eq. (35). Typically, $m_d < m_\star$ (see Fig. 3), and the specific angular momentum dissipation rate, in the quasi-stationary approximation of Syer & Clarke [115], is

$$\dot{\ell}_{\text{mig,II,SC}} = \left(\frac{m_d}{m_\star} \right)^k \dot{\ell}_{\text{gas}} = - \left(\frac{m_d}{m_\star} \right)^k \frac{v_{\text{orb}} v_{\text{gas},r}}{2}, \quad (107)$$

where $\dot{\ell}_{\text{gas}}$ is the angular momentum loss in the gas due to viscosity, $v_{\text{gas},r} = 2M_\bullet r/m_d(r)$ is the radial velocity of gas given by Eq. (37), v_{orb} is the orbital velocity Eq. (2), and $k = 3/8$ for electron-scattering opacity and β -disks. If neglecting the banking up of gas near the outer edge of the gap, then angular momentum balance implies $k = 1$, which we adopt conservatively for α -disks [see eq. (42) in Ref. [104]]. We note that this assumption is different than those used in Refs. [53, 99]. Substituting Eqs. (6), (35), and (37),

$$\frac{\dot{\ell}_{\text{mig,II,SC}}}{\dot{\ell}_{\text{GW}}} = \begin{cases} 6.2 \times 10^{-6} \dot{m}_{\bullet 1} M_{\bullet 5}^3 m_{\star 1}^{-2} \bar{r}_{10}^4 & \text{for } \alpha\text{-disks,} \\ 5.8 \times 10^{-3} \alpha_1^{1/2} \dot{m}_{\bullet 1}^{5/8} M_{\bullet 5}^{13/8} m_\star^{-11/8} \bar{r}_{10}^{25/8} & \text{for } \beta\text{-disks.} \end{cases} \quad (108)$$

Notice that for α -disks, this is independent of α ; the dissipation of the CO's angular momentum is proportional to M_\bullet . For β -disks, Eq. (108) also accounts for the accumulation of mass near the CO, which leads to additional angular momentum dissipation, sensitive to α .

We also consider the time-dependent solution of Ivanov et. al. [104] for β -disks that accounts for the accumulation of gas and a zero stress boundary condition at the edge of the gap (see also Eq. (24) in Ref. [148]):

$$\dot{\ell}_{\text{mig,II,IPP}}^\beta = -c_2 v_{\text{orb}} \frac{\dot{M}_\bullet}{m_\star} (r_{\text{dd}} r)^{1/2}, \quad (109)$$

where r_{dd} is the “radius of disk dominance”, which satisfies $m_d(r_{\text{dd}}) = m_\star$ [see Eq. (35)], $c_2 \equiv \{1 + \delta[1 -$

$(r/r_{\text{dd}})^{1/2}]\}^{k_2}$, $\delta = 6.1$, and $k_2 = 0.26$. Note that c_2 is only mildly r dependent. For $r = r_{\text{dd}}$, $c_2 = 1$ so that both estimates [Eqs. (107) and (109)] imply a migration rate tracking the radial velocity of gas, so that $\dot{\ell}_{\text{mig,II,IPP}}^\beta = \dot{\ell}_{\text{mig,II,SC}}^\beta = \dot{\ell}_{\text{gas}} = -v_{\text{orb}} v_{\text{gas},r}/2$, while for $r \ll r_{\text{dd}}$, $c_2 \approx 1.66$, asymptotically independent of r . Similar to Eq. (107), Eq. (109) is valid for electron scattering opacity β -disks, but is not applicable for radiation-pressure dominated α -disks. Substituting Eq. (35) for r_{dd} , we find for $r \ll r_{\text{dd}}$,

$$\frac{\dot{\ell}_{\text{mig,II,IPP}}^\beta}{\dot{\ell}_{\text{GW}}} = 5.1 \times 10^{-4} \alpha_1^{2/7} \dot{m}_{\bullet 1}^{11/14} M_{\bullet 5}^{31/14} m_{\star 1}^{-23/14} \bar{r}_{10}^{-7/2}. \quad (110)$$

D. Quenching of migration

In the following we assume that inside and outside the minimum gap opening radius r_{gap} [Eq. (45–46)] Type-I and Type-II migration operate, where we use Eq. (106) and Eqs. (108–110), respectively. Once the CO has crossed inside r_{gap} , the gas is no longer expelled efficiently by the tidal field of the CO, and the gas is free to flow in on the accretion timescale with a radial velocity $v_{\text{gas},r}$ [Eq. (37)]. If this is faster than the GW inspiral rate of the CO $v_{\star r}$ [Eq. (8)], then the gap can refill. In Sec. III B 1, we have shown that $|v_{\star r}| \leq |v_{\text{gas},r}|$ is satisfied if $\bar{r} \geq \bar{r}_d$, given by Eq. (48). Thus, if $\bar{r} = \bar{r}_{\text{gap}} \geq \bar{r}_d$ is met [see Eqs. (45–46)], we assume that the gap refills, and switch from the disk generated torque from Type-II to Type-I. Otherwise, if a gap has formed and cannot follow the inspiral rate of the CO, disk torques are expected to shift out of resonance, and become too distant for efficient angular momentum exchange. Then the interaction is greatly suppressed, and we assume $\dot{\ell}_{\text{mig}}(\bar{r}) = 0$ if $\bar{r}_{\text{gap}} \leq \bar{r} \leq \bar{r}_d$. Once the gap has formed and decoupled, it can no longer refill, so we further assume $\dot{\ell}_{\text{mig}} = 0$ if $\bar{r} \leq \bar{r}_{\text{gap}} \leq \bar{r}_d$. Finally, if the gap refills (i.e. $\bar{r}_{\text{gap}} \geq \bar{r}_d$) then Type-I migration can operate efficiently even if the inspiral rate is faster than the viscous inflow rate ($\bar{r} \leq \bar{r}_d$), since the spiral patterns can form much faster on a dynamical timescale $t_{\text{dyn}} \sim \Omega^{-1}$. The interaction may be significantly different only much later when the inspiral time $t_{\text{GW}} \equiv r/\dot{r}_{\text{GW}}$ becomes faster than the cooling time of the disk [149], i.e.

$$t_{\text{cool}} \equiv \frac{1}{\alpha \Omega}, \quad (111)$$

where \dot{r}_{GW} is the GW driven inspiral rate, Ω is the orbital angular velocity and α is the parameter in the viscosity prescription. From Eqs. (2), (8), and (111) we get $t_{\text{GW}} < t_{\text{cool}}$ inside

$$\bar{r}_c \equiv 0.055 \alpha_1^{-2/3} M_{\bullet 5}^{-2/3} m_{\star 1}^{2/3}. \quad (112)$$

Typically the disk cooling does not impose a limitation outside the ISCO for EMRIs unless α is very small and the mass-ratio is not extreme.

To summarize we assume,

$$\dot{\ell}'_{\text{mig}} = \begin{cases} \dot{\ell}_{\text{mig,I}}, & \text{if } \bar{r} < \bar{r}_{\text{gap}}, \\ \dot{\ell}_{\text{mig,II}}, & \text{if } \bar{r} > \bar{r}_{\text{gap}}, \end{cases} \quad (113)$$

and

$$\dot{\ell}_{\text{mig}} = \begin{cases} 0 & \text{if } \bar{r} < \bar{r}_c \text{ or } \bar{r}_{\text{gap}} < \bar{r} < \bar{r}_d \\ & \text{or } \bar{r} < \bar{r}_{\text{gap}} < \bar{r}_d, \\ \dot{\ell}'_{\text{mig}} & \text{otherwise,} \end{cases} \quad (114)$$

where for $\dot{\ell}_{\text{mig,I}}$ we use Eq. (106), while for $\dot{\ell}_{\text{mig,II}}$ either the Syer-Clarke model Eq. (108) or the Ivanov et. al. model (110). The later is only available for β -disks in the radiation-pressure dominated regime, while the Syer-Clarke is applicable both for α or β -disks. In summary, we consider three cases for migration, which utilize the same Type-I model, but differ in the Type-II regime

1. M α_{SC} : α -disks with Syer-Clarke Eq. (108);
2. M β_{SC} : β -disks with Syer-Clarke Eq. (108);
3. M β_{IPP} : β -disks with Ivanov et. al. Eq. (109).

E. GW Implications

The change in the angular momentum dissipation rate modifies the GW driven inspiral rate, which modifies the GW phase evolution. The corresponding phase shift $\delta\phi_{\text{GW}}$ can be calculated in a similar way as for an azimuthal wind (see Sec. V D above, and Paper I [50]). The interested reader can find the details of the derivation in Appendix B.

For the default parameters, we find that Type-I migration produces a typical GW dephasing on the order of 10^{-2} and 10 radians during the final year of observation in α and β -disks, respectively. The large increase in dephasing for the β -disk case is due to the much larger surface density.

Even more interesting is the case where a gap opens; Type-II migration is clearly the most dominant perturbation among all the ones considered in this paper. However, as showed in Sec. III B, a gap is expected to close for most EMRIs in the LISA band. For α -disks, Type-II migration can generate GW phase shifts of order $10 - 100$ radians in one year, and up to $10^3 - 10^4$ rad for β -disks. The modifications to the GW spectrum are so large that if this effect is in play, that vacuum EMRI templates might be ineffective to extract LISA GWs. The blue lines in Figure 1 and 5 show the phase shift due to migration as a function of final orbital radius including quenching effects [Eq. (114)] for both Type-II migration models (Syer & Clarke steady state and the Ivanov et. al. quasi-stationary models, Eq. (108) and (110), respectively), assuming $\alpha_1 = \dot{m}_{\bullet,1} = 1$. For other system parameters and observation times, we provide asymptotic analytical expressions in Eqs. (115–116) and Table II below.

	$(10, 10^5)$	$(10^2, 10^5)$	$(10, 10^6)$	$(10^2, 10^6)$
Primary acc.	1.0 (-3)	1.0 (-3)	1.0 (-3)	1.0 (-3)
BHL α	1.9 (+0)	4.6 (-3)	5.7 (-3)	2.9 (-3)
BHL β	4.6 (+0)	0.0 (+0)	1.8 (+1)	7.0 (+0)
W α	1.5 (-2)	8.0 (-5)	8.0 (-4)	1.1 (-4)
W β	1.4 (-1)	0.0 (+0)	3.2 (-1)	8.3 (-1)
SG α	2.5 (-5)	4.9 (-5)	4.5 (-6)	8.7 (-6)
SG β	6.8 (-4)	5.5 (-4)	1.1 (-3)	8.9 (-4)
M α_{SC}	6.2 (-3)	1.8 (-1)	2.4 (-6)	9.6 (-5)
M β_{SC}	6.9 (+2)	1.8 (+2)	7.3 (-2)	8.8 (-1)
M β_{IPP}	8.2 (+1)	1.4 (+1)	7.3 (-2)	8.8 (-1)

TABLE I. Summary of accretion disk effects on the GW phase shift induced by different accretion disk effects relative to vacuum waveforms. Rows correspond to different accretion disk effects: Primary Eddington-limited accretion (Primary acc.), secondary Bondi-Hoyle-Lyttleton (BHL) accretion, azimuthal winds (W), disk's self-gravity (SG) and migration (M). Columns correspond to different EMRI systems assuming a 1 year observation. The entries $x(y)$ denote $x \times 10^y$ in radians. The phase shift is negative for all effects except for SG α . Observe that β -disk migration is the dominant effect for the first two columns, while β -disk BHL accretion is dominant for the last two columns.

VIII. COMPARISON OF ACCRETION DISK EFFECTS

We summarize the GW phase shift generated by the dominant accretion disk effects in Table I. Different rows show different accretion disk effects with the parameters of Eq. (26), while columns show different EMRI systems with component masses given by all four combinations of $M_{\bullet} = (10^5, 10^6) M_{\odot}$ and $m_{\star} = (10, 100) M_{\odot}$. The entries represent the GW phase shift between the standard vacuum waveform and those including the effects of the accretion disk in the Newtonian approximation. The phase shift is between one-year long GW waveforms with the same final radius in the most sensitive LISA frequency band.²⁰ $(\bar{r}_f, \bar{r}_0) \approx (16, 25)$ for $(M_{\bullet}, m_{\star}) = (10^5, 10) M_{\odot}$; $(\bar{r}_f, \bar{r}_0) \approx (16, 42)$ for $(M_{\bullet}, m_{\star}) = (10^5, 10^2) M_{\odot}$; $(\bar{r}_f, \bar{r}_0) \approx (3, 7.6)$ for $(M_{\bullet}, m_{\star}) = (10^6, 10) M_{\odot}$; $(\bar{r}_f, \bar{r}_0) \approx (3, 13)$ for $(M_{\bullet}, m_{\star}) = (10^6, 10^2) M_{\odot}$. The phase shift estimates are derived in Appendix A, B, and C, using Eqs. (A10), (B8), and (C5), where the underlying quantities \dot{m}_{\star} , ℓ and Φ_{disk} are substituted from Sec. IV–VI, taking into account all of the quenching mechanisms that are in play. In particular, for migration we use Type I and Type II in the appropriate radial ranges without and with gaps, respectively, where we utilize either the Syer-Clarke (SC) or the Ivanov et. al. (IPP) model for Type

²⁰ Here we don't marginalize over an arbitrary phase shift between the two waveform templates for simplicity. These estimates are in good agreement with the more complicated calculations presented in Sec. X below.

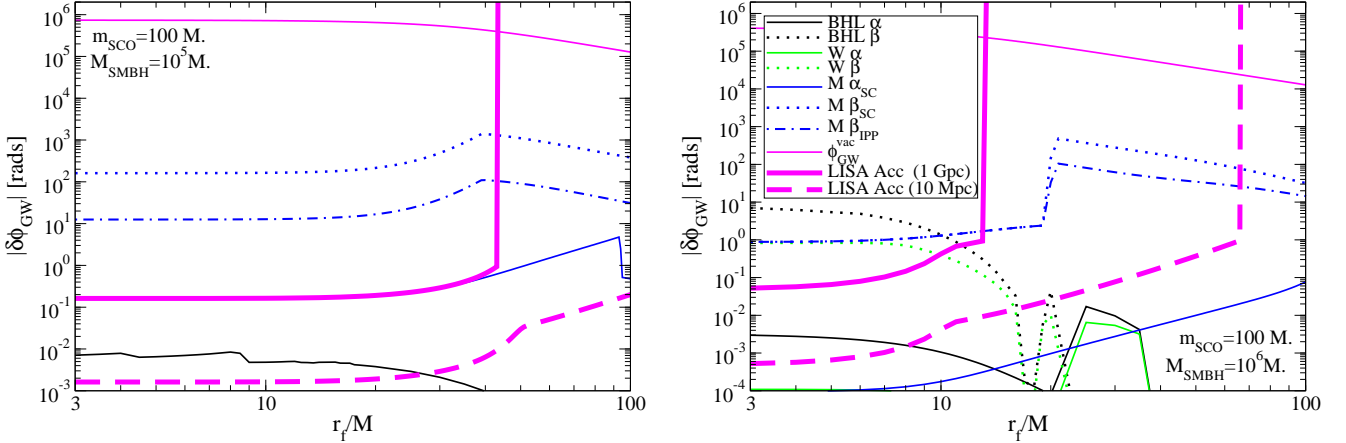


FIG. 5. The GW phase shift as a function of final radius in units of M_\bullet induced by different accretion disk effects relative to vacuum waveforms. As in Fig. 1, solid curves correspond to α -disks, while dotted ones to β -disks. Different color curves represent different accretion disk effects ($\alpha_1 = \dot{m}_{\bullet 1} = 1$): black is for secondary Bondi-Hoyle-Lyttleton (BHL) accretion, green is for azimuthal winds (W) and blue is for migration (M), with dotted and dot-dashed curves for β -disks in the Syer-Clarke and Ivanov et. al. model respectively. The thin, solid magenta line is the total accumulated GW phase in vacuum, while the thick, solid (dashed) magenta line is a measure of the sensitivity to which LISA can measure the GW phase for a source at 1 Gpc (10 Mpc). This figure presents similar conclusions to those found in Fig. 1, but for a different set of EMRI parameters.

II migration, see Sec. VII D.²¹

Table I shows that the migration estimate incorporating the SC model in β -disks is by far dominant, followed by migration using IPP in β -disks, and BHL accretion. The effects of the disk's self-gravity, wind effects, migration in α -disks and Eddington-limited accretion onto the SMBH are all completely negligible for LISA EMRIs. All effects studied lead to a reduction of phase cycles in a fixed observation time for fixed final radius, except for the effect of disk gravity in α -disks. Other detectable EMRIs not shown in this table (different masses and/or orbital radii) might be more sensitive to disk effects.

Figures 1 and 5 show GW phase difference induced by various disk effects as a function of final orbital radius. Solid curves correspond to α -disks, and dotted curves to β -disks. Curve colors represent different accretion disk effects: black curves correspond to BHL accretion, green curves to azimuthal wind effects, and blue curves to migration (dotted for SC- β , dot-dashed for IPP- β). Left and right panels correspond to different mass ratios and SMBH masses. Additionally, Figs. 1 and 5 include three disk-independent reference curves. The thin, solid magenta line is the total accumulated GW phase without disk effects. The thick magenta curves represent the approximate accuracy to which LISA can measure the GW phase as a function of radius, using the simple estimates given by Eq. (19) for a typical source located at 1 Gpc (solid) and 10 Mpc (dashed). We present more detailed estimates of measurement accuracy in Sec. X below.

Typically migration in β -disks generates the dominant phase shift for all final radii. The large drop in the right panel occurs because the gap closes around $\bar{r} \sim 20.4$ for β -disks for these masses, changing Type-II into Type-I migration²². BHL accretion follows migration in importance, and in certain cases (as in the right panel of the figure), the former can be the most important effect if the gap refills. The sudden quenching features in the BHL accretion curves are due to EM radiation pressure, where photon diffusion becomes sufficiently short for EM radiation to escape the flow. Observe that LISA is sensitive to EMRIs that are close to the SMBH (e.g. $\bar{r} \lesssim 50$); the sharp rise of the LISA accuracy estimate is because EMRIs at larger radii are not detected with SNR of 10 or bigger. All disk effects above the thick magenta line are significant and possibly measurable, while wind effects and self-gravity effects (not shown in the figure) always lead to dephasings of order 1 radian or much less. These figures suggest that GW observations may be used to test the predictions of different accretion disk models.

We note that for the masses in the left panel of Fig. 5, the CO is located at $\bar{r}_* = 43$ and $\bar{r}_* = 51$ one and two years prior to merger. A gap is open beyond $\bar{r}_* > \bar{r}_{gap} = 96$ and 5 for α and β -disks. The EMRI evolution becomes much faster than the viscous inflow and the gap decouples at a radius of $\bar{r}_d = 39$ for a β -disk.

To describe the phase shift for different observation times or accretion disk parameters than those shown in Figures 1 and 5, we provide analytical expressions for the asymptotic phase shift for various processes in two limits,

²¹ To understand which quenching mechanisms are in effect for the particular cases, see Figure 4 in Sec. IV C 6.

²² Gap decoupling does not occur since $\bar{r}_d \sim 19.2$.

	C_1 [$\delta\phi_{\text{GW}}^{\text{long}}$]	C_2 [$\delta^2\phi_{\text{GW}}^{\text{long}}$]	c_1 [α_1]	c_2 [$\dot{m}_{\bullet 1}$]	c_3 [$M_{\bullet 5}$]	c_4 [$m_{\star 1}$]	c_5 [yr]	c_6 [$\bar{r}_{f,10}$]	D_1 [$\delta\phi_{\text{GW}}^{\text{short}}$]	D_2 [$\delta^2\phi_{\text{GW}}^{\text{short}}$]	d_3 [$M_{\bullet 5}$]	d_4 [$m_{\star 1}$]	d_5 [yr]	d_6 [$\bar{r}_{f,10}$]
BHL α	6.9 (+0)	3.2 (-1)	-1	-5	-17/4	17/8	25/8	5/2	2.5 (+0)	-2.6 (+0)	-4	2	3	1/2
BHL β	3.2 (+3)	3.2 (-1)	-4/5	-17/5	-3	8/5	13/5	5/2	5.7 (+3)	8.2 (+0)	-19/5	2	3	-8/5
SB	1.3 (+1)	3.7 (-1)	0	1	3/4	-11/8	13/8	5/2	4.2 (+2)	2.8 (+1)	-2	0	3	-11/2
Wind α	3.4 (-2)	8.4 (-4)	-1	-3	-13/4	13/8	21/8	21/2	1.5 (-2)	8.2 (+0)	-2	1	2	5/2
Wind β	4.7 (+1)	4.3 (-3)	-4/5	-7/5	-2	11/10	21/10	42/5	8.6 (+1)	1.4 (+1)	-9/5	1	2	2/5
SW α	1.5 (-1)	7.9 (-2)	0	3	7/4	-15/8	9/8	9/2	2.6 (+0)	2.5 (+1)	0	-1	2	-7/2
SW β	3.5 (-1)	7.9 (-2)	0	3	7/4	-15/8	9/8	9/2	6.2 (+0)	2.5 (+1)	0	-1	2	-7/2
M1 α	4.0 (-3)	8.4 (-4)	-1	-3	-13/4	13/8	21/8	21/2	1.8 (-3)	8.2 (+0)	-2	1	2	5/2
M1 β	7.0 (+0)	4.3 (-3)	-4/5	-7/5	-2	11/10	21/10	42/5	1.3 (+1)	1.4 (+1)	-9/5	1	2	2/5
M2 α_{SC}	2.5 (+1)	1.8 (-2)	0	1	3/4	-11/8	13/8	13/2	1.5 (+2)	1.9 (+1)	0	-1	2	-3/2
M2 β_{SC}	1.5 (+4)	3.5 (-2)	1/2	5/8	-3/16	-31/32	45/32	45/8	1.5 (+5)	2.2 (+1)	-11/8	-3/8	2	-19/8
M2 β_{IPR}	1.6 (+3)	2.7 (-2)	2/7	11/4	3/14	-8/7	3/2	6	1.3 (+4)	2.0 (+1)	-11/14	-9/14	2	-2
SG α	2.2 (-5)	1.7 (-2)	-20/21	-13/21	-59/84	3/8	11/8	11/2	5.8 (-6)	-1.8 (+1)	1/21	0	1	3/2
SG β	-6.1 (-4)	-1.0 (-2)	-4/5	3/5	1/4	-1/40	39/40	39/10	-9.7 (-4)	7.8 (+0)	1/5	0	1	-1/10

TABLE II. Constant coefficients and exponents in Eqs. (115–116) for long and short observations (columns), for different effects (rows). We use the notation $x(y) = x \times 10^y$ in radians. Observe again that the dominant dephasing is due to Type-II migration (M2) both in the short- and long-observation limits. Also notice that all dephasing scales with positive powers of the radius (i.e. $c_6 > 0$ and $d_6 > 0$), implying accretion disk effects become stronger for EMRIs orbiting at larger separations.

namely

$$\delta\phi_{\text{GW}}^{\text{long}} = -C_1 \alpha_1^{c_1} \dot{m}_{\bullet 1}^{c_2} M_{\bullet 5}^{c_3} m_{\star 1}^{c_4} T_{\text{yr}}^{c_5} \left(1 - C_2 \frac{M_{\bullet 5}^{c_6/2}}{m_{\star 1}^{c_6/4}} \frac{\bar{r}_{f,10}^{c_6}}{T_{\text{yr}}^{c_6/4}} \right) \quad (115)$$

$$\delta\phi_{\text{GW}}^{\text{short}} = -D_1 \alpha_1^{d_1} \dot{m}_{\bullet 1}^{d_2} M_{\bullet 5}^{d_3} m_{\star 1}^{d_4} T_{\text{yr}}^{d_5} \bar{r}_{f,10}^{d_6} \times \left(1 - D_2 \frac{m_{\star 1}}{M_{\bullet 5}^2} \frac{T_{\text{yr}}}{\bar{r}_{f,10}^4} \right), \quad (116)$$

where the (C, c, D, d) parameters are given by the rows of Table II. Here $d_1 \equiv c_1$ and $d_2 \equiv c_2$. The first (second) formula is applicable if the observation time is much shorter (longer) than the inspiral time [Eq. (13)]. The particular processes are represented by rows in order: the full BHL rate (i.e. assuming no quenching throughout the observation), the supply limited BHL rate (SB, using Eq. 62 throughout the observation), the corresponding hydrodynamic drag from the azimuthal wind for the full BHL accretion and SB (W and SW, respectively), Type-I migration (i.e. assuming a gap is not present throughout the observation), steady-state Type-II migration, quasi-stationary Type-II migration (i.e. assuming a gap is open throughout the observation), and disk self-gravity (SG). Note that LISA observations are sensitive to the combinations $\alpha_1^{c_1} \dot{m}_{\bullet 1}^{c_2}$, see corresponding columns.

Most accretion disk effects are several orders of magnitude larger for β -disks relative to α -disks. This is because β -disks can be much more massive in the regime of interest for EMRIs. In particular, this suggests the GW phase shift may be used to test the predictions of different accretion disk models.

IX. RELATIVISTIC WAVEFORMS AND DETECTION

Next, we consider accretion disk effects in more realistic waveform models. EMRI GWs are highly relativistic, with velocities close to the speed of light and sometimes skimming the SMBH horizon. As such, Newtonian waveform estimates for GW data analysis are inaccurate. Here we investigate the relativistic correction to the EMRI dynamics using the extended one body framework, and make simple estimates on the imprint of accretion disk effects on the GW waveform. This analysis, however, continues to neglect relativistic corrections to accretion disk effects.

A. Systems Investigated

In the rest of this paper, we restrict our investigations to the following two representative EMRI systems:

- **System I:** Masses $M_{\bullet} = 10^5 M_{\odot}$, $m_{\star} = 10 M_{\odot}$, spin parameter $a_{\bullet}/M_{\bullet} = 0.9$, observation time $T = 1 \text{ yr}$, range of orbital radius $\bar{r} \in (16, 25)$, orbital velocity $v/c \in (0.2, 0.25)$, GW frequency $f_{\text{GW}} \in (0.005, 0.01) \text{ Hz}$, GW phase $\phi_{\text{GW}} \sim 1.3 \times 10^6 \text{ rad}$.
- **System II:** Masses $M_{\bullet} = 10^6 M_{\odot}$, $m_{\star} = 10 M_{\odot}$, spin parameter $a_{\bullet}/M_{\bullet} = 0.9$, observation time $T = 1 \text{ yr}$, range of orbital radius $\bar{r} \in (3, 7)$, orbital velocity $v/c \in (0.37, 0.54)$, GW frequency $f_{\text{GW}} \in (0.003, 0.01) \text{ Hz}$, GW phase $\phi_{\text{GW}} \sim 9 \times 10^5 \text{ rad}$. The ISCO is located at $\bar{r}_{\text{ISCO}} \approx 2.32$.

Figures 1 and 5 shows that accretion disk effects are expected to be significant for these systems.

We make the following simplifying assumptions. First, we consider only quasi-circular EMRIs on the equatorial plane, such that the orbital angular momentum is perpendicular to the SMBH's spin angular momentum. We have also investigated Systems with spin anti-aligned or zero and found similar results. The accretion disk is also assumed to be on the equatorial plane, such that the EMRI is completely embedded in the disk. We ignore the CO's spin angular momentum, as well as sub-leading mass-ratio terms in the radiation-reaction fluxes and in the Hamiltonian.

Such simplifying assumptions make the problem analytically tractable within the EOB framework, employed here for waveform modeling. As of the writing of this paper, the EOB framework for EMRIs has not been sufficiently developed for non-equatorial orbits; it has, however, been satisfactorily tested for equatorial orbits with extreme or comparable mass-ratios, $q \lesssim 10^{-4}$ and $q \gtrsim 10^{-2}$.

We expect that many accretion disk effects (migration, BHL, and wind effects) will be maximal for the equatorial EMRIs studied here. Other effects, however, are substantially different for EMRIs inclined with respect to the accretion disk. Similarly, disk effects may excite eccentricity, which may dramatically increase the impact of accretion disk effects on the GW observables [46, 47, 53, 54]. A study of non-equatorial or eccentric EMRIs with an accretion disk is beyond the scope of this paper.

B. Basics of the EOB Framework

We employ the adiabatic EOB framework of [73–75] to model EMRI waveforms. The EOB scheme was first proposed in [150, 151] to model the coalescence of comparable-mass BH binaries. Since then, this scheme has been greatly enhanced and extended to other type of systems [152–163]. Waveforms constructed in this way have been successfully compared to a set of numerical relativity results [164–166] and to self-force calculations [167, 168]. Recently, [73–75] proposed the combination of EOB and BH perturbation theory techniques to model EMRI waveforms for LISA data-analysis purposes. This is the scheme we adopt in this paper.

In the adiabatic, EOB framework for quasi-circular EMRIs, the GW phase can be obtained by solving the adiabatic equation

$$\dot{\Omega} = - \left(\frac{dE}{d\Omega} \right)^{-1} \mathcal{F}_{\text{GW}}(\Omega), \quad (117)$$

where $\Omega \equiv \dot{\phi}$ is the orbital angular frequency (Eq. (2) but with relativistic corrections), overhead dots stand for time derivatives, E is the binary system's total binding energy and $\mathcal{F}_{\text{GW}} \equiv dE_{\text{GW}}/dt$ is the GW energy flux. We have here implicitly assumed a balance law: all loss of gravitational binding energy is removed only by GW radiation, $dE/dt = -dE_{\text{GW}}/dt$.

The binary's binding energy in a Kerr background for a quasi-circular orbit is simply given by [169]

$$E = \mu \frac{1 - 2\bar{r}^{-1} + \chi_{\bullet}\bar{r}^{-3/2}}{\sqrt{1 - 3\bar{r}^{-1} + 2\chi_{\bullet}\bar{r}^{-3/2}}}. \quad (118)$$

where $\mu \equiv M_{\bullet}m_{\star}/M$ is the reduced mass, with $M \equiv M_{\bullet} + m_{\star}$ the total mass, $\bar{r} \equiv r/M$, and $\chi_{\bullet} \equiv a_{\bullet}/M_{\bullet}$ is the reduced Kerr spin parameter. Notice that it is the binding energy that drives the orbital evolution, and not the total energy of the system, which would also account for the rest-mass energy.

We employ here the factorized form of the GW flux, considered in [158, 161, 162], with the assumption of adiabaticity:

$$\mathcal{F}_{\text{GW}}(\Omega) = \frac{1}{8\pi} \sum_{\ell=2}^8 \sum_{m=0}^{\ell} (m\Omega)^2 |R h_{\ell m}|^2, \quad (119)$$

where R is the distance to the observer, m is the azimuthal quantum number of the multipolar-decomposed waveform, and

$$h_{\ell m} = h_{\ell m}^{\text{Newt}, \epsilon_p} S_{\ell m}^{\epsilon_p} T_{\ell m} e^{i\delta_{\ell m}} (\rho_{\ell m})^{\ell}, \quad (120)$$

and where ϵ_p is the multipolar waveform parity (i.e. $\epsilon_p = 0$ if $\ell + m$ is even, $\epsilon_p = 1$ if $\ell + m$ is odd). All the terms in Eq. (120) ($S_{\ell m}^{\epsilon_p}$, $T_{\ell m}$, $\delta_{\ell m}$ and $\rho_{\ell m}$) are functions of (r, ϕ, Ω) that can be found in [158, 161, 162]. The Newtonian part of the waveform is given by

$$h_{\ell m}^{\text{Newt}, \epsilon_p} \equiv \frac{M_{\bullet}}{R} n_{\ell m}^{(\epsilon_p)} c_{\ell+\epsilon_p} v^{\ell+\epsilon_p} Y_{\ell-\epsilon_p, -m}(\pi/2, \phi). \quad (121)$$

where $Y_{\ell,m}(\theta, \phi)$ are the standard spherical harmonics, $n_{\ell m}^{(\epsilon_p)}$ and $c_{\ell+\epsilon_p}$ are numerical coefficients that depend on the mass-ratio [161]. The orbital velocity v is related to the orbital frequency via $v = (M\Omega)^{1/3}$, which then implies the binary orbital separation is

$$\bar{r} = \frac{[1 - \chi_{\bullet}\bar{\Omega}]}{\bar{\Omega}^{2/3}}, \quad (122)$$

where recall that the overhead bar stands for normalization with respect to total mass: $\bar{\Omega} = M\Omega \approx M_{\bullet}\Omega$.

At this stage one might be slightly confused, as the right-hand side of the evolution equation one wishes to solve (Eq. (117)) depends on a variety of quantities, including the orbital separation and the orbital phase. The assumption of adiabatic quasi-circularity allows us to replace the orbital separation in terms of the orbital frequency via Eq. (122). By definition, the orbital phase is related to its frequency via the differential equation $\dot{\phi} = \Omega$. This equation, together with Eq. (117) forms a closed system of coupled, first-order partial differential equations that can be consistently solved.

The flux in Eq. (119), however, is not sufficiently accurate to model EMRIs. First, it neglects the loss of energy due to the absorption of GWs by the MBH. Second, it

is built from a PN expansion, which is in principle valid only for slowly-moving sources, which EMRIs are not. This flux can be improved by linearly adding BH absorption terms and by adding calibration coefficients to Eq. (119) that are fitted to a more accurate, numerical flux. This is the procedure proposed in [73–75], which we follow here. We include up to 8 calibration coefficients, obtained by fitting to a more accurate Teukolsky evolution in the point-particle limit, as given in Eqs. (26)–(29) of [75], as well as BH absorption terms as given in Appendix B of [75].

Initial data for the evolution of the system of differential equations is obtained through a mock evolution, started at $r = 100M_\bullet$ and ended at $f_{\text{GW}} = 0.01$ Hz (see e.g. [73–75]). The mock evolution is initialized with the post-circular data of [151]. Once the evolution terminates, one can read initial data one-year prior to that point directly from the numerical evolution of the mock simulation. We obtain initial data of such form separately both in the case of vacuum EMRIs and for EMRIs in an accretion disk, as the evolutions are generically different. Once the orbital phase is obtained by solving Eq. (117) with this initial data, the waveforms are readily obtained through Eq. (120).

Before proceeding, let us comment on the differential system one must solve numerically. As already mentioned, since the source of Eq. (117) depends both on orbital phase and frequency, there are truly two coupled, first-order differential equations that must be solved. But the source term of this equation is incredibly more complicated than implied here. Even though $S_{\ell m}$, $T_{\ell m}$, $\delta_{\ell m}$ and $\rho_{\ell m}$ are known analytically as functions of ϕ and Ω , each term contains very long and complicated series expansions with fractional exponents that include special functions, such as the polygamma function. For this reason, the EOB evolution is not a simple integration, as it naively appears to be in this section. Instead, the coupled set of first order equations must be solved simultaneously via numerical methods, where here we employ a partially optimized, Mathematica routine.

C. Disk Modifications to EOB GWs

GW modeling in the adiabatic EOB framework depends sensitively on the energy E and the flux \mathcal{F}_{GW} . Modifications to the MBH or the CO mass naturally change all mass scales that depend on the total mass M , such as the symmetric mass-ratio η . Radiation pressure and migration modifies the rate of change of the angular momentum and thus the flux. In what follows, we explain how we modify the EOB scheme to account for such disk effects.

1. Effective Hamiltonian

The effective Hamiltonian controls the conservative evolution of the EOB model. We have considered several accretion disk effects that directly modify the Hamiltonian, such as the self-gravity of the disk and the increase in mass of the SMBH and the CO. Of these effects, the latter has been found to be the largest. We concentrate on this effect here.

The increase in the CO’s mass can be modeled by solving for the time evolution of m_\star . The differential equation that controls this evolution is Eq. (63), where M_\bullet^{flux} is given in Eq. (62), while \dot{m}_\star^B is given by Eq. (61). Notice that \dot{m}_\star depends on radius, or on orbital frequency by Eq. (122), which itself is a function of time. Since the accretion rate is not constant, one must solve the system of differential equations on Ω and m_\star consistently, which we do numerically and perturbatively as follows. First, we solve the frequency evolution equation, setting m_\star to a constant and neglecting accretion. Second, we use Eq. (122) to rewrite Eq. (63) in terms of orbital frequency. Third, we replace this orbital frequency by the time-evolution obtained in vacuum. Fourth, we numerically solve the evolution equation for \dot{m}_\star , as its source now depends only on time. In step two, we are implicitly discarding non-linear terms that scale as $(\dot{m}_\star T_{\text{obs}})^2$, i.e. the square of the accretion rate times the observation time. This quantity is approximately 10^{-8} or much smaller (clearly much smaller than unity) for typical LISA observation times.

Once the time evolution for the CO’s mass has been obtained, one must then make sure that all quantities that depend on it are properly promoted to time functions. For example, all quantities that depend on the total mass, such as the symmetric mass-ratio η or the reduced mass μ are modified. In particular, the numerical code used to solve the differential equation (Eq. (117)) is naturally written in dimensions of the total mass of the system, which now becomes a time-function. A simple trick to deal with this is to rescale all mass-quantities by the factor $M(t)/M(0)$, which is equal to unity initially, but deviates from unity with time. In particular, this implies that $\bar{\Omega} \rightarrow [M(t)/M(0)]\bar{\Omega}$ and $\bar{r} \rightarrow [M(t)/M(0)]^{-1}\bar{r}$.

Once these substitutions have been made, one can solve for the frequency and phase evolutions, with $m_\star(t)$ a function of time, by providing appropriate initial data. When considering BHL accretion, we choose the same initial data as in the vacuum case (as explained in the end of Sec. IX B) one year prior to reaching a GW frequency of 10^{-2} Hz. The frequency and phase evolution can be compared when m_\star is a constant and when it is not, which provides a measure of the effect of BHL accretion on GWs.

2. Radiation-Reaction Force

The radiation-reaction force controls the rate at which orbits inspiral. This force can be expressed in terms of the rate of change of orbital elements, such as binding energy, angular momentum and the Carter constant. Since we restrict attention to an equatorial, quasi-circular EMRI geometry, we need to consider only the energy flux.

Modifying the EOB model to account for a different radiation-reaction force amounts to the rule

$$\mathcal{F}_{\text{GW}} \rightarrow \mathcal{F}_{\text{GW}} \left(1 + \frac{\delta \dot{\ell}}{\dot{\ell}_{\text{GW}}} \right) \quad (123)$$

in Eq. (117). When modeling an azimuthal wind, $\delta \dot{\ell} = \dot{\ell}_{\text{wind}}$ via Eq. (80), while when modeling migration, then $\delta \dot{\ell}$ is given by Eqs. (114); all throughout $\dot{\ell}_{\text{GW}}$ is given by Eq. (6) with $e = 0$. When substituting in for $\delta \dot{\ell}$ one must be careful to use the properly quenched \dot{m}_* (Eq. (70)), if the accretion disk effect depends on the rate of BHL accretion. All other aspects of the framework can be left unchanged, as Eq. (123) automatically induces deviations from the Kepler relation.

The system of EOB differential equations can now be solved using appropriate initial data. Initial conditions for the vacuum and accretion-disk case are prescribed via mock evolutions as explained in detail in Sec. IX B, with $\delta \dot{\ell} = 0$ and $\delta \dot{\ell} \neq 0$ respectively. As explained above, this guarantees that both simulations will terminate at the same orbital separation. Due to different radiation-reaction force laws, however, the starting radii or frequencies are different in each case for a fixed observation time. To account for this, we will later maximize comparison measures over a time and phase shift between vacuum and accretion disk waveforms, as we explain in Sec. X A.

X. DATA ANALYSIS CONSIDERATIONS

We are now ready to perform a more detailed data analysis study of the accretion disk effects on waveforms. We begin by investigating the dephasing of the EOB waveforms constructed in the previous section. We then continue with an overlap study and end with a discussion of degeneracies between accretion disk parameters and EMRI system parameters.

A. Dephasing Analysis

As explained in Sec. II B 2, a dephasing study is useful to roughly determine whether two waveforms can be distinguished from each other given a GW detection; if the phase difference or *dephasing* between waveforms is large enough, then they are distinguishable (see

Eq. (19)). Here, we compare the dephasing of the dominant, $(\ell, m) = (2, 2)$ vacuum and non-vacuum GW modes, initialized with the data of Sec. IX B.

If we take one waveform to be “the signal” and the other to be “the template,” then the dephasing depends on two extrinsic parameters contained in the template: an overall phase $\delta\phi$ and time shift δt . We here study the dephasing after minimizing it with respect to these extrinsic parameters. The template also depends on other parameters, such as the masses and spins, but we here set these to be equal to the signal’s parameters, i.e. we do not minimize the dephasing over such parameters. In a realistic data analysis implementation, one would maximize the SNR (or minimize the dephasing) over all parameters, at the cost of introducing error into parameter estimation due to the use of incorrect templates.

Before minimizing the dephasing over a time and a phase shift, it is worth pointing out that its magnitude (computed with relativistic EOB waveforms) roughly agrees with the Newtonian results presented in Table I. For example, the final dephasing after 12 months of evolution (initializing the simulations with the same final frequency and the same initial phase) between vacuum and β -disk migration is ~ 217 rads with the EOB model and ~ 670 rads with the Newtonian estimates for System I. In this case, the relativistic model leads to a larger dephasing than the Newtonian estimates because, in the latter, Sys. I evolves more rapidly due to relativistic corrections and the CO spends less time in the Type-II dominated region. We have verified that for weakly-relativistic EMRIs, where only Type-I or Type-II migration is in play, Newtonian and EOB dephasings agree.

A more appropriate measure of distinguishability, however, requires that one minimizes the dephasing with respect to δt and $\delta\phi$. Following the prescription of Eq. (23) in [165], we search for a δt and $\delta\phi$ such that $\|f_1(t+\delta t) - f_2(t)\| \leq \delta_f$ and $\|\phi_1(t+\delta t) - \phi_2(t) - \delta\phi\| \leq \delta_t$, where $\phi_{1,2}$ and $f_{1,2}$ are the dominant GW phase and frequencies for waveforms $h_{1,2}(t)$. The $\|A\|$ notation stands for the integral of A over a time window of length $64\lambda_{\text{GW}}$, where λ_{GW} is the GW wavelength (see e.g. [75] for details). The signal $h_1(t)$ is assumed to be a vacuum template, while h_2 is a non-vacuum template for a specific accretion disk effect. We choose the tolerances $\delta_f = 10^{-11}$ and $\delta_t = 10^{-6}$; decreasing these magnitudes does not visibly change the dephasing results shown below. The value of δt and $\delta\phi$ are unique for a specific set of $h_{1,2}$, i.e. for a given accretion disk effect. This *alignment* procedure has been shown to be equivalent to maximizing the fitting factor over time and phase of coalescence in a matched filtering calculation with white noise [165].

Figure 6 shows the dominant dephasing (left-panel) and fractional amplitude difference (right-panel) after such alignment. As before, we plot these quantities for the dominant GW mode as a function of time in units of months, using different color curves for different accretion disk effects and different curve styles for different types of disks. Observe that after alignment, the dephas-

ing increases much less rapidly than in the previous case. This implies that the loss of overlap will also grow much more slowly. Dephasings after alignment thus correspond to the least difference between vacuum and non-vacuum waveform phases, without maximizing over intrinsic EOB parameters (such as the SMBH's and CO's mass) or other extrinsic parameters (such as those associated with the observation angles, detector motion, etc.).

Figure 6 confirms that certain accretion disk effects become significant very early during a LISA observation. As discussed in Sec. II B, a rough measure of whether the dephasing is “distinguishable” for an event with SNR ~ 10 is whether $\delta\phi_{\text{GW}} \gtrsim 1 \text{ rad}$ (see Sec. X B for a more accurate measure). The imprint of migration becomes almost immediately distinguishable for Sys. I and β -disks, while it takes at least one full year of observation before one can observe the same type of migration for Sys. II or BHL accretion for Sys. I. Wind effects also become important within one year of observation but for β -disks only.

Whether an effect is distinguishable is naturally sensitive to the EMRI parameters and orbital radii. Indeed, the bottom panel of Figure 6, corresponding to System-II, shows that in this case most effects are much smaller. This is mainly due to the assumption that System II's orbit is much closer to the SMBH where disk effects are less relevant. The bottom panel further suggests that BHL and azimuthal wind effects might be barely distinguishable after 1 year for β -disks only. Notice that all of these findings are consistent with the Newtonian estimates and figures presented in the previous sections.

The right panel of Figure 6 shows the fractional amplitude difference between the dominant mode of vacuum and non-vacuum waveforms after the alignment procedure described above. The amplitude difference follows closely the trend of the dephasing: Type-II migration is clearly visible in amplitude changes, while other effects are greatly suppressed. The amplitude difference plays an important role in the calculation of the overlap and the SNR of the difference that we show below.

B. Overlap Analysis

Dephasing studies are convenient as rough measure of distinguishability for a fixed SNR. However, the SNR changes during the GW observation, as signal accumulates and its frequency enters the detector's more sensitive domain. A more accurate measure of the detection significance of the particular disk effect in the data stream is the SNR of the waveform *difference* between the data streams with and without the effect, and the so called overlap/mismatch. In Sec. II B, we defined all these quantities in terms of cross-correlation integrals weighted by the spectral noise of the LISA detector. Note that these quantities account for the difference in both the phase and amplitude evolution of the GW signal.

Figure 7 shows the SNR of the difference $\rho(\delta h)$ in the

$(\ell, m) = (2, 2)$ GW harmonic after minimization over time and phase shift in units of months. As before, different curve styles and colors correspond to different accretion disk models and effects, as defined in Fig. 1. The thick horizontal line corresponds to an SNR of 10, just about the threshold for detection. The numbers at the top of this figure show how the vacuum waveform SNR builds up as a function of observation time. This figure confirms that β -disk migration is the dominant perturbation to the measured GW signal and suggests that it is distinguishable within 4 months of observation. Migration is followed in significance by BHL accretion (for either α or β -disks) and β -disk azimuthal winds. These effects become distinguishable only after a full year of observation. All other accretion disk effects are insignificant within a 1 year evolution for System I. For System II, only β -disk BHL accretion and azimuthal disks are significant and only after 1 year of observation. Other effects may become significant for binaries that are closer to Earth than 1 Gpc, or if the observation is longer, or if the binary orientation relative to the detector is better than average.

This figure is a more realistic estimate of distinguishability than the dephasing study presented in the previous section. The increase in realism comes at the cost of a small drop in distinguishability; e.g. although Fig. 7 suggests that BHL accretion might be measurable after a 1 year observation, this is only marginal in the figures above. Such a drop is mostly due to the inclusion of detector noise in this subsection. Measurability of accretion disk effect would of course improve if the source is closer to Earth, such that the SNR of the signal is larger. Irrespective of this, all calculations suggest that Type II migration is such a strong effect that it is likely to be measurable with LISA.

C. Degeneracies

Degeneracies between EMRI system parameters, such as the SMBH and CO's mass, and accretion disk parameters could deteriorate the extraction of accretion disk parameters from EMRI GW observations. If one were to maximize the overlap function over all parameters (instead of just a time and phase offset, as done in the previous section), one might find mismatches much closer to zero, at the cost of biasing parameter extraction. In this subsection, we investigate this issue and the spectral signature left by disk-induced effects.

The effect of possible degeneracies can be assessed by investigating the Fourier transform of the GW response function, as this is the main ingredient in matched filtering. We restrict our study of degeneracies to a simple analytical estimate of the Fourier transform using the Newtonian stationary phase approximation (SPA) (see e.g. [170, 171]). First, let us review this approximation in vacuum GR, and then consider the modifications introduced by leading-order disk effects.

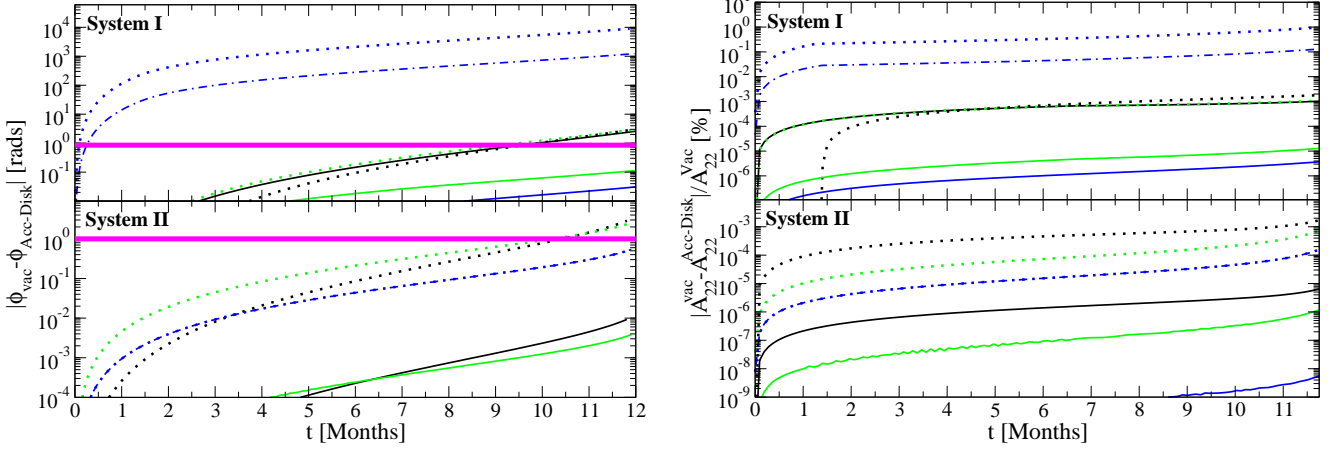


FIG. 6. Aligned dephasing (left) and aligned fractional amplitude difference (right) as a function of time in units of months for the dominant GW mode. Line style and color follow the same notation as in Fig. 5. The thick solid lines signal a 1 radian dephasing. The top and bottom panels correspond to System I and II respectively. Observe that the minimized dephasing exceeds unity in a short observation time for β -disk migration and System I, while for System II, only BHL accretion and β -disk wind effects do so after a full-year of observation.

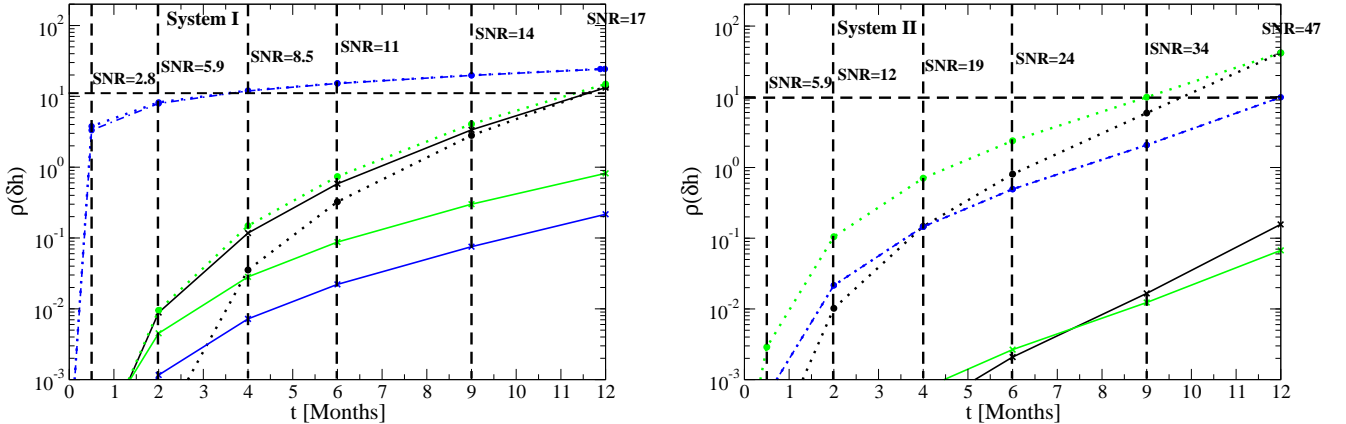


FIG. 7. SNR of the aligned, dominant waveform difference as a function of time in units of months. The left panel corresponds to System I and the right one to System II. Different curve colors and styles correspond to different disk effects and disk models, respectively, as in Fig. 5. The thick horizontal dashed line correspond to an SNR of 10. Observe that the SNR of the difference exceeds the SNR threshold in four months for β disk migration and Sys. I, while it take a full year of observation for the same to occur when modeling BHL accretion and β -disk wind effects.

The Fourier transform of the response function $h(t) = A(t)e^{i\phi_{\text{GW}}(t)}$ as

$$\tilde{h}(f) \equiv \int_{-\infty}^{\infty} h(t)e^{2\pi ift} dt. \quad (124)$$

This generalized Fourier integral can be solved via the method of steepest descent, assuming the amplitude changes slowly relative to the phase and noting that the complex phase $\psi = 2\pi ft - \phi_{\text{GW}}$ has a stationary point at $d\psi(f, t_0)/dt = 2\pi f - d\phi_{\text{GW}}(t_0)/dt = 0$. In this approximation, the Fourier transform becomes (see e.g. Eq. (4.5)

$$\tilde{h}(f) = \frac{8}{5} \frac{A(f)}{2} \sqrt{\frac{1}{2F}} e^{i(2\pi ft_0 - \phi_0)}, \quad (125)$$

where the factor of $8/5$ accounts for sky-averaging over beam pattern functions. The quantities $[t_0, \psi(f, t_0), \dot{\psi}(f, t_0)]$ for a fixed f can be found by assuming that the phase and time of merger are fixed

(t_c, ϕ_c) :

$$t_0 - t_c = \int_0^{\Omega_0} \frac{dE}{d\Omega'} \left(\frac{dE}{dt} \right)^{-1} d\Omega' = \int_0^{\bar{r}_0} \frac{d\bar{r}}{\dot{r}}, \quad (126)$$

$$\phi_0 - \phi_c = \int_0^{\Omega_0} \frac{dE}{d\Omega'} \left(\frac{dE}{dt} \right)^{-1} \Omega' d\Omega' = 2 \int_0^{\bar{r}_0} \Omega \frac{d\bar{r}}{\dot{r}}, \quad (127)$$

where $\Omega_0 \equiv f/2$ is the stationary point and $\bar{r}_0 \equiv \bar{r}(f/2)$. The quantity \dot{r} can be constructed from $(dE/d\bar{r})^{-1} E$ and $\dot{E} = \mathcal{F}_{\text{GW}}(\bar{r}, \Omega)$ is the GW energy loss rate, given in Eqs. (1,5) in the Newtonian approximation or Eqs. (118,119) in the EOB approximation, if we neglect accretion disk effects.

Neglecting disk effects, we can readily evaluate each of these terms to leading (Newtonian) order. Using that the orbital frequency is given by Eq. (2) and the rate of change of the orbital separation by Eq. (8), Eq. (126) becomes $t_0 = t_c - (5/256)\mathcal{M}u^{-8/3}$, while Eq. (127) becomes $\phi(t_0) = \phi_c - (1/16)u^{-5/3}$, where we have defined the reduced frequency $u \equiv \pi\mathcal{M}f$, with the chirp mass $\mathcal{M} = q^{3/5}M_\bullet$ and $q \equiv m_\star/M_\bullet$ the mass-ratio. Using the Newtonian expressions for $A(t) = \mathcal{M}/D_L(\mathcal{M}\Omega)^{2/3}$ (see e.g. Eq.(3.5) in [171]), the sky-averaged Fourier amplitude becomes

$$|\tilde{h}|_{\text{vac}} = \frac{\mathcal{M}^{5/6}}{\pi^{2/3}\sqrt{30} D_L} f^{-7/6}. \quad (128)$$

where D_L is the luminosity distance of the source and f is the observed GW frequency, while the Fourier phase is

$$\psi_{\text{vac}}(t_0, f) = 2\pi f t_0 - \phi(f) = \frac{3}{128} u^{-5/3} + \text{const}, \quad (129)$$

Let us now repeat this calculation with accretion disk modifications. We modify the above algorithm by replacing $\dot{E} = \dot{E}_{\text{vac}}(1 + \delta\ell/\dot{\ell}_{\text{GW}})$, where $\delta\ell$ is given by Eqs. (106), (108) or (110) for Type I, II-SC and II-IPP migration respectively, or Eq. (80) for azimuthal winds. We replaced m_\star by Eq. (71) when modeling unquenched, BHL accretion. The resulting frequency-domain phase and amplitude can be parameterized as

$$\psi/\psi_{\text{vac}} = 1 - \tilde{A}_1 \alpha_1^{c_1} \dot{m}_{\bullet 1}^{c_2} M_{\bullet 5}^{\tilde{a}_3} q_0^{\tilde{a}_4} u_0^{\tilde{a}_5}, \quad (130)$$

and

$$|\tilde{h}|/|\tilde{h}|_{\text{vac}} = 1 - \tilde{B}_1 \alpha_1^{c_1} \dot{m}_{\bullet 1}^{c_2} M_{\bullet 5}^{\tilde{a}_3} q_0^{\tilde{a}_4} u_0^{\tilde{a}_5}, \quad (131)$$

where $q_0 \equiv q/10^{-4}$ is the normalized mass-ratio $q = M_\bullet/m_\star$ and $u_0 \equiv (\pi\mathcal{M}f)/(6.15 \times 10^{-5})$ is a normalized reduced frequency and a GW frequency of 10^{-2} Hz. The parameters $(\tilde{A}_1, \tilde{B}_1, \tilde{a}_i)$ are given in Table III, while notice that (c_1, c_2) are the same as those in Table II. Note that the expressions in Eqs. (130) and (131) are valid only in the regime of frequency space where the accretion disk effects are small perturbations away from the vacuum evolution (ie. at sufficiently small separations).

		\tilde{A}_1	\tilde{B}_1	\tilde{a}_3	\tilde{a}_4	\tilde{a}_5
BHL	α	3 (-8)	2 (-7)	1	4	-20/3
BHL	β	1 (-5)	1 (-4)	6/5	79/25	-79/15
W	α	6 (-17)	1 (-16)	1	16/5	-16/3
W	β	6 (-12)	4 (-11)	6/5	59/25	-59/15
M1	α	3 (-10)	4 (-9)	1	16/5	-16/3
M1	β	1 (-6)	3 (-6)	6/5	59/25	-59/15
M2	α_{SC}	8 (-6)	2 (-5)	1	-2/5	-8/3
M2	β_{SC}	6 (-3)	2 (-2)	1/4	-1/8	-25/12
M2	β_{IPP}	6 (-4)	2 (-3)	4/7	-17/70	-7/3

TABLE III. Columns are parameters in Eq. (130) and rows are migration effects. As in Table I, the notation $x(y) = x \times 10^y$ in radians for \tilde{A}_1 and dimensionless for \tilde{B}_1 . Observe that the frequency exponent $\tilde{a}_5 < 0$, implying that these accretion disk effects are dominant at small frequencies (large radii).

Let us discuss these results further. First, notice that corrections to $\psi(t_0, f)$ due to Type II migration are orders of magnitude larger than all other effects, as shown by the magnitude of \tilde{A}_1 . Second, notice that all disk-induced corrections depend on *negative* powers of frequency (or reduced frequency u in this case). This is because such accretion disk corrections are largest for large radii, equivalent to weak-field GR effects. In fact, they are dominant over the leading-order vacuum term (the factor of $u^{-5/3}$ in ψ_{vac}) at low frequency. This suggests that migration effects are not strongly correlated with GR vacuum terms in the PN approximation²³, as the latter depend on positive powers of u relative to $u^{-5/3}$.

One might wonder how the accretion disk effects modify the Fourier phase and amplitude when they are not necessary a small perturbation away from the vacuum evolution. In general, the accretion disk correction changes the functional form of the phase or amplitude as follows:

$$y_{\text{vac}} \rightarrow \frac{y_{\text{vac}}}{1 + \Delta \alpha_1^{\tilde{a}_1} \dot{m}_{\bullet 1}^{\tilde{a}_2} M_{\bullet 5}^{\tilde{a}_3} q_0^{\tilde{a}_4} u_0^{\tilde{a}_5}} \quad (132)$$

where $y_{\text{vac}} = (\psi, |\tilde{h}|)$ when $\Delta = (\tilde{A}_1, \tilde{B}_1)$. This means that, unlike what Eqs. (130) and (131) suggest, the accretion disk effects always *suppress* the vacuum evolution as $\Delta > 0$. Figure 8 shows the absolute value squared of the Fourier amplitudes as a function of frequency for an EMRI with $M_\bullet = 10^5 M_\odot$ and $m_\star = 10 M_\odot$ and different accretion disk effects (neglecting all quenching). For comparison, we also plot the vacuum amplitude and the spectral noise density curve. Observe that below $f \lesssim 10^{-3}$ Hz, accretion disk induced migration becomes dominant over GW emission, and the Fourier amplitude

²³ However, the detected signal is also modulated during LISA's orbit around the Sun which we neglect in this paper. This can introduce correlations between parameters that change the GW phase slowly, such as migration effects, source direction, and orientation angles [172].

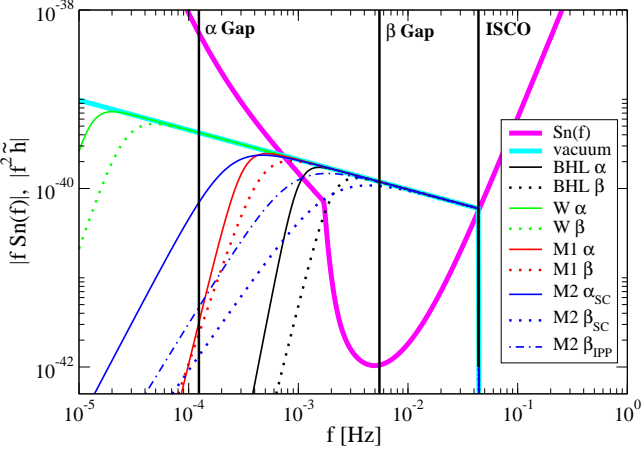


FIG. 8. Absolute value squared of the Fourier amplitudes with different accretion disk effects (see label) as a function of frequency in units of Hertz. We also plot this amplitude in vacuum and LISA’s spectral noise density. Vertical lines from right to left correspond to the ISCO frequency, the frequency at which a gap forms for β -disks and for α -disks.

is significantly different. This effect was also demonstrated to decrease the GW background for pulsar timing arrays [148]. A gap is expected to be opened at small frequencies, but to close at the radii indicated with vertical lines (see Sec. III B). At these frequencies Type-II migration transitions to Type-I. Coincidentally, hydrodynamic drag due to an azimuthal wind and BHL accretion cease at smaller frequencies.

The precise accuracies to which disk parameters can be estimated is difficult to ascertain. A crude Fisher analysis that neglects degeneracies (a diagonal approximation) suggests extraction accuracies of up to 1%. We expect, however, that correlations will deteriorate the accuracy of extraction down to 10% [76]. Ultimately, a proper assessment of the accuracy to which disk parameters could be extracted from EMRI observations would require the detailed mapping of the likelihood surface with relativistic EMRI signals, full Fourier transforms, and improved disk modeling (including relativistic effects and magnetic fields). This, however, is beyond the scope of this paper.

XI. DISCUSSION

We have explored the effect of accretion disks on the GWs emitted during the inspiral of a small BH into a much more massive one. We have found that disk migration has the biggest influence on the EMRI dynamics. If EMRIs are detected with LISA, our study suggests that migration could be measurable within 4 months of observation for a β -disk. Depending on the particular EMRI considered, a gap could open in the accretion disk, leaving an imprint in the GW observable. We have studied possible degeneracies between accretion disk and EMRI parameters and found that they are weakly correlated.

This is because disk effects are dominant at large separations, thus introducing “negative” PN terms in the frequency-domain waveform phase. The LISA detection of a GW from an EMRI embedded in an accretion disk could therefore allow us to measure a combination of the α and \dot{m}_\bullet parameters of the disk.

The prospect of probing accretion disks with GWs can be improved in the presence of an EM counterpart. If the EM luminosity of the SMBH’s accretion disk is observed, one might be able to separately measure both α and \dot{m}_\bullet by adding the information from a GW detection. If the GW detection does not show evidence of accretion disk effects but an EM signal is present, then one might be able to distinguish between α and β -disks.

Several caveats should be kept in mind about elements of our analysis that could be improved on in the future. First, we have considered a very specific type of EMRI, consisting of quasi-circular orbits on the equatorial plane. In principle, the CO could be in an inclined and eccentric orbit. If so, certain accretion disk effects that were negligible in our analysis, such as the self-gravity of the disk, could become more important. Such effects would induce additional apsidal and nodal precession, which could leave a detectable signature on both the EM and GW signals.

Another important caveat is that we did not explore possible degeneracies with other EMRI parameters, like source direction. It is possible that the orbital modulation of LISA can induces a time dependence mimicing the effects of accretion disks. However, since these modulations are periodic, we expect no strong degeneracies after a multi-year observation.

Another important issue involves the accuracy of the EMRI model used. Although recently an EOB-inspired EMRI waveform model was developed [73–75], no such model has been thoroughly tested for generic EMRIs. Even in the case of quasi-circular inspirals on the equatorial plane, the EOB model is still only accurate up to dephasings of order 10 radians. This implies that accretion disk effects associated with dephasing signatures of this magnitude, such as the effect of BHL accretion, might be difficult to disentangle. However, accretion disk effects are also important at large separations, whereas mismodeling errors are of concern only close to the ISCO. Thus, the detection of EMRIs at moderate binary separations might allow the extraction of small accretion disk effects. Moreover, the effects of migration are much larger than any possible waveform mismodeling and so they can be easily isolated. Ultimately, a more detailed Markov-Chain Monte-Carlo study is required to determine the accuracy to which disk effects can be measured.

Finally, let us highlight the large uncertainty that currently exists in accretion disk modeling. Even when considering radiatively efficient thin Newtonian disks, there are several viable models, here parametrized as α and β -disks, that can have drastically different effects on EMRI inspirals. Unfortunately, these Newtonian models are expected to be highly inaccurate precisely in the regime

where EMRIs are most easily seen, i.e. in the relativistic regime close to the SMBH. A natural extension of this work would be to consider EMRIs in the context of relativistic accretion disks [101, 102], for example through the inclusion of relativistic BHL accretion [38] and migration [143, 144].

ACKNOWLEDGMENTS

We are grateful to Cole Miller, Ramesh Narayan, Shane Davis, Scott Hughes, and Zoltán Haiman for useful comments and suggestions. BK and NY acknowledge support from the NASA through Einstein Postdoctoral Fellowship Award Number PF9-00063 and PF0-110080 issued by the Chandra X-ray Observatory Center, which is operated by the Smithsonian Astrophysical Observatory for and on behalf of the National Aeronautics Space Administration under contract NAS8-03060. BK acknowledges partial support by OTKA grant 68228. AL acknowledges support from NSF grant AST-0907890 and NASA grants NNX08AL43G and NNA09DB30A.

Appendix A: Phase Correction due to CO Accretion

Let us compute here the GW phase evolution when the CO's mass is varying due to BHL accretion. The GW phase is given by the first line of Eq. (14).

$$\phi_{\text{GW}} = 2 \int_{\bar{r}_{0'}}^{\bar{r}_f} \Omega(\bar{r}) \frac{d\bar{r}}{\dot{\bar{r}}} = -\frac{5}{32} M_{\bullet} \int_{\bar{r}_{0'}}^{\bar{r}_f} \frac{\bar{r}^{3/2}}{m_{\star}(\bar{r})} d\bar{r}. \quad (\text{A1})$$

Two important corrections are induced by the CO's variable mass: a change in the limits of integration $\bar{r}_0 \rightarrow \bar{r}_{0'}$ and a change in the denominator of the integrand in the phase evolution, $m_{\star} \rightarrow m_{\star}(t)$. We expand both in a Taylor series around \bar{r}_0 and the initial CO mass $m_{\star,0}$ at $\bar{r} = \bar{r}_{0'}$. We evaluate the change in the total GW phase induced by accretion while keeping \bar{r}_f , the observation time $T = t_f - t_0$, and $m_{\star,0}$ fixed.

The limits of integration can be computed by integrating the radial inspiral evolution equation (8) with the time dependent $m_{\star}(t)$,

$$\bar{r}_f^4 - \bar{r}_{0'}^4 = -\frac{256}{5} \frac{1}{M_{\bullet}^2} \int_{t_{0'}}^{t_f} m_{\star}(t) dt. \quad (\text{A2})$$

where

$$m_{\star}(t) = m_{\star,0} + \int_{t_{0'}}^t \dot{m}_{\star}(t') dt'. \quad (\text{A3})$$

Note that $\dot{m}_{\star} \equiv \dot{m}_{\star}(\bar{r})$ given by Eqs. (54,70). Changing integration variable from t to \bar{r} using $dt = d\bar{r}/\dot{\bar{r}}$ using Eq. (8) for $\dot{\bar{r}}(\bar{r})$, we get

$$\int_{t_0'}^{t_f} m_{\star}(t) dt = m_{\star,0} \left(T + \frac{25}{4096} \frac{M_{\bullet}^4}{m_{\star,0}^2} \langle \delta m_{\star} \rangle_{3,3} \right), \quad (\text{A4})$$

where²⁴

$$\langle \delta m_{\star} \rangle_{A,B} \equiv \int_{\bar{r}_f}^{\bar{r}_0} d\bar{r} \bar{r}^A \int_{\bar{r}}^{\bar{r}_0} d\bar{r}' \bar{r}'^B \frac{\dot{m}_{\star}(\bar{r}')}{m_{\star,0}}. \quad (\text{A5})$$

Substituting in Eq. (A2), the initial separation becomes

$$\bar{r}_{0'}^{\dot{m}} = \bar{r}_f \left[1 + \frac{\tau_{\text{SPA}}}{\bar{r}_f^4} \left(1 + \frac{25}{4096} \frac{M_{\bullet}^4}{m_{\star,0}^2 T} \langle \delta m_{\star} \rangle_{3,3} \right) \right]^{1/4}. \quad (\text{A6})$$

where τ_{SPA} is the dimensionless observation time given by Eq. (11), the \dot{m} index was introduced to distinguish from other modifications below, c.f. Eq. (11) for \bar{r}_0 . Thus, the change in the lower integration bound in Eq. (A1) is

$$\delta \bar{r}_{0'}^{\dot{m}} = \bar{r}_{0'}^{\dot{m}} - \bar{r}_0 \approx \frac{5}{64} \frac{M_{\bullet}^2}{m_{\star,0} \bar{r}_0^3} \langle \delta m_{\star} \rangle_{3,3}. \quad (\text{A7})$$

Since the total relative change in m_{\star} is very small during the observation, we may approximate $1/m_{\star}(t)$ in Eq. (A1) as

$$\frac{1}{m_{\star}(t)} = \frac{1}{m_{\star,0} + \int_{t_0}^t \dot{m}_{\star}(t') dt'} \approx \frac{1}{m_{\star,0}} - \frac{1}{m_{\star,0}^2} \int_{t_0}^t \dot{m}_{\star}(t') dt' \quad (\text{A8})$$

so that Eq. (A1) becomes

$$\begin{aligned} \phi_{\text{GW}}^{\dot{m}_{\star}} &\approx -\frac{5}{32} M_{\bullet} \int_{\bar{r}_{0'}}^{\bar{r}_f} d\bar{r} \frac{\bar{r}^{3/2}}{m_{\star,0}} \left[1 - \int_{t(\bar{r}_{0'})}^{t(\bar{r})} dt' \frac{\dot{m}_{\star}(t')}{m_{\star,0}} \right] \\ &= \frac{1}{16} \frac{M_{\bullet}}{m_{\star,0}} \left(\bar{r}_{0'}^{5/2} - \bar{r}_f^{5/2} \right) - \frac{25}{2048} \frac{M_{\bullet}^3}{m_{\star,0}^2} \langle \delta m_{\star} \rangle_{3/2,3}, \end{aligned} \quad (\text{A9})$$

where the \dot{m}_{\star} label denotes that the CO is accreting, in the second line we have changed integration variables using $dt' = d\bar{r}'/\dot{\bar{r}'}$ and used Eq. (A5).

Relative to the GW phase without accretion,

$$\begin{aligned} \delta \phi_{\text{GW}}^{\dot{m}_{\star}} &= \frac{5}{32} \frac{M_{\bullet}}{m_{\star,0}} \bar{r}_0^{3/2} \delta \bar{r}_{0'}^{\dot{m}} - \frac{25}{2048} \frac{M_{\bullet}^3}{m_{\star,0}^2} \langle \delta m_{\star} \rangle_{3/2,3} \\ &\approx \frac{25}{2048} \frac{M_{\bullet}^3}{m_{\star,0}^2} \left(\frac{\langle \delta m_{\star} \rangle_{3,3}}{\bar{r}_0^{3/2}} - \langle \delta m_{\star} \rangle_{3/2,3} \right). \end{aligned} \quad (\text{A10})$$

Equation (A10) and (A5) can be used to calculate the GW phase shift for arbitrary \dot{m}_{\star} . In the next two subsections we consider BHL accretion $\dot{m}_{\star}^{\text{B}}$ and gas supply limited BHL accretion $\dot{m}_{\star} = \dot{M}_{\bullet}$.

1. Unsaturated BHL accretion

First consider the case where BHL accretion is not limited by the amount of local gas supply, $\dot{m}_{\star}^{\text{B}}(r) \leq \dot{M}_{\bullet}$.

²⁴ Since $\langle \delta m_{\star} \rangle_{A,B} \ll m_{\star,0} T$, we approximate the lower integration bounds in Eq. (A5) with \bar{r}_0 .

BHL accretion is not quenched by local gas supply if the observation is limited to orbital radii $\bar{r} \leq \bar{r}_q$, or equivalently, if the dimensionless accretion rate onto the SMBH $\dot{m}_\bullet \geq \dot{m}_{\bullet,q}$. In practice, this is the case during a year of observation approaching ISCO, if the SMBH accretion rate is moderate to high $\dot{m}_\bullet \gtrsim 0.3$ or if the mass-ratio is very small $m_\star/M_\bullet \lesssim 10^{-6}$ [see Eq. (64)].

Substituting the BHL accretion rate, Eqs. (54,A5) for α and β -disks into Eq. (A10) yields

$$\delta\phi_{\text{GW}}^{\alpha,\text{B}} = -0.733 \alpha_1^{-1} \frac{M_{\bullet 5}^2}{\dot{m}_{\bullet 1}^5 m_{\star 1}} \bar{r}_{0,20}^{25/2} \left(1 - \frac{280}{99} x^{5/2} + \frac{175}{99} x^4 + \frac{56}{99} x^{25/2} - \frac{50}{99} x^{14} \right), \quad (\text{A11})$$

$$\delta\phi_{\text{GW}}^{\beta,\text{B}} = -495 \alpha_1^{-4/5} \frac{M_{\bullet 5}^{11/5}}{\dot{m}_{\bullet 1}^{17/5} m_{\star 1}} \bar{r}_{0,20}^{52/5} \left(1 - \frac{6188}{2133} x^{5/2} + \frac{7735}{4266} x^4 + \frac{2975}{4266} x^{52/5} - \frac{1300}{2133} x^{119/10} \right), \quad (\text{A12})$$

where $m_{\star 1}$ refers to the initial CO mass at \bar{r}_0 , $x = \bar{r}_f/\bar{r}_0$, $\bar{r}_0 \equiv \bar{r}_0(\bar{r}_f, T)$ is given by Eq. (11), and $\bar{r}_{0,20} = \bar{r}_0/20$. The phase evolution given by Eq. (A11–A12) depends on only two sets of parameters: the time-independent coefficient preceding the parentheses, and the time dependent quantity τ/\bar{r}_f^4 . The later also appears in the standard inspiral phase expression, Eq. (14), which we used to distinguish two cases: when the observation time is long or short relative to the inspiral timescale at the given radius [see Eqs. (15–16)].

We can similarly distinguish here between two asymptotic cases. For long observations ($T \gg T_{\text{crit}}$) or small separations ($\bar{r}_f \ll \bar{r}_{f,\text{crit}}$), $\bar{r}_0 \approx \tau^{1/4}$, $x \approx \bar{r}_f/\tau^{1/4} \ll 1$, we can approximate the dephasing with the general formula

$$\delta\phi_{\text{GW},\text{long}} = -C_1 \alpha_1^{-c_1} \dot{m}_{\bullet 1}^{-c_2} \frac{m_{\star n}^{c_3}}{M_{\bullet 5}^{c_4}} T_{\text{yr}}^{c_5} \left(1 - C_2 \frac{M_{\bullet 5}^{2c_6}}{m_{\star 1}^{c_6}} \frac{\bar{r}_{f,10}^{4c_6}}{T_{\text{yr}}^{c_6}} \right) \quad (\text{A13})$$

where the coefficients (C_i, c_j) are given by the first two rows of Table II and $n = 2$ for Type II migration, while $n = 1$ for all other migration disk effects. For short observations ($T \ll T_{\text{crit}}$) or small separations ($\bar{r}_f \gg \bar{r}_{f,\text{crit}}$), $\tau/\bar{r}_f^4 \ll 1$, $\bar{r}_0 \approx \bar{r}_f + \tau/(4\bar{r}_f^3)$, $x \approx 1 - \tau/(4\bar{r}_f^4)$, and we can approximate the dephasing with the general formula

$$\delta\phi_{\text{GW},\text{short}} = -\frac{D_1}{\alpha_1^{c_1} \dot{m}_{\bullet 1}^{c_2} M_{\bullet 5}^{d_2}} \frac{m_{\star n}^{d_1}}{T_{\text{yr}}^{d_3} \bar{r}_{f,10}^{d_4}} \left(1 - D_2 \frac{m_{\star 1}}{M_{\bullet 5}^2} \frac{T_{\text{yr}}}{\bar{r}_{f,10}^4} \right) \quad (\text{A14})$$

where the coefficients (D_i, d_j) are given by the first two rows of Table II and $n = 2$ for Type II migration, while $n = 1$ for all other migration disk effects.

2. Gas supply limited BHL accretion

If $\dot{m}_\star^{\text{B}}(\bar{r}) \geq \dot{M}_\bullet$, the accretion onto the CO is limited by the amount of local gas supply. This is the case outside $\bar{r} \geq \bar{r}_q$, or if the SMBH accretion rate satisfies $\dot{m}_\bullet \geq \dot{m}_{\bullet,q}$, see Eq. (64) for $(\bar{r}_q, \dot{m}_{\bullet,q})$. In practice, this is the case for $\dot{m}_\bullet \lesssim 0.1$ for beta disks if the final orbital radius is not very close to the ISCO (e.g. $\bar{r}_f \gtrsim 10$). For larger \dot{m}_\bullet accretion rates approaching the ISCO or intermediate mass-ratio inspirals, BHL accretion starts supply limited and becomes unsaturated near the ISCO.

Assuming $\dot{m}_\star = \dot{M}_\bullet$ in Eqs. (A5,A10), we get

$$\delta\phi_{\text{GW}}^{\text{sup. BHL}} \approx -4.2 \frac{\dot{m}_{\bullet 1} M_{\bullet 5}^4}{m_{\star 1}^3} \bar{r}_{0,20}^{13/2} \left(1 - \frac{208}{63} x^{5/2} + \frac{130}{63} x^4 + \frac{80}{63} x^{13/2} - \frac{65}{63} x^8 \right) \quad (\text{A15})$$

for both α and β -disks, where again $\bar{r}_0 \equiv \bar{r}_0(\bar{r}_f, T)$ given by Eq. (11) and $x = \bar{r}_f/\bar{r}_0$. Relative to the BHL accretion case with unlimited gas supply Eq. (A11–A12), the phase is a less steep function of radius. The evolution is again determined by two combination of parameters, the constant coefficient (which is now different) and the time dependent quantity τ/\bar{r}_f^4 .

In the two limiting cases, where the observation is long or short relative to the inspiral timescale, we again can parameterize the dephasing as in Eq. (A13) and (A14) respectively, where the coefficients (C_i, c_j) and (D_i, d_j) are given by the third row of Table II.

Appendix B: Phase Correction due to Wind and Migration

In this appendix we derive the correction to the GW phase due to a modification in angular momentum dissipation. The result of a similar, but more general, angular momentum dissipation rate $\delta\ell/\ell_{\text{GW}} = Ar^B$ is presented in Paper I [50]. We focus on quasi-circular orbits only. From Eq. (14),

$$\begin{aligned} \phi_{\text{GW}} &= 2 \int_{\bar{r}_{0'}}^{\bar{r}_f} \Omega(\bar{r}) \frac{d\bar{r}}{\dot{\bar{r}}} = 2 \int_{\bar{r}_{0'}}^{\bar{r}_f} \Omega(\bar{r}) \left(\frac{d\ell}{dt} \right)^{-1} \left(\frac{d\ell}{d\bar{r}} \right) d\bar{r} \\ &= \int_{\bar{r}_{0'}}^{\bar{r}_f} \bar{r}^{-2} \frac{d\bar{r}}{\dot{\ell}(\bar{r})}, \end{aligned} \quad (\text{B1})$$

where we have expressed the GW phase as a function of radial and temporal derivatives of the specific angular momentum of the CO. Similar to Appendix A, we calculate the total total change in the GW phase relative to the unperturbed GW inspiral phase, by keeping the final separation \bar{r}_f and the observation time T fixed. Relative to the vacuum inspiral Eq. (14), a modified angular momentum dissipation causes a phase shift by changing the lower integration bound and $\dot{\ell}$ in Eq. (B1). Since the additional specific angular momentum loss $\delta\dot{\ell}$ is small rela-

tive to $\dot{\ell}_{\text{GW}}$, we may approximate the result by expanding in a series in the small quantity $\delta\dot{\ell}/\dot{\ell}_{\text{GW}}$.

First to estimate $\bar{r}_{0'}$, note that the accelerated dissipation of angular momentum causes an accelerated inspiral rate. For circular orbits, $\ell = M_{\bullet}\bar{r}^{1/2}$, $E = M_{\star}/(2\bar{r})$, so that

$$\dot{\bar{r}} = \frac{2\bar{r}^{1/2}}{M_{\bullet}}\dot{\ell} = -\frac{64}{5}\frac{m_{\star}}{M_{\bullet}^2}\bar{r}^{-3}\left(1 + \frac{\delta\dot{\ell}}{\dot{\ell}_{\text{GW}}}\right). \quad (\text{B2})$$

This equation can be integrated to give

$$\bar{r}_{0'}^{\dot{\ell}} = \bar{r}_f \left[1 + \frac{\tau}{\bar{r}_f^4} \left(1 + \frac{4}{\tau} \langle \delta\ell \rangle_3\right)\right]^{1/4}. \quad (\text{B3})$$

where we have introduce the index $\dot{\ell}$ to distinguish from other effects, and we define²⁵

$$\langle \delta\ell \rangle_A \equiv \int_{\bar{r}_f}^{\bar{r}_0} d\bar{r} \bar{r}^A \left(\frac{\delta\dot{\ell}}{\dot{\ell}_{\text{GW}}}\right) d\bar{r}'. \quad (\text{B4})$$

Comparing to Eq. (11), the change in the lower integration bound

$$\delta\bar{r}_{0'}^{\dot{\ell}} = \bar{r}_{0'}^{\dot{\ell}} - \bar{r}_0 \approx \frac{\langle \delta\ell \rangle_3}{\bar{r}_0^3} \quad (\text{B5})$$

Now using

$$\frac{1}{\dot{\ell}} = \frac{1}{\dot{\ell}_{\text{GW}} + \delta\dot{\ell}} \approx \frac{1}{\dot{\ell}_{\text{GW}}} \left(1 - \frac{\delta\dot{\ell}}{\dot{\ell}_{\text{GW}}}\right) \quad (\text{B6})$$

for the integrand in Eq. (B1), the GW phase is

$$\begin{aligned} \phi_{\text{GW}}^{\dot{\ell}} &\approx \frac{5}{32} \frac{M_{\bullet}}{m_{\star}} \int_{\bar{r}_f}^{\bar{r}_{0'}} d\bar{r} \bar{r}^{3/2} \left(1 - \frac{\delta\dot{\ell}}{\dot{\ell}_{\text{GW}}}\right) \\ &= \frac{5}{32} \frac{M_{\bullet}}{m_{\star}} \left[\frac{2}{5} \left(\bar{r}_{0'}^{5/2} - \bar{r}_f^{5/2} \right) - \langle \delta\ell \rangle_{3/2} \right] \end{aligned} \quad (\text{B7})$$

so that relative to the vacuum inspiral phase

$$\begin{aligned} \delta\phi_{\text{GW}}^{\dot{\ell}} &\approx \frac{5}{32} \frac{M_{\bullet}}{m_{\star}} \left(\bar{r}_0^{3/2} \delta\bar{r}_{0'}^{\dot{\ell}} - \langle \delta\ell \rangle_{3/2} \right) \\ &= \frac{5}{32} \frac{M_{\bullet}}{m_{\star}} \left(\frac{\langle \delta\ell \rangle_3}{\bar{r}_0^{3/2}} - \langle \delta\ell \rangle_{3/2} \right). \end{aligned} \quad (\text{B8})$$

Equations (B8) and (B4) are the analogues of Eqs (A10) and (A5) for the GW phase shift caused by an additional source of angular momentum dissipation $\delta\dot{\ell}$. In the next three subsections we consider the azimuthal wind, Type-I migration, and Type-II migration. In these cases $\delta\dot{\ell}/\dot{\ell}_{\text{GW}} = Ar^B$ where A and B are constants, so the integral in Eq. (B4) can be evaluated analytically.

1. Wind – unsaturated BHL accretion

If the additional angular momentum dissipation is caused by an azimuthal wind where the accretion onto the CO is the unsaturated BHL rate, $\delta\dot{\ell}(\bar{r}) = \dot{\ell}_{\text{wind}}^{\text{B}}(\bar{r})$ given by Eq. (81). Substituting in Eqs. (B8) and (B4) we get

$$\begin{aligned} \delta\phi_{\text{GW}}^{\alpha, \text{Bw}} &\approx -5.2 \times 10^{-3} \alpha_1^{-1} \frac{M_{\bullet}^2}{\dot{m}_{\bullet 1}^3 m_{\star 1}} \bar{r}_{0,20}^{21/2} \\ &\quad \times \left(1 - 8x^{21/2} + 7x^{12}\right), \end{aligned} \quad (\text{B9})$$

$$\begin{aligned} \delta\phi_{\text{GW}}^{\beta, \text{Bw}} &\approx -10 \alpha_1^{-4/5} \frac{M_{\bullet}^{11/5}}{\dot{m}_{\bullet 1}^{7/5} m_{\star 1}} \bar{r}_{0,20}^{42/5} \\ &\quad \times \left(1 - \frac{33}{5}x^{42/5} + \frac{28}{5}x^{99/10}\right), \end{aligned} \quad (\text{B10})$$

where $x = \bar{r}_f/\bar{r}_0$ and $\bar{r}_0 \equiv \bar{r}_0(\bar{r}_f, T)$, see discussion following Eqs. (A12,A15). Following the derivation presented in Appendix A 1, we can expand in long and short observation times relative to the inspiral timescale to recover a dephasing as in Eq. (A13) and (A14) with the coefficients (C_i, c_j) and (D_i, d_j) given by the fourth and fifth rows of Table II.

2. Wind – quenched BHL accretion

If the additional angular momentum dissipation is caused by an azimuthal wind where the accretion onto the CO is limited by the amount of gas supply then we substitute $\delta\dot{\ell}(\bar{r}) = \dot{\ell}_{\text{wind}}^{\text{sup. BHL}}(\bar{r})$ Eq. (82) into Eq. (B8) to obtain the corresponding total GW phase shift

$$\delta\phi_{\text{GW}}^{\text{Bw}} = \begin{pmatrix} -0.065 \\ -0.16 \end{pmatrix} \frac{\dot{m}_{\bullet 1}^3 M_{\bullet}^4}{m_{\star 1}^3} \bar{r}_{0,20}^{9/2} \left(1 + 3x^6 - 4x^{9/2}\right), \quad (\text{B11})$$

where throughout this section the top and bottom rows correspond to α and β -disks, respectively, and the parameters $x \equiv x(\bar{r}_f, T)$ and $\bar{r}_0 \equiv \bar{r}_0(\bar{r}_f, T)$, see discussion following Eqs. (A12,A15). Notice that although we are here setting $\dot{m}_{\star} = \dot{M}_{\bullet}$, there is still a dependance on the type of accretion disk, due to the factor of γ in Eq. (80).

Again, as in Appendix A 1, we expand in long and short observation times to obtain the dephasing of Eqs. (A13) and (A14) with the coefficients (C_i, c_j) and (D_i, d_j) given by the sixth and seventh rows of Table II.

3. Type-I migration

Let us now compute the dephasing introduced by the angular momentum dissipation due to Type-I migration.

²⁵ Since $\dot{\ell}_{\text{wind}}/\dot{\ell}_{\text{GW}} \ll 1$, we approximate the lower integration bound with \bar{r}_0 in Eq. (B4).

Substituting Eqs. (106) into Eqs. (B8) and (B4) we get

$$\delta\phi_{\text{GW}}^{\alpha,\text{TI}} = -6.1 \times 10^{-4} \alpha_1^{-1} \frac{\dot{m}_{\bullet 1}^{-3} M_{\bullet 5}^2}{m_{\star 1}} \bar{r}_{0,20}^{21/2} \times \left(1 - 8x^{21/2} + 7x^{12}\right), \quad (\text{B12})$$

$$\delta\phi_{\text{GW}}^{\beta,\text{TI}} = -1.5 \alpha_1^{-4/5} \frac{\dot{m}_{\bullet 1}^{-7/5} M_{\bullet 5}^{11/5}}{m_{\star 1}} \bar{r}_{0,20}^{42/5} \times \left(1 - \frac{33}{5}x^{42/5} + \frac{28}{5}x^{99/10}\right). \quad (\text{B13})$$

where again $x \equiv x(\bar{r}_f, T)$ and $\bar{r}_0 \equiv \bar{r}_0(\bar{r}_f, T)$

We now take the two limiting cases of long and short observations. For long and short observations, we find dephasings as in Eq. (A13) and (A14) with coefficients (C_i, c_j) and (D_i, d_j) given by the eighth and ninth rows of Table II.

4. Type-II migration

Consider now the dephasing corresponding to the angular momentum dissipation due to Type-II migration. Substituting Eqs. (108) and (110) into Eqs. (B8) and (B4) we get

$$\delta\phi_{\text{GW}}^{\alpha,\text{TII,SC}} = -8 \times 10^{-3} \frac{\dot{m}_{\bullet 1} M_{\bullet 5}^4}{m_{\star 2}^3} \bar{r}_{0,20}^{13/2} \times \left(1 - \frac{16}{3}x^{13/2} + \frac{13}{3}x^8\right), \quad (\text{B14})$$

$$\delta\phi_{\text{GW}}^{\beta,\text{TII,SC}} = -22 \alpha_1^{1/2} \frac{\dot{m}_{\bullet 1}^{5/8} M_{\bullet 5}^{21/8}}{m_{\star 2}^{19/8}} \bar{r}_{0,20}^{45/8} \times \left(1 - \frac{19}{4}x^{45/8} + \frac{15}{4}x^{57/8}\right), \quad (\text{B15})$$

$$\delta\phi_{\text{GW}}^{\beta,\text{TII,IPP}} = -1.2 \alpha_1^{2/7} \frac{\dot{m}_{\bullet 1}^{11/14} M_{\bullet 5}^{45/14}}{m_{\star 2}^{37/14}} \bar{r}_{0,20}^6 \times \left(1 - 5x^6 + 4x^{15/2}\right). \quad (\text{B16})$$

where again $x \equiv x(\bar{r}_f, T)$ and $\bar{r}_0 \equiv \bar{r}_0(\bar{r}_f, T)$. Notice that we have normalized the CO's mass to $m_{\star 2} = m_{\star}/(100M_{\bullet})$, where a gap opens and Type-II migration occurs.

Let us now take the two limiting cases of long and short observations. For long and short observations, we find a dephasing as in Eq. (A13) and (A14) respectively, with (C_i, c_j) and (D_i, d_j) given by the tenth, eleventh and twelfth rows of Table II.

Appendix C: Phase Correction due to the Disk Gravity

Let us study how the gravitational potential generated by the disk, Φ_{disk} , affects the GW phase. The latter is

given by

$$\phi_{\text{GW}} = 2 \int_{t'_0}^{t_f} \Omega dt = 2 \int_{\bar{r}'_0}^{\bar{r}_f} \Omega(\bar{r}) \frac{d\bar{r}}{\dot{\bar{r}}}, \quad (\text{C1})$$

where now both the angular velocity $\Omega(\bar{r})$ and the inspiral rate $\dot{\bar{r}}$ are modified by the disk potential, see Eq. (97) and (102). The latter also implies a change in the integration bound for a fixed \bar{r}_f and observation time.

We can integrate Eq. (102) perturbatively to obtain

$$\bar{r}_{0'} = \bar{r}_f \left[1 + \frac{\tau}{\bar{r}_f^4} \left(1 + \frac{4}{\tau} \langle \Phi_{\text{disk}} \rangle_{6,2} \right) \right]^{1/4}. \quad (\text{C2})$$

where we have defined

$$\langle \delta\Phi \rangle_{m,n} \equiv \int_{\bar{r}_f}^{\bar{r}_0} \bar{r}^m \frac{d^n \Phi_{\text{disk}}}{d\bar{r}^n} d\bar{r}. \quad (\text{C3})$$

Substituting Eqs. (97) and (102) in Eq. (C1) gives

$$\begin{aligned} \phi_{\text{GW}} &= \frac{5}{32\eta} \int_{\bar{r}_f}^{\bar{r}'_0} \bar{r}^{3/2} \left(1 + \frac{\bar{r}^2}{2} \frac{d\Phi_{\text{disk}}}{d\bar{r}} + \bar{r}^3 \frac{d^2\Phi_{\text{disk}}}{d\bar{r}^2} \right) d\bar{r} \\ &= \frac{5}{32\eta} \left[\frac{2}{5} \left(\bar{r}_{0'}^{5/2} - \bar{r}_f^{5/2} \right) + \frac{1}{2} \langle \delta\Phi \rangle_{7/2,1} + \langle \delta\Phi \rangle_{9/2,2} \right]. \end{aligned} \quad (\text{C4})$$

Subtracting from this expression the vacuum expression for the GW phase, we find

$$\delta\phi_{\text{GW}}^{\text{disk}} = -\frac{5}{32} \frac{M}{m_{\star}} \left(\frac{\langle \delta\Phi \rangle_{6,2}}{\bar{r}_0^{3/2}} - \frac{1}{2} \langle \delta\Phi \rangle_{7/2,1} - \langle \delta\Phi \rangle_{9/2,2} \right). \quad (\text{C5})$$

The result is algebraically similar to the phase shift due to a modified angular momentum loss rate Eq. (B8) or a modified CO mass Eq. (A10). Note that the overall minus sign is compensated for by the sign of the potential $\Phi_{\text{disk}} < 0$.

1. Disk Potential

Let us compute a more convenient form of the disk potential Φ_{disk} . Assuming that $\Sigma(r) = \Sigma_0 r^{\gamma}$, the accretion disk parameters $(\alpha, \dot{m}_{\bullet}, M_{\bullet})$, carried by Σ_0 , can be taken out of the integrals in Eqs. (91,92). The integral only depends on $(\gamma, \bar{r}, \bar{r}_{\min}, \bar{r}_{\max})$. We may evaluate the integrals in the Legendre expansion (92).

$$\begin{aligned} \Phi_{\text{disk}} &= 2\pi\Sigma_0 \sum_{\ell=0,2}^{\infty} [\mathcal{P}_{\ell}(0)]^2 \left\{ \frac{\bar{r}^{1+\gamma}}{\ell+2+\gamma} \left[1 - \left(\frac{\bar{r}_{\min}}{\bar{r}} \right)^{\ell+2+\gamma} \right] \right. \\ &\quad \left. + \frac{\bar{r}^{1+\gamma}}{\ell-1-\gamma} \left[1 - \left(\frac{\bar{r}}{\bar{r}_{\max}} \right)^{\ell-1-\gamma} \right] \right\} \end{aligned} \quad (\text{C6})$$

Next we exercise the gauge freedom to set

$$\Phi_{\text{disk}}^{\text{new}}(\bar{r}) \equiv \Phi_{\text{disk}}(\bar{r}) + \frac{2\pi r_{\max} \Sigma(r_{\max})}{1+\gamma} \quad (\text{C7})$$

and in the following drop the “new” specifier. Note that for both disk models $\gamma > -1$; it is $3/2$ and $-3/5$ for α and β -disks. The disk potential in Eq. (C6) is expressed as a sum of two terms in the curly brackets, which correspond to the potential of the disk interior and exterior to the orbit, respectively.

Let us discuss the contribution of various multipolar harmonics, ℓ .

$$\begin{aligned}\Phi_{\text{disk}}^{\ell=0} &= \frac{2\pi\Sigma_0\bar{r}^{\gamma+1}}{(1+\gamma)(2+\gamma)} \left[1 + (1+\gamma) \left(\frac{\bar{r}_{\min}}{\bar{r}} \right)^{2+\gamma} \right] \\ \Phi_{\text{disk}}^{\ell=2} &= -\frac{\pi\Sigma_0\bar{r}^2}{2(\gamma-1)} \left(\bar{r}_{\max}^{\gamma-1} - \frac{5}{4+\gamma}\bar{r}^{\gamma-1} - \frac{\gamma-1}{4+\gamma}\frac{\bar{r}_{\min}^{4+\gamma}}{\bar{r}^5} \right) \\ \Phi_{\text{disk}}^{\ell=4} &= -\frac{81\pi}{32} \frac{\Sigma_0 r^{\gamma+1}}{(3-\gamma)(6+\gamma)} \left[1 - \frac{6+\gamma}{9} \left(\frac{\bar{r}}{\bar{r}_{\max}} \right)^{3-\gamma} - \frac{3-\gamma}{9} \left(\frac{\bar{r}_{\min}}{\bar{r}} \right)^{6+\gamma} \right].\end{aligned}\quad (\text{C8})$$

In each case we have arranged the terms in increasing order for $\gamma = 3/2$. Equation (C8) shows that for $\gamma > 1$ and $\bar{r} \ll \bar{r}_{\max}$ the potential is dominated by the quadrupolar harmonic $\ell = 2$,

$$\Phi_{\gamma>1}(\bar{r}) \approx \Phi_{\ell=2}(\bar{r}) \approx -\frac{\pi\Sigma_0\bar{r}_{\max}^{\gamma-1}}{2(\gamma-1)}\bar{r}^2. \quad (\text{C9})$$

When $-1 < \gamma < 1$, the disk potential is asymptotically independent of the inner and outer boundaries for $\bar{r}_{\min} \ll \bar{r} \ll \bar{r}_{\max}$. We can then analytically evaluate the infinite sum, and get

$$\Phi_{\gamma<1}(\bar{r}) \approx 2\pi c_0 \Sigma_0 \bar{r}^{\gamma+1} \quad (\text{C10})$$

where

$$c_0 = \frac{1}{\gamma+1} \frac{\Gamma(1+\frac{\gamma}{2})\Gamma(\frac{1-\gamma}{2})}{\Gamma(\frac{3+\gamma}{2})\Gamma(\frac{-\gamma}{2})}. \quad (\text{C11})$$

so that $c_0 = 1.38$ for β -disks where $\gamma = -3/5$. Equations (C9) and (C10) represent the asymptotic solutions for α and β -disks, respectively. Substituting the particular surface density profiles for the two disk models leads to the potential given by Eq. (95).

2. Axisymmetric disk gravity without a gap

We can now evaluate the GW phase shift, Eq. (C5), for the potential generated by α and β -disks without a gap. We restrict to $\bar{r}_{\min} \ll \bar{r} \ll \bar{r}_{\max}$ and substitute Eq. (95)

$$\delta\phi_{\text{GW}}^{\text{adg},\alpha} = -8.3 \times 10^{-5} \alpha_1^{-20/21} \frac{M_{\bullet 5}^{43/21}}{m_{\bullet 1}^{13/21} m_{\star 1}} \bar{r}_{0,20}^{11/2} \times \left(1 - \frac{21}{10}x^{11/2} + \frac{11}{10}x^7 \right), \quad (\text{C12})$$

$$\delta\phi_{\text{GW}}^{\text{adg},\beta} = 3.0 \times 10^{-4} \alpha_1^{-4/5} \frac{\dot{m}_{\bullet 1}^{3/5} M_{\bullet 5}^{11/5}}{m_{\star 1}} \bar{r}_{0,20}^{39/10} \times \left(1 + \frac{3}{10}x^{39/10} - \frac{13}{10}x^{27/5} \right), \quad (\text{C13})$$

where again $x = \bar{r}_f/\bar{r}_0$. The sign difference is due to the fact that the disk exerts an outward pull for α and an inward push for β -disks. In the long and short observation limits, we find dephasing as in Eq. (A13) and (A14) with (C_i, c_j) and (D_i, d_j) given by the thirteenth and fourteenth rows of Table II.

- [1] K. Danzmann and A. Rüdiger, *Class. Quantum Grav.* **20**, S1 (2003).
- [2] K. Danzmann, *Advances in Space Research* **32**, 1233 (2003).
- [3] T. Prince, *American Astronomical Society Meeting* **202**, 3701 (2003).
- [4] “LISA,” www.esa.int/science/lisa, lisa.jpl.nasa.gov.
- [5] J. Carre and E. K. Porter, (2010), * Temporary entry *, arXiv:arXiv:1010.1641 [gr-qc].
- [6] C. Cutler and M. Vallisneri, *Phys. Rev. D* **76**, 104018 (2007), arXiv:0707.2982 [gr-qc].
- [7] L. Barack and C. Cutler, *Phys. Rev. D* **70**, 122002 (2004), arXiv:gr-qc/0409010.
- [8] N. Yunes, M. Miller, and J. Thornburg, (2010), * Temporary entry *, arXiv:arXiv:1010.1721 [astro-ph.GA].
- [9] P. Amaro-Seoane, J. R. Gair, M. Freitag, M. C. Miller, I. Mandel, C. J. Cutler, and S. Babak, *Classical and Quantum Gravity* **24**, 113 (2007), arXiv:astro-ph/0703495.
- [10] L. Barack and C. Cutler, *Phys. Rev. D* **69**, 082005 (2004), arXiv:gr-qc/0310125.
- [11] J. R. Gair, *Class. Quant. Grav.* **26**, 094034 (2009), arXiv:0811.0188 [gr-qc].
- [12] J. E. Barnes and L. Hernquist, *ARA&A* **30**, 705 (1992).
- [13] M. C. Begelman, R. D. Blandford, and M. J. Rees, *Nature* **287**, 307 (1980).
- [14] J. Miralda-Escudé and J. A. Kollmeier, *ApJ* **619**, 30 (2005).
- [15] M. Milosavljević and A. Loeb, *ApJ* **604**, L45 (2004), arXiv:astro-ph/0401221.
- [16] J. Goodman and J. C. Tan, *ApJ* **608**, 108 (2004), arXiv:astro-ph/0307361.
- [17] Y. Levin, *MNRAS* **374**, 515 (2007), arXiv:astro-ph/0603583.
- [18] M. J. Valtonen, S. Mikkola, D. Merritt, A. Gopakumar, H. J. Lehto, T. Hyvönen, H. Rampadarath, R. Saunders, M. Basta, and R. Hudec, *ApJ* **709**, 725 (2010), arXiv:0912.1209 [astro-ph.HE].
- [19] B. Kocsis, Z. Haiman, and K. Menou, *ApJ* **684**, 870 (2008), arXiv:0712.1144.

[20] B. Kocsis, Z. Frei, Z. Haiman, and K. Menou, ApJ **637**, 27 (2006), arXiv:astro-ph/0505394.

[21] B. F. Schutz, Nature **323**, 310 (1986).

[22] D. E. Holz and S. A. Hughes, ApJ **629**, 15 (2005), arXiv:astro-ph/0504616.

[23] C. Deffayet and K. Menou, ApJ **668**, L143 (2007), arXiv:0709.0003.

[24] G. Giampieri, (1993), arXiv:astro-ph/9305034.

[25] S. K. Chakrabarti, ApJ **411**, 610 (1993).

[26] S. K. Chakrabarti, Phys. Rev. **D53**, 2901 (1996), arXiv:astro-ph/9603117.

[27] D. Molteni, G. Gerard, and S. K. Chakrabarti, ApJ **436**, 249 (1994).

[28] F. Hoyle and R. A. Lyttleton, in *Proceedings of the Cambridge Philosophical Society*, Proceedings of the Cambridge Philosophical Society, Vol. 35 (1939) pp. 405–+.

[29] H. Bondi and F. Hoyle, Monthly Notices of the Royal Astronomical Society **104**, 273 (1944).

[30] H. Bondi, Monthly Notices of the Royal Astronomical Society **112**, 195 (1952).

[31] S. L. Shapiro and S. A. Teukolsky, *Black Holes, White Dwarfs and Neutron Stars: The Physics of Compact Objects*, by Stuart L. Shapiro, Saul A. Teukolsky, pp. 672. ISBN 0-471-87316-0. Wiley-VCH, June 1986., edited by Shapiro, S. L. & Teukolsky, S. A. (1986).

[32] R. Edgar, New A Rev. **48**, 843 (2004), arXiv:astro-ph/0406166.

[33] R. Narayan, The Astrophysical Journal **536**, 663 (2000), arXiv:astro-ph/9907328.

[34] L. Šubr and V. Karas, A&A **352**, 452 (1999), arXiv:astro-ph/9910401.

[35] V. Karas and L. Šubr, A&A **376**, 686 (2001), arXiv:astro-ph/0107232.

[36] N. I. Shakura and R. A. Sunyaev, Astron. Astroph. **24**, 337 (1973).

[37] C. F. Gammie, ApJ **553**, 174 (2001), arXiv:astro-ph/0101501.

[38] E. Barausse and L. Rezzolla, Phys. Rev. D **77**, 104027 (2008), arXiv:0711.4558 [gr-qc].

[39] F. D. Ryan, Phys. Rev. D **52**, 3159 (1995), arXiv:gr-qc/9506023.

[40] J. C. B. Papaloizou and J. E. Pringle, Monthly Notices of the Royal Astronomical Society **208**, 721 (1984).

[41] O. M. Blaes, Monthly Notices of the Royal Astronomical Society **212**, 37P (1985).

[42] Y. Kojima, Progress of Theoretical Physics **75**, 251 (1986).

[43] Y. T. Liu and S. L. Shapiro, Phys. Rev. D **82**, 123011 (2010), arXiv:1011.0002 [astro-ph.HE].

[44] M. Milosavljević and E. S. Phinney, ApJ **622**, L93 (2005), arXiv:astro-ph/0410343.

[45] J. D. Schnittman and J. H. Krolik, ApJ **684**, 835 (2008), arXiv:0802.3556.

[46] A. I. MacFadyen and M. Milosavljević, ApJ **672**, 83 (2008), arXiv:astro-ph/0607467.

[47] J. Cuadra, P. J. Armitage, R. D. Alexander, and M. C. Begelman, MNRAS **393**, 1423 (2009), arXiv:0809.0311.

[48] T. Bogdanović, C. S. Reynolds, and R. Massey, ApJ **731**, 7 (2011), arXiv:1005.2193 [astro-ph.CO].

[49] P. Chang, L. E. Strubbe, K. Menou, and E. Quataert, MNRAS **407**, 2007 (2010), arXiv:0906.0825 [astro-ph.HE].

[50] N. Yunes, B. Kocsis, A. Loeb, and Z. Haiman, ArXiv e-prints (2011), (Paper I), arXiv:1103.4609 [astro-ph.CO].

[51] P. J. Sakimoto and F. V. Coroniti, ApJ **247**, 19 (1981).

[52] J. Frank, A. King, and D. J. Raine, *Accretion Power in Astrophysics*, by Juhan Frank and Andrew King and Derek Raine, pp. 398. ISBN 0521620538. Cambridge, UK: Cambridge University Press, February 2002., edited by Frank, J., King, A., & Raine, D. J. (2002).

[53] P. J. Armitage and P. Natarajan, ApJ **634**, 921 (2005), arXiv:astro-ph/0508493.

[54] K. Hayasaki, PASJ **61**, 65 (2009), arXiv:0805.3408.

[55] C. J. Nixon, P. J. Cossins, A. R. King, and J. E. Pringle, MNRAS , 363 (2011), arXiv:1011.1914 [astro-ph.HE].

[56] P. T. Leung, Y. T. Liu, W. Suen, C. Y. Tam, and K. Young, Physical Review Letters **78**, 2894 (1997), arXiv:gr-qc/9903031.

[57] P. Papadopoulos and J. A. Font, Phys.Rev. **D59**, 044014 (1999), arXiv:gr-qc/9808054 [gr-qc].

[58] A. Nagar, G. Diaz, J. A. Pons, and J. A. Font, Phys.Rev. **D69**, 124028 (2004), arXiv:gr-qc/0403077 [gr-qc].

[59] A. Nagar, J. A. Font, O. Zanotti, and R. de Pietri, Phys. Rev. D **72**, 024007 (2005), arXiv:gr-qc/0506070.

[60] A. Nagar, O. Zanotti, J. A. Font, and L. Rezzolla, Phys.Rev. **D75**, 044016 (2007), arXiv:gr-qc/0610131 [gr-qc].

[61] A. Nagar, O. Zanotti, J. A. Font, and L. Rezzolla, Phys. Rev. D **75**, 044016 (2007), arXiv:gr-qc/0610131.

[62] F. P. Esposito, ApJ **165**, 165 (1971).

[63] B. Kocsis and A. Loeb, Physical Review Letters **101**, 041101 (2008), arXiv:0803.0003.

[64] M. Marklund, G. Brodin, and P. K. S. Dunsby, ApJ **536**, 875 (2000), arXiv:astro-ph/9907350.

[65] G. Brodin, M. Marklund, and M. Servin, Phys. Rev. D **63**, 124003 (2001), arXiv:astro-ph/0004351.

[66] D. Papadopoulos, N. Stergioulas, L. Vlahos, and J. Kuijpers, A&A **377**, 701 (2001), arXiv:astro-ph/0107043.

[67] A. Källberg, G. Brodin, and M. Bradley, Phys. Rev. D **70**, 044014 (2004), arXiv:gr-qc/0312051.

[68] C. A. Clarkson, M. Marklund, G. Betschart, and P. K. S. Dunsby, ApJ **613**, 492 (2004), arXiv:astro-ph/0310323.

[69] P. Mösta, C. Palenzuela, L. Rezzolla, L. Lehner, S. Yoshida, and D. Pollney, Phys. Rev. D **81**, 064017 (2010), arXiv:0912.2330 [gr-qc].

[70] M. Johnston, R. Ruffini, and F. Zerilli, Physics Letters B **49**, 185 (1974).

[71] A. Källberg, G. Brodin, and M. Marklund, Classical and Quantum Gravity **23**, L7 (2006), arXiv:gr-qc/0410005.

[72] H. J. Mosquera Cuesta, Phys. Rev. D **65**, 064009 (2002).

[73] N. Yunes, A. Buonanno, S. A. Hughes, M. Coleman Miller, and Y. Pan, Phys.Rev.Lett. **104**, 091102 (2010), arXiv:arXiv:0909.4263 [gr-qc].

[74] N. Yunes, GW Notes, Vol. 2, p. 3-47 **2**, 3 (2009).

[75] N. Yunes, A. Buonanno, S. A. Hughes, Y. Pan, E. Barausse, *et al.*, (2010), “Temporary entry”, arXiv:arXiv:1009.6013 [gr-qc].

[76] K. Yagi et. al., in preparation.

[77] P. C. Peters and J. Mathews, Physical Review **131**, 435 (1963).

[78] P. C. Peters, Physical Review **136**, 1224 (1964).

[79] L. Blanchet, Living Rev. Rel. **9**, 4 (2006), and references therein, gr-qc/0202016.

[80] L. Lindblom, B. J. Owen, and D. A. Brown, Phys. Rev. D **78**, 124020 (2008), arXiv:0809.3844 [gr-qc].

[81] L. Lindblom, Phys. Rev. D **80**, 064019 (2009), arXiv:0907.0457 [gr-qc].

[82] L. Lindblom, J. G. Baker, and B. J. Owen, ArXiv e-prints (2010), arXiv:1008.1803 [gr-qc].

[83] A. P. Lightman and D. M. Eardley, ApJ **187**, L1+ (1974).

[84] N. I. Shakura and R. A. Sunyaev, MNRAS **175**, 613 (1976).

[85] G. S. Bisnovatyi-Kogan and S. I. Blinnikov, A&A **59**, 111 (1977).

[86] T. Piran, ApJ **221**, 652 (1978).

[87] K. Ohsuga, S. Mineshige, M. Mori, and Y. Kato, PASJ **61**, L7+ (2009), arXiv:0903.5364 [astro-ph.HE].

[88] S. Hirose, J. H. Krolik, and O. Blaes, ApJ **691**, 16 (2009), arXiv:0809.1708.

[89] S. Hirose, O. Blaes, and J. H. Krolik, ApJ **704**, 781 (2009), arXiv:0908.1117 [astro-ph.HE].

[90] N. J. Turner, J. M. Stone, J. H. Krolik, and T. Sano, ApJ **593**, 992 (2003), arXiv:astro-ph/0304511.

[91] N. J. Turner, ApJ **605**, L45 (2004), arXiv:astro-ph/0402539.

[92] C. Done and S. W. Davis, ApJ **683**, 389 (2008), arXiv:0803.0584.

[93] J. A. Kollmeier, C. A. Onken, C. S. Kochanek, A. Gould, D. H. Weinberg, M. Dietrich, R. Cool, A. Dey, D. J. Eisenstein, B. T. Jannuzzi, E. Le Floc'h, and D. Stern, ApJ **648**, 128 (2006), arXiv:astro-ph/0508657.

[94] J. R. Trump, C. D. Impey, B. C. Kelly, M. Elvis, A. Merloni, A. Bongiorno, J. Gabor, H. Hao, P. J. McCarthy, J. P. Huchra, M. Brusa, N. Capelluti, A. Koekemoer, T. Nagao, M. Salvato, and N. Z. Scoville, ApJ **700**, 49 (2009), arXiv:0905.1123 [astro-ph.CO].

[95] M. E. Pessah, C. Chan, and D. Psaltis, ApJ **668**, L51 (2007), arXiv:0705.0352.

[96] J. J. Lissauer, O. Hubickyj, G. D'Angelo, and P. Bodenheimer, Icarus **199**, 338 (2009), arXiv:0810.5186.

[97] G. Dubus, J. Hameury, and J. Lasota, A&A **373**, 251 (2001), arXiv:astro-ph/0102237.

[98] A. R. King, J. E. Pringle, and M. Livio, MNRAS **376**, 1740 (2007), arXiv:astro-ph/0701803.

[99] Z. Haiman, B. Kocsis, and K. Menou, ApJ **700**, 1952 (2009), arXiv:0904.1383 [astro-ph.CO].

[100] J. Goodman, MNRAS **339**, 937 (2003), arXiv:astro-ph/0201001.

[101] I. D. Novikov and K. S. Thorne, in *Black Holes (Les Astres Occlus)*, edited by A. Giannaras (1973) pp. 343–450.

[102] D. N. Page and K. S. Thorne, ApJ **191**, 499 (1974).

[103] P. Artymowicz and S. H. Lubow, ApJ **467**, L77+ (1996).

[104] P. B. Ivanov, J. C. B. Papaloizou, and A. G. Polnarev, MNRAS **307**, 79 (1999), arXiv:astro-ph/9812198.

[105] P. J. Armitage and P. Natarajan, ApJ **567**, L9 (2002), arXiv:astro-ph/0201318.

[106] T. Tanaka and K. Menou, ApJ **714**, 404 (2010), arXiv:0912.2054 [astro-ph.CO].

[107] D. N. C. Lin and J. Papaloizou, ApJ **309**, 846 (1986).

[108] G. Bryden, X. Chen, D. N. C. Lin, R. P. Nelson, and J. C. B. Papaloizou, ApJ **514**, 344 (1999).

[109] A. Crida, A. Morbidelli, and F. Masset, Icarus **181**, 587 (2006), arXiv:astro-ph/0511082.

[110] P. Goldreich and S. Tremaine, ApJ **241**, 425 (1980).

[111] P. Artymowicz and S. H. Lubow, ApJ **421**, 651 (1994).

[112] P. Artymowicz, ApJ **419**, 155 (1993).

[113] W. R. Ward, Icarus **126**, 261 (1997).

[114] W. F. Winters, S. A. Balbus, and J. F. Hawley, ApJ **589**, 543 (2003), arXiv:astro-ph/0301589.

[115] D. Syer and C. J. Clarke, MNRAS **277**, 758 (1995), arXiv:astro-ph/9505021.

[116] S. A. Hughes, Phys. Rev. D **61**, 084004 (2000), arXiv:gr-qc/9910091; Phys. Rev. D **63**, 049902 (2001); Phys. Rev. D **65**, 069902 (2002); Phys. Rev. D **67**, 089901 (2003); Phys. Rev. D **78**, 109902 (2008).

[117] J. M. Bardeen and J. A. Petterson, Ap. J. Letters **195**, L65+ (1975).

[118] A. R. King, S. H. Lubow, G. I. Ogilvie, and J. E. Pringle, Monthly Notices of the Royal Astronomical Society **363**, 49 (2005), arXiv:astro-ph/0507098.

[119] G. Lodato and J. E. Pringle, MNRAS **368**, 1196 (2006), arXiv:astro-ph/0602306.

[120] M. Bregman and T. Alexander, ApJ **700**, L192 (2009), arXiv:0903.2051 [astro-ph.GA].

[121] Q. Yu, Y. Lu, and D. N. C. Lin, ApJ **666**, 919 (2007), arXiv:0705.3649.

[122] A. Ulubay-Siddiki, O. Gerhard, and M. Arnaboldi, MNRAS **398**, 535 (2009), arXiv:0909.5333 [astro-ph.CO].

[123] M. R. Krumholz, C. F. McKee, and R. I. Klein, ApJ **618**, 757 (2005), arXiv:astro-ph/0409454.

[124] M. R. Krumholz, C. F. McKee, and R. I. Klein, ApJ **638**, 369 (2006), arXiv:astro-ph/0510410.

[125] M. J. Rees, Phys. Scr **17**, 193 (1978).

[126] M. C. Begelman, MNRAS **187**, 237 (1979).

[127] J. M. Blondin, ApJ **308**, 755 (1986).

[128] P. J. Armitage, ArXiv Astrophysics e-prints (2007), arXiv:astro-ph/0701485.

[129] K. M. Kratter, R. A. Murray-Clay, and A. N. Youdin, ApJ **710**, 1375 (2010), arXiv:0909.2644 [astro-ph.EP].

[130] H. Tanaka, T. Takeuchi, and W. R. Ward, ApJ **565**, 1257 (2002).

[131] S. Chandrasekhar, ApJ **97**, 255 (1943).

[132] D. Lynden-Bell, MNRAS **124**, 279 (1962).

[133] J. Binney and S. Tremaine, *Galactic Dynamics: Second Edition*, by James Binney and Scott Tremaine. ISBN 978-0-691-13026-2 (HB). Published by Princeton University Press, Princeton, NJ USA, 2008., edited by Binney, J. & Tremaine, S. (Princeton University Press, 2008).

[134] E. C. Ostriker, ApJ **513**, 252 (1999), arXiv:astro-ph/9810324.

[135] H. Kim and W. Kim, ApJ **665**, 432 (2007), arXiv:0705.0084.

[136] E. Barausse, MNRAS **382**, 826 (2007), arXiv:0709.0211.

[137] B. Kocsis and S. Tremaine, ArXiv e-prints (2010), arXiv:1006.0001 [astro-ph.GA].

[138] G. D'Angelo, W. Kley, and T. Henning, ApJ **586**, 540 (2003), arXiv:astro-ph/0308055.

[139] S. Paardekooper, C. Baruteau, A. Cruda, and W. Kley, MNRAS **401**, 1950 (2010), arXiv:0909.4552 [astro-ph.EP].

[140] R. P. Nelson and J. C. B. Papaloizou, MNRAS **350**, 849 (2004), arXiv:astro-ph/0308360.

[141] G. Laughlin, A. Steinacker, and F. C. Adams, ApJ **608**, 489 (2004), arXiv:astro-ph/0308406.

[142] S. Paardekooper and G. Meléma, A&A **459**, L17 (2006), arXiv:astro-ph/0608658.

[143] C. M. Hirata, ArXiv e-prints (2010), arXiv:1010.0758 [astro-ph.HE].

[144] C. M. Hirata, ArXiv e-prints (2010), arXiv:1010.0759 [astro-ph.HE].

[145] M. A. Amin and A. V. Frolov, MNRAS **370**, L42 (2006), arXiv:astro-ph/0603687.

[146] M. Lin and J. Papaloizou, ArXiv e-prints (2011), arXiv:1103.5036 [astro-ph.EP].

[147] M. Lin and J. Papaloizou, ArXiv e-prints (2011), arXiv:1103.5025 [astro-ph.EP].

[148] B. Kocsis and A. Sesana, MNRAS **411**, 1467 (2011), arXiv:1002.0584 [astro-ph.CO].

[149] J. H. Krolik, *Active galactic nuclei : from the central black hole to the galactic environment / Julian H. Krolik*. Princeton, N. J. : Princeton University Press, c1999., edited by Krolik, J. H. (1999).

[150] A. Buonanno and T. Damour, Phys. Rev. **D59**, 084006 (1999).

[151] A. Buonanno and T. Damour, Phys. Rev. **D62**, 064015 (2000).

[152] T. Damour, P. Jaranowski, and G. Schaefer, Phys. Rev. **D62**, 084011 (2000).

[153] T. Damour, Phys. Rev. **D64**, 124013 (2001).

[154] A. Buonanno, Y. Chen, and T. Damour, Phys. Rev. **D74**, 104005 (2006).

[155] T. Damour, P. Jaranowski, and G. Schaefer, Phys. Rev. **D78**, 024009 (2008), arXiv:0803.0915 [gr-qc].

[156] E. Barausse and A. Buonanno, Phys. Rev. **D81**, 084024 (2010), arXiv:0912.3517 [gr-qc].

[157] A. Nagar, T. Damour, and A. Tartaglia, Class. Quant. Grav. **24**, S109 (2007), arXiv:gr-qc/0612096.

[158] T. Damour and A. Nagar, Phys. Rev. **D76**, 064028 (2007).

[159] S. Bernuzzi and A. Nagar, Phys. Rev. **D81**, 084056 (2010), arXiv:1003.0597 [gr-qc].

[160] T. Damour, B. R. Iyer, and B. S. Sathyaprakash, Phys. Rev. **D57**, 885 (1998).

[161] T. Damour, B. R. Iyer, and A. Nagar, Phys. Rev. D **79**, 064004 (2009), arXiv:0811.2069 [gr-qc].

[162] Y. Pan, A. Buonanno, R. Fujita, E. Racine, and H. Tagoshi, (2010), arXiv:1006.0431 [gr-qc].

[163] R. Fujita and B. R. Iyer, (2010), arXiv:1005.2266 [gr-qc].

[164] T. Damour and A. Nagar, Phys. Rev. **D79**, 081503 (2009).

[165] A. Buonanno *et al.*, Phys. Rev. **D79**, 124028 (2009).

[166] Y. Pan *et al.*, Phys. Rev. **D81**, 084041 (2010), arXiv:0912.3466 [gr-qc].

[167] L. Barack and N. Sago, Phys. Rev. Lett. **102**, 191101 (2009), arXiv:0902.0573 [gr-qc].

[168] T. Damour, Phys. Rev. **D81**, 024017 (2010), arXiv:0910.5533 [gr-qc].

[169] J. M. Bardeen, W. H. Press, and S. A. Teukolsky, Astrophys. J. **178**, 347 (1972).

[170] E. Poisson and C. M. Will, Phys. Rev. D **52**, 848 (1995), arXiv:gr-qc/9502040.

[171] N. Yunes, K. G. Arun, E. Berti, and C. M. Will, (2009), arXiv:0906.0313 [gr-qc].

[172] B. Kocsis, Z. Haiman, K. Menou, and Z. Frei, Phys. Rev. D **76**, 022003 (2007).